

# An Investigation of Ion Engine Erosion by Low Energy Sputtering

Thesis by

Olivier B. Duchemin

In Partial Fulfillment of the Requirements

for the Degree of

Doctor of Philosophy

California Institute of Technology

Pasadena, California

2001

(Submitted February 28, 2001)

©2001

Olivier B. Duchein

All Rights Reserved

*The surfaces of bodies are the field of very powerful forces of whose action we know but little.*

Lord Rayleigh

*The surface was invented by the devil.*

Wolfgang Pauli

# Acknowledgments

Long before reaching the point of writing these lines, I had forged the conviction that I would abide by two principles in my acknowledgements: the first one, not to mix personal and professional acknowledgements; and the second, to avoid the pitfall of naming a long list of people. Now that the time has come, I realize that I simply have too much to be grateful for to follow these two principles. My first heartfelt thanks therefore go to my family—and to my fiancée Elizabeth—for their unwavering support.

In the process of trudging along the arduous path of experimental research, I have encountered many helpful hands that pointed me in the right direction and prevented me from taking an unhealthy amount of wrong turns. I am indebted to Joel Sercel for sharing with me, and above all communicating to me, his enthusiasm about space vehicle and mission design, as well as his views on concurrent systems engineering. Taking his class as an elective in my first year was a defining moment of my graduate experience. Joel had no small part in my decision to stay and helped me find my way to the Jet Propulsion Laboratory and to what I believe must truly be one of the best propulsion technology groups in the world. I wish to thank John Brophy, for accepting me in his group in the first place, and for allowing me to work on this project. He was followed as group supervisor by Jay Polk, who provided me with

necessary assistance, guidance, and much-needed encouragement when I thought I was learning more about fixing laboratory equipment than science. Both John and Jay showed much patience with the slow progress of my work.

Working within this group was an incredibly stimulating experience. The talent, complementarity and dedication of all members of the Advanced Propulsion Technology Group at JPL provided me with an ideal environment and an incredibly tough example to follow. I wish to thank Al Owens, Bill Thogmartin and Robert Toomath for their assistance in the numerous occasions when I felt helpless fixing a piece of equipment or dealing with uncooperative hardware. I would also have had a lot of difficulties writing the second chapter of this dissertation without the fruitful discussions I had with John Anderson and his patient answers to the numerous questions I asked while processing data. Colleen Marrese always showed an unwavering enthusiasm and optimism, and introduced me to the art of setting up a data acquisition system. I am indebted to John Blandino for the time he took to discuss my experiments and his help with exam preparation. Many thanks are also due to Chuck Garner, my initial mentor and office mate, as well as to Dennis Fitzgerald, Bob Frisbee, Keith Goodfellow, Patricia Hayes-Rowe, Lee Johnson, Stephanie Leifer, Jürgen Müller, Muriel Noca, Robert Shotwell, Joe Wang and John Ziemer. To all, my thanks.

In addition, Professor Marc-Aurele Nicolet and Elizabeth Kolawa were kind enough to let me use the magnetron sputtering facilities at Caltech, with the assistance of Stefan Gasser and Pierre Giauque. I also wish to extend my gratitude to Professor Bruce Koel at USC. I was very fortunate to have the opportunity to use his facilities and work with his research group, in particular Chih-Sung Ho and Santanu Banerjee.

Last but not least, very sincere thanks are due to Professor Culick, my advisor, who not only accepted to take me under his wing within the Jet Propulsion Center

at the Graduate Aeronautical Laboratories, but also managed to make me feel truly a part of his research group. I wish to thank him for his interest, when my activities were not along the lines of his main research objectives, and for treating me just like another student of his group. These thanks extend to the whole JPC group at Caltech.

# Abstract

Unlike chemical propulsion systems, which are fundamentally limited in performance by propellant energy density, electric propulsion devices, such as ion engines, are limited in total deliverable impulse by maximum propellant throughput due to engine wear.

In order to perform realistic modeling of engine lifetime, the erosion mechanisms involved must be understood. In particular, the damage—or sputtering—caused by slow ions on solid surfaces is extremely difficult to quantify. We first review the engine failure modes in which sputtering of molybdenum by slow xenon ions plays a critical role. We then present the relevant physical mechanisms, and describe a model for estimating the minimum kinetic energy necessary to dislodge a surface atom.

Over seventeen analytical approaches to the energy dependence of sputtering have been published in the literature. We implement the four that are most relevant to ion engine erosion processes. In addition, we use the Monte-Carlo simulation program TRIM to calculate sputtering yields. We find, in particular, that the relative sensitivity of sputtering yield to surface binding energy increases dramatically near the sputtering threshold energy. Although the surface binding energy is a (weak) function of temperature, we show that the sputtering yield should not increase significantly at temperatures typical of ion engine operation.

An experimental approach to the measurement of low energy sputtering yields is implemented and validated. Based on the Quartz Crystal Microbalance (QCM) technique, this method takes advantage of the differential mass sensitivity exhibited by the piezoelectric quartz resonator used in this study. Because of the importance of surface contamination in low energy sputtering, a surface kinetics model is presented to describe a surface under the simultaneous cleaning effect of ion bombardment, and background gas flow contamination.

A special case of simultaneous surface contamination and erosion occurs during engine ground testing, where carbon is backsputtered on the accelerator grid from the facility. We describe experiments to measure ion-induced desorption cross-sections for carbon on molybdenum, before concluding that the protective effect of the carbon contamination is unlikely to significantly affect engine erosion, so that ground testing results are applicable to space operations.

# Contents

Acknowledgments . . . . .	iv
Abstract . . . . .	vii
Table of Contents . . . . .	ix
List of Figures . . . . .	xiii
List of Tables . . . . .	xviii
Nomenclature . . . . .	xix
<b>1 Introduction and Background</b>	<b>1</b>
1.1 Electric Propulsion and the Need for Lifetime . . . . .	1
1.1.1 Earth Orbit Applications . . . . .	2
1.1.2 Deep Space Missions . . . . .	3
1.2 Summary and Dissertation Outline . . . . .	5
<b>2 Ion Engine Operation and Failure Modes</b>	<b>8</b>
2.1 The NSTAR Ion Engine . . . . .	9
2.2 Failure Modes . . . . .	13
2.2.1 Accelerator Grid Erosion . . . . .	14
2.2.2 Screen Grid Erosion . . . . .	19
2.2.3 Cathode End of Life . . . . .	22

2.3	Assessment of Engine Lifetime by Analysis and Testing . . . . .	26
2.4	Summary . . . . .	29
<b>3</b>	<b>Physics of Sputtering by Energetic Ions</b>	<b>32</b>
3.1	Description and Historical Applications . . . . .	32
3.2	Theory of Physical Sputtering . . . . .	35
3.2.1	Physics and Mechanisms . . . . .	35
3.2.2	Interatomic Potential Models . . . . .	39
3.2.3	Cross-Sections . . . . .	41
3.3	Sputtering Threshold and Surface Binding Energy . . . . .	45
3.4	Summary . . . . .	51
<b>4</b>	<b>Analytical and Computational Treatment of Sputtering</b>	<b>53</b>
4.1	Threshold Energy Model with Inelastic Losses . . . . .	53
4.2	Analytical Formulae for the Energy Dependence of Sputtering yields .	60
4.2.1	The Sigmund Theory . . . . .	60
4.2.2	Semi-Empirical Formulae . . . . .	63
4.2.3	Discussion . . . . .	66
4.3	Monte-Carlo Simulations Using TRIM 2000 . . . . .	70
4.3.1	The TRIM Program . . . . .	70
4.3.2	Results on the Energy Dependence of the Sputtering Yield . .	72
4.3.3	Results on the Temperature Dependence of the Sputtering Yield	74
4.4	Conclusions . . . . .	79
<b>5</b>	<b>The Quartz Crystal Microbalance Technique</b>	<b>81</b>
5.1	Low Energy Sputtering Measurement Techniques . . . . .	81
5.2	Physical Principle . . . . .	84

5.3	Temperature Sensitivity . . . . .	87
5.4	Differential Mass Sensitivity . . . . .	89
5.5	Practical Implementation: The Current-Sensitivity Integral . . . . .	93
5.6	Conclusions . . . . .	95
<b>6</b>	<b>Experimental Measurements of Low Energy Sputtering Yields</b>	<b>97</b>
6.1	Apparatus and Procedure . . . . .	97
6.1.1	Vacuum Chamber . . . . .	97
6.1.2	Ion Source . . . . .	99
6.1.3	Beam Diagnostics . . . . .	101
6.1.4	Sputtering Measurements . . . . .	102
6.1.5	Other Diagnostics . . . . .	105
6.1.6	Data Acquisition . . . . .	108
6.1.7	Experimental Procedure . . . . .	108
6.2	Sample Preparation and Properties . . . . .	109
6.2.1	Preparation . . . . .	109
6.2.2	Sample Density . . . . .	113
6.2.3	Sample Surface Contamination . . . . .	117
6.3	Results and Discussion . . . . .	121
6.4	Conclusions . . . . .	125
<b>7</b>	<b>The Effect of Carbon Deposition in Ground-Based Operations</b>	<b>127</b>
7.1	Accelerator Grid Erosion by Charge-Exchange Ions During Ion Engine Ground Testing . . . . .	127
7.2	Surface Kinetics Model . . . . .	132
7.3	Desorption Cross-Section Model . . . . .	133

7.4	Experimental Measurements of Carbon Desorption Cross-Sections . . .	136
7.4.1	Surface Diagnostics and Ion Scattering Spectroscopy . . . . .	136
7.4.2	Apparatus and Sample Preparation . . . . .	139
7.4.3	Experimental Procedure . . . . .	141
7.4.4	Results . . . . .	143
7.5	Discussion . . . . .	146
7.6	Conclusions . . . . .	147
<b>8</b>	<b>Conclusions</b>	<b>150</b>
8.1	Summary of Major Results . . . . .	150
8.2	Future Work . . . . .	155
8.3	Outlook . . . . .	157
<b>A</b>	<b>Divergence of a Non-Neutralized Beam</b>	<b>159</b>
	<b>Bibliography</b>	<b>161</b>

# List of Figures

1.1	Ion vs. chemical rocket in deep space. . . . .	4
2.1	Schematic diagram of the NSTAR ion engine. . . . .	11
2.2	The NSTAR 30-cm ion engine. . . . .	12
2.3	Electrostatic potential and ion current density in an individual ion optics aperture. . . . .	13
2.4	Accelerator grid erosion pattern for a 10-kW xenon ion thruster. . . .	15
2.5	Electron backstreaming limit vs. time during NSTAR mission profile test. . . . .	16
2.6	Perveance limit vs. time during NSTAR mission profile test. . . . .	18
2.7	Screen grid transparency to ions vs. time during NSTAR mission profile test. . . . .	19
2.8	Cross-section of screen grid webbing after 8200-hour wear test. . . .	20
2.9	Discharge loss vs. time during NSTAR mission profile test. . . . .	22
2.10	Cathode erosion at end of engineering model thruster 8200-hour LDT. . . .	24
2.11	Cathode erosion during on-going spare flight thruster MPT. . . . .	25
2.12	Flow chart of probabilistic risk assessment. . . . .	29
2.13	Screen grid structural failure risk vs. engine propellant throughput. . .	30

3.1	Classical two-particle scattering. . . . .	36
3.2	A “billiard-ball” description of sputtering mechanisms. . . . .	38
3.3	A comparison of stopping cross-sections in Thomas-Fermi coordinates for different interatomic potentials. . . . .	44
3.4	Sputtering threshold energy and yield as a function of ion angle of incidence for xenon on molybdenum. . . . .	50
4.1	Relative sputtering threshold versus number of collisions for xenon ions on molybdenum, assuming no inelastic energy losses; a quarter, and a full Lindhard-Scharff inelastic stopping power. . . . .	57
4.2	Relative sputtering threshold at normal incidence versus number of collisions for xenon ions on different target materials, using a quarter Lindhard-Scharff inelastic stopping power. . . . .	59
4.3	Analytical formulae, computer simulations, and previous experimental data for the energy dependence of the sputtering yield of molybdenum by xenon ions. . . . .	69
4.4	Distribution of the normal component of the kinetic energy of displaced atoms reaching the surface for four different bombarding ion energies.	73
4.5	Average energy of sputtered atoms, number of backscattered ions and vacancies created per ion versus energy for xenon ion bombardment of molybdenum. . . . .	74
4.6	Longitudinal view of final recoil and ion positions for different values of ion energy. . . . .	75
4.7	Contributions of ionization, vacancies and phonons to the energy loss of ions and recoil atoms for xenon bombardment of molybdenum. . .	76

4.8	Dependence of the atomic heat of sublimation on temperature, for tungsten and molybdenum. . . . .	77
4.9	Differential plots of displaced atoms energy at the surface for xenon bombardment of molybdenum, at varying bombarding ion kinetic energies. . . . .	78
4.10	Sputtering yield dependence on surface binding energy and temperature at near-threshold energy for xenon on molybdenum. . . . .	79
5.1	Planar resonator and fundamental thickness shear mode of vibration.	85
5.2	Frequency-temperature curves for the AT family of quartz crystal resonators. . . . .	88
5.3	Plano-convex quartz crystal resonator. . . . .	89
5.4	Differential mass sensitivity for a 6-MHz, plano-convex quartz crystal resonator. . . . .	92
6.1	JPL facility for low energy sputtering yield measurements. . . . .	98
6.2	Electrical schematic of the ion gun. . . . .	100
6.3	Schematic diagram of the $E \times B$ velocity filter built for the experiments.	101
6.4	$E \times B$ traces for 100-, 400-, and 800-eV xenon ions. . . . .	103
6.5	$E \times B$ traces vs. discharge voltage for 400-eV singly- and doubly-charged xenon ions. . . . .	104
6.6	Radial beam current density profiles for two different focusing voltages.	105
6.7	QCM sensor assembly. . . . .	106
6.8	Electrical schematic of the QCM sensor assembly, and data acquisition.	107
6.9	SEM micrograph of a molybdenum engine grid bit broken in liquid nitrogen, edge view. Magnification $\times 7000$ . . . . .	111

6.10	Thornton diagram: schematic representation of the influence of substrate temperature and argon working pressure on the structure of metal coatings deposited by sputtering using cylindrical magnetron sources. . . . .	112
6.11	SEM micrographs of molybdenum films broken in liquid nitrogen, for different anode bias voltages during deposition. . . . .	114
6.12	SEM micrograph of the surface of a 30-kÅ molybdenum film deposited with an anode bias voltage of -80 V. Magnification $\times 25000$ . . . . .	115
6.13	Regenerative vs. destructive processes for an adsorbate layer on a substrate. . . . .	117
6.14	Beam-to-background gas particles flux ratio at a surface at room temperature. . . . .	119
6.15	Time history of eroded thickness for 1-keV, 600-eV and 300-eV xenon ion bombardment on molybdenum. . . . .	122
7.1	Electrostatic potential contours and ion trajectories in an individual ion optics aperture. . . . .	128
7.2	Schematic diagram of the NSTAR ground testing facility, and particle flows to and from the engine during thruster operation. . . . .	129
7.3	Sputtering yields for xenon on bulk molybdenum and carbon. . . . .	130
7.4	Optical photographs showing the deposition and erosion patterns on the downstream side of the accelerator grid. . . . .	131
7.5	SEM images with elemental resolution showing the deposition and erosion pattern on the downstream side of the accelerator grid. . . . .	131
7.6	Mechanisms of ion-induced desorption, <i>e.g.</i> , carbon adsorbate on a molybdenum substrate. . . . .	135

7.7	Principle of Ion Scattering Spectroscopy. . . . .	137
7.8	Diagnostics setup in the ultra high vacuum facility used to measure the ion-induced desorption cross-sections. . . . .	138
7.9	Ultra high vacuum facility used to measure the ion-induced desorption cross-section. . . . .	139
7.10	Molybdenum ISS peak vs. time for 500-eV argon ion-induced desorp- tion of carbon on a molybdenum single crystal. . . . .	142
7.11	Ion source used in the ion-induced desorption experiments. . . . .	143
7.12	ISS signal area for molybdenum vs. xenon ion fluence. . . . .	145
7.13	Measured and calculated cross-sections for ion-induced desorption of carbon from molybdenum by xenon and argon ions. . . . .	147
7.14	Attenuation of molybdenum sputtering yield due to carbon deposition vs. ion impingement current density. . . . .	149
8.1	Analytical formulae, computer simulations, previous experimental data, and results of the present study for the energy dependence of the sput- tering yield of molybdenum by xenon ions. . . . .	154
8.2	Analytical formulae and computer simulations for the energy depen- dence of the sputtering yield of molybdenum by xenon ions below 100 eV.	155

# List of Tables

2.1	NSTAR throttle and performance table at beginning of life. . . . .	10
2.2	NSTAR engine and performance parameters. . . . .	28
3.1	Thomas-Fermi energy $E_{TF}$ for different projectile-target combinations.	40
3.2	Experimental and analytical values of the sputtering threshold energy (eV) for xenon ions and different target elements. . . . .	49
4.1	Sputtering threshold values for xenon ion bombardment on different target materials for two models of inelastic energy losses. . . . .	58
4.2	Quantitative uncertainties in the Wilhelm theory for xenon on molybdenum. . . . .	68
6.1	Magnetron sputtering deposition parameters. . . . .	113
6.2	Density estimates for the sputter-deposited molybdenum films. . . .	116
6.3	Summary of results for sputtering experiments with xenon ions on molybdenum. . . . .	124
6.4	Sputtering yield of xenon on molybdenum, comparison with other data from published literature. . . . .	125
7.1	Summary of experimental ion-induced desorption cross-section measurements for carbon on molybdenum. . . . .	146

# Nomenclature

## Acronyms and Abbreviations

AES	Auger Electron Spectroscopy
APPH	Auger Peak-to-Peak Height
CSI	Current-Sensitivity Integral
DS 1	<i>Deep Space 1</i>
JPL	Jet Propulsion Laboratory
ISS	Ion Scattering Spectroscopy
LDT	Life Demonstration Test
LSS	Lindhard-Scharff-Schiott
MPT	Mission Profile Test
NASA	National Aeronautics and Space Administration
NSTAR	NASA Solar electric propulsion Technology Application Readiness
PKA	Primary Knock-on Atom
QCM	Quartz Crystal Microbalance
RBS	Rutherford Backscattering Spectrometry
SCA	Spherical Capacitor Analyzer
SEM	Scanning Electron Microscope

SEP	Solar Electric Propulsion
SKA	Secondary Knock-on Atom
SRIM	the Stopping and Range of Ions in Matter, scientific software package
TH	thrust level, defined in Table 2.1
TRIM	the TRansport of Ions in Matter, Monte-Carlo simulation program
ZBL	Ziegler-Biersack-Littmark

## English Symbols

$a$	quartz crystal active area, cm
$a_{BM}$	Born-Mayer screening radius, 0.219 Å
$a_I$	Lindhard screening radius, Å
$a_o$	Bohr radius, 0.529 Å
$A_{BM}$	constant in Eq. 4.12, eV
$A_s$	fit parameter in Eq. 4.22
$b$	impact parameter in a binary collision, Å
$B$	magnetic induction, T
$c_0$	crystal constant, defined by Eq. 5.9
$c_f$	differential crystal mass sensitivity, Hz/g
$C$	constant in Eq. 7.10
$C_{55}$	quartz constant in Eq. 5.11, $6.881 \times 10^{10} \text{ N}\cdot\text{m}^{-2}$
$\overline{C_{66}}$	quartz constant in Eqs. 5.10 and 5.11, $2.924 \times 10^{10} \text{ N}\cdot\text{m}^{-2}$
$C_a$	cross-section factor, defined by Eq. 7.9, $\text{cm}^2$
$C_{AT}$	transverse wave speed for an AT-cut quartz crystal, m/s

$C_f$	crystal mass sensitivity, Hz·cm <sup>2</sup> /g
$C_m$	constant in Eq. 3.10, eV <sup>2m</sup> ·Å <sup>2</sup>
$d$	source-to-target distance, cm
$dm$	mass element, g
$ds$	surface area element, cm <sup>2</sup>
$e$	electronic charge, 1.60×10 <sup>-19</sup> C, or elementary charge, defined by $e^2=14.39$ eV·Å in LSS theory
$E$	particle energy, eV, or electric field, V/m
$E_l$	average minimum energy for atom escape
$E_R$	Rydberg energy, 13.6 eV
$E_{TF}$	Thomas-Fermi energy, eV
$f$	resonant frequency of a quartz crystal oscillator, Hz
$f_0$	resonant frequency of an unloaded quartz crystal oscillator, Hz
$F_D$	density of energy deposited at a surface, eV/Å
$h$	parameter in Eq. 3.22, or half-thickness of planar resonator, cm
$h_0$	half-thickness at center of a plano-convex resonator, cm
$h_{1/2}$	coefficient in Eq. 4.23
$h_E$	electrode thickness on a coated quartz crystal, cm
$I$	ISS signal intensity
$I_a$	accelerator grid current, A
$I_b$	beam current, A
$I_{sp}$	specific impulse, s
$J_b$	ion engine beam current density, A/cm <sup>2</sup>

$J$	ion gun beam current density, nA/mm <sup>2</sup>
$k$	number of collisions
$k_{26}^2$	quartz constant in Eqs. 5.10 and 5.11, $7.744 \times 10^{-3}$
$k_e$	Lindhard electronic stopping coefficient
$l$	mean free path, Å
$m$	parameter in Eqs. 3.10 and 3.11
$M_1$	projectile particle mass, amu, or quartz constant in Eq. 5.10, $1.10 \times 10^{11}$ N·m <sup>-2</sup>
$M$	atomic mass, amu
$n$	surface atomic number density, cm <sup>-2</sup>
$N$	bulk atomic number density, cm <sup>-3</sup> or Å <sup>-3</sup>
$p_s, q_s$	fit parameters in Eq. 4.22
$P$	pressure, Pa
$q$	electric charge, C
$Q$	fit parameter in Eq. 4.21
$r$	radial coordinate, mm or Å
$R$	radius of curvature, cm or m, or beam radius, cm
$R_0$	apsis of a head-on collision in the hard-core approximation to the Born-Mayer potential, Å
$R_{12}$	reflection coefficient for the projectile 1 in the element 2
$R_a, R_p$	average and projected range, respectively, of ions in a solid, Å
$s_e(\epsilon)$	reduced electronic stopping power
$s_n(\epsilon)$	reduced nuclear stopping power
$S$	surface area of quartz crystal resonator, cm <sup>2</sup>

$S_e$	electronic stopping power, $\text{eV}\cdot\text{\AA}^2$
$S_{i,s}$	sticking probability of gas species $i$ on clean surface $s$
$S_n$	nuclear stopping power, $\text{eV}\cdot\text{\AA}^2$
$t$	time, s
$T$	energy transferred in a scattering event, eV, or temperature, ° or K
$T_m$	melting temperature, K
$U_b$	surface binding energy, eV
$U_d$	lattice displacement energy, eV
$U_s$	sublimation energy, eV
$v$	particle velocity, m/s
$V$	interatomic potential, eV
$V_s$	screen grid voltage, V
$x$	Cartesian coordinate, $\text{\AA}$ , or parameter in Eq. 7.5
$y$	parameter in Eq. 7.6
$Y$	sputtering yield
$Z$	atomic number

## Greek Symbols

$\alpha$	energy independent function of the mass ratio in Eqs. 4.13 and 4.20
$\alpha^*$	energy independent function of the mass ratio in Eq. 4.21
$\beta$	sputtered atom emission angle, with respect to surface normal

$\hat{\beta}$	sputtered atom emission angle for lowest threshold energy, with respect to surface normal
$\gamma$	energy transfer factor in a binary collision, defined by Eq. 3.3
$\Gamma$	energy independent function of $M_1$ and $Z_2$ in Eq. 4.21
$\delta$	beam divergence angle
$\Delta\tau$	actual thickness change, cm
$\Delta\tau_{meas}$	measured thickness change, cm
$\epsilon$	Linhard's reduced energy, defined by Eq. 3.6
$\epsilon_0$	permittivity of vacuum, $8.854 \times 10^{-12}$ F/m
$\eta$	inverse time constant, s, defined in Eq. 6.3
$\Theta$	barycentric scattering angle
$\theta$	azimuthal polar coordinate, or projectile scattering angle in laboratory frame of reference
$\vartheta$	incidence angle with respect to surface normal
$\lambda$	dimensionless function of the parameter $m$ , defined by Eq. 3.11
$\mu_0$	permeability of vacuum, $4\pi \times 10^{-7}$ N/A <sup>2</sup>
$\xi$	fractional surface coverage
$\rho$	electronic density, electrons/cm <sup>3</sup>
$\rho_E$	density of electrode on a quartz crystal resonator, g/cm <sup>3</sup>
$\rho_Q$	quartz crystal density, 2.649 g/cm <sup>3</sup>
$\sigma$	scattering cross-section, cm <sup>2</sup>
$\sigma_0$	areal mass density, g/cm <sup>2</sup>
$\sigma_d$	ion-induced desorption cross-section, cm <sup>2</sup>
$\tau$	thickness, cm
$\phi$	target particle scattering angle in laboratory frame of reference

$\Phi$	screening function
$\varphi$	particle flux density, $\text{s}^{-1}\text{cm}^{-2}$

## Subscripts

1	related to incident particle
2	related to target particle
$a$	related to adsorbate
AT	related to a quartz crystal resonator, defines the cut as (yxl)- 35.25°
$b$	related to beam
$c$	related to center of mass
$C$	related to carbon
$e$	related to electrons
$g$	related to gas phase
$i$	related to gas species
$m$	parameter, defined by Eq. 3.10
$Mo$	related to molybdenum
$n$	related to nuclei
$s$	related to substrate

## Miscellaneous Symbols

$\mathcal{H}(\cdot)$	Heaviside step function
$\Delta E$	electronic energy loss, eV
$\Delta f$	change in resonant frequency, Hz
$\Delta m$	mass loading, g

$\Delta t$	duration of exposure, s
$\Delta V$	velocity increment, m/s
$\Delta\sigma$	change in areal mass density, g/cm <sup>2</sup>

# Chapter 1

## Introduction and Background

This chapter proposes a very brief introduction to the benefits and challenges associated with the use of electric propulsion. It provides the motivational background for the work described in this dissertation.

### 1.1 Electric Propulsion and the Need for Lifetime

The use of electric propulsion is continuously increasing. By the end of the year 2000, a total of 388 electric thrusters were on board 152 spacecraft, 19 of which had been launched into space over the past year [1]. In particular, and after four decades of experimental research and laboratory testing, ion engine technology has now reached a level of maturity that allows such engines to be baselined in a variety of Earth-orbit or deep space missions. Electric propulsion devices, such as ion engines, fulfill mainly three roles: attitude control, orbit maintenance, and/or primary propulsion to provide orbital changes. They have now been recognized by mission planners and spacecraft operators as capable of providing substantial gains in mission performance and/or cost reductions.

### 1.1.1 Earth Orbit Applications

For Earth-orbit missions, the benefits brought by electric propulsion translate into increased operational life, higher payload mass and/or reduced launch vehicle costs. As an example, a geostationary satellite needs a total velocity increment (or  $\Delta V$ ) of up to 55 m/s per year of service life for North-South Station Keeping (NSSK) [2]. This, to a first order approximation, corresponds to a total (annual) impulse of 110 kN·s to be delivered for a 2-ton class satellite. For total Geostationary Earth Orbit (GEO) station-keeping and repositioning of such a 2-ton satellite, the gross (wet) propulsion system mass for a 10-year orbit life would be about 600 kg and 250 kg respectively for a chemical and ion propulsion system [3].

In the case of an Earth-orbiting satellite, the choice of electric propulsion to perform orbit raising however comes at the cost of a longer transfer time and needs to be the result of a trade-off study that accounts for, in particular, the loss of revenue during that period or the possible damage due to an extended exposure to the severity of the Van Allen radiation belt. A 1987-study [4] envisioned the use of electric propulsion instead of a conventional chemical upper stage to transfer the Global Positioning System (GPS) satellites from parking in low Earth orbit to mission orbits. The study concluded that this could potentially reduce the mass of the cargo element to be delivered to the low Earth parking orbit by 73% and the transport to orbit life cycle cost by up to 61%, or \$21 million per flight. The flight time requirement was 90 days or less. Thus, while Solar Electric Propulsion (SEP) is currently used for geostationary satellite station keeping, additional increases in payload mass or decreases in launch vehicle costs are achieved by using this technology for orbit transfers.

Other studies [5–10] have described in great detail the substantial benefits of electric propulsion specific to Earth orbit applications, which include orbit insertion,

orbit transfers, attitude control, orbit maintenance, and de-orbit. Such benefits are needed to accompany the current trend of communications satellites towards longer lifetimes, increased masses and higher powers. Increased masses mean more transmission channels and more effective use of orbital positions, while higher powers translate into larger bandwidths. For a satellite mission time of 15 years, expected thruster operation times over 15000 hours are desirable [8].

### 1.1.2 Deep Space Missions

The benefits provided by electric propulsion to deep-space missions translate into reduced trip times, greater spacecraft net mass and/or smaller launch vehicles. To date, ion engines are the most efficient electric propulsion devices in the specific impulse ( $I_{sp}$ ) range optimum for interplanetary spacecraft.

A rather simple example might be taken by considering the very simplistic hypothesis of a “seventy million km dash” race between two 500-kg interplanetary probes in deep space starting with a zero relative velocity. As depicted in Fig. 1.1 the difference in performance is clearly in favor of the ion-propelled spacecraft for missions that are sufficiently challenging from a propulsion standpoint. Although overly simplistic because it would not correspond to a realistic mission profile, this example illustrates the difference between a low-thrust, high- $I_{sp}$  and a high-thrust, low- $I_{sp}$  propulsion system. Another word of caution needs to be said when comparing high-thrust to low-thrust propulsion systems about the significance of gravity losses in the real world: the required  $\Delta V$  can be more than doubled for a low-thrust trajectory [11]. The mass and performance in this example were chosen to correspond closely to that of the *Deep Space 1* (DS 1) spacecraft launched in October 1998. DS 1, a technology demonstration mission currently on its extended mission, was the first interplanetary mission to

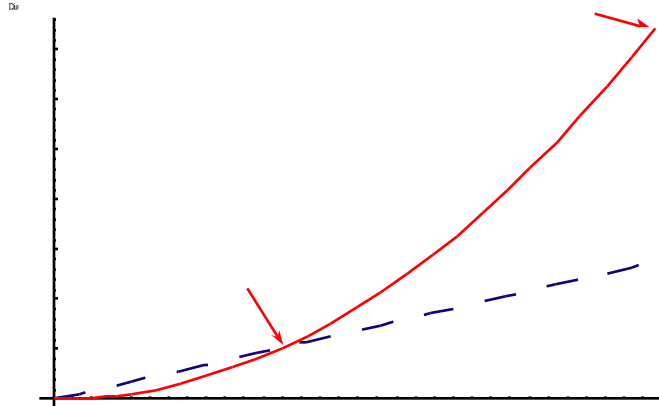


Figure 1.1: Ion vs. chemical rocket in deep space. The two spacecraft start with zero relative velocity. The trajectory curves result from the integration of the equations of motion assuming an ideal impulsive burn for the chemical rocket (dashed line) with an  $I_{sp}$  of 320 s, and no gravity losses with an  $I_{sp}$  of 3200 s for the ion propulsion rocket (solid line). Both spacecraft have a 500-kg wet mass and a propulsion system mass of 163 kg. This includes 82 kg of xenon propellant and 75 kg of propulsion system dry mass, including solar arrays, for the ion propulsion system, and 136 kg of  $N_2O_4/N_2H_4$  bipropellant and 20 kg of propulsion system dry mass for the chemical propulsion system.

implement electric propulsion as its primary propulsion system and made the use of ion propulsion for deep space missions a reality [12]. The single 30-cm ion thruster on DS 1 will deliver a total  $\Delta V$  of 4.5 km/s to the 486 kg spacecraft during its mission while consuming less than 81 kg of xenon propellant, corresponding to a lifetime at full power of 7500 hours (8200 hours demonstrated before launch).

Direct comparisons between chemical bi-propellant and ion propulsion systems for deep space missions are not straightforward though. One-way minimum-energy transfers produce unacceptable travel times to target planets, and modern trajectories usually involve one or more gravity assists that can provide a  $\Delta V$  much greater than that provided by the on-board propulsion system [13–18]. As an example, the main unit in the *Voyager* spacecraft propulsion system was the Solid Rocket Motor (SRM)

that provided for the final increment of injection velocity after launch by a Titan-Centaur III E. The launch mass was 2016 kg and included 1046 kg of SRM expelled mass for a total delivered impulse of 2897 kN·s. However, the gravity assist at Jupiter saved both *Voyager* spacecraft over 1600 tons of in-flight propulsive mass [19]. Indeed, the benefit of electric propulsion to solar system exploration missions can often be seen not by merely comparing propulsion system performance but rather by comparing *trajectory* performance. Ref. [20] describes a Neptune orbiter mission involving a Solar Electric Earth Gravity Assist (SEEGA) trajectory with ion propulsion. This mission delivers a total payload (an orbiter) of 310 kg to Neptune after a 10-year trip time and using a Delta II 7925, a \$52M launch vehicle. In comparison, *Voyager 2* reached Neptune in 12 years with a 115-kg science payload and using a launch vehicle that would cost over \$250M today.

Numerous additional examples can be found in the literature that further illustrate how electric propulsion technology can enable (by reducing the launch mass) or enhance (by reducing trip times and allowing greater payloads) scientific solar system or interstellar exploration missions [14, 21–31].

## 1.2 Summary and Dissertation Outline

In summary, the superior performance of electric propulsion systems for propulsively demanding missions, despite the need for an external power source, fundamentally comes from values of  $I_{sp}$  (a measure of achievable  $\Delta V$ ) that are an order of magnitude higher than those typical for on-board chemical propulsion systems. However, while the practical limit to high- $\Delta V$  space missions using chemical propulsion resides with the prohibitive propellant mass due to limited propellant energy density, the greatest

issue with ion engine performance is maximum propellant throughput capability per engine. Put differently, the leverage for improved performance is not *specific* impulse, but rather *total* deliverable impulse. In fact, improved lifetime for an ion engine can readily translate into a combination of increased performance, decreased risk and/or decreased propulsion system dry mass.

In addition, such improvements will be needed for a variety of currently envisioned high-energy planetary exploration missions that depart from the propulsively “easy” fly-by missions of the last decades and recent orbiter missions. Example near- and mid-term missions that place increased requirements on spacecraft propulsion include the Solar Probe, Mercury Orbiter, Neptune Orbiter, Titan Explorer, Saturn Ring Observer, Europa Lander, and sample return missions to comets, Venus, or Mars. Even a typical small-body rendezvous mission would require an engine service life of 9000–12000 hours [32]. The success of the NASA Solar electric propulsion Technology Application Readiness (NSTAR) program was not only to develop, qualify and flight-validate Solar Electric Propulsion (SEP) technology, but also and perhaps as importantly to stimulate the consideration of propulsively more difficult solar system exploration missions requiring improved SEP systems.

In this dissertation, Chapter 2 will provide a review of the specific life-limiting phenomena encountered in the NSTAR ion engine, and will explain the method implemented to provide quantitative estimates of engine lifetime. Chapter 3 describes the physics and theory of sputtering—the removal of near-surface atoms—by energetic ions. Chapter 4 is closely related: it is an attempt to clarify the use of theoretical or semi-empirical formulae to evaluate the sputter yield. It shows, in addition, the results of computer simulations by Monte-Carlo methods. Chapter 5 describes the Quartz Crystal Microbalance (QCM) technique and a novel way of implementing it

for the measurement of very low erosion rates, and Chapter 6 presents the experimental procedure implemented to measure low-energy sputter yields of xenon ions on molybdenum as well as the data analysis and results. Chapter 7 is more specifically related to a subset of engine failure modes involving the erosion of the downstream side of the ion extraction optics, and discusses the effect of carbon deposition originating from ground facilities on accelerator grid wear rates. It describes desorption cross-sections measurements on thin carbon films in the monolayer-range deposited on molybdenum. Finally, Chapter 8 summarizes the main results and provides concluding remarks and recommendations. Although Chapters 2 and 3 are closely related to the work described in Ref. [33], a significant amount of material has been added or modified. Likewise, Chapters 5–6 and 7, respectively, are based on the work described in Refs. [34, 35].

## Chapter 2

# Ion Engine Operation and Failure Modes

Electric propulsion devices, and in particular ion engines, are inherently low-thrust (low-mass flow rate) systems. In particular, the thrust and corresponding total mass flow rate for the NSTAR 30-cm thruster range from about 94 mN and 3 mg/s at full power to 20 mN and 1 mg/s at minimum power, with cathode mass flow rates as low as 0.24 mg/s (Table 2.1). Such devices thus need to operate for extended amounts of time—typically thousands to tens of thousands of hours—to impart the appropriate  $\Delta V$  to a spacecraft. As a consequence, the design challenges reside mostly with the propellant management devices necessary to control mass flow rates lower than a mg/s, and engine lifetime. The latter challenge is the subject of the effort described in this dissertation, and this chapter provides an overview of the life-limiting phenomena for ion engines with a special emphasis on the ones driven by low-energy sputtering processes.

## 2.1 The NSTAR Ion Engine

The 30-cm NSTAR ion engine is shown schematically in Fig. 2.1 and pictured in Fig. 2.2. During normal, steady engine operation, the propellant—neutral xenon gas—is fed into the discharge chamber—the main internal volume of the thruster. The self-heating, discharge hollow cathode provides the primary electrons necessary to ionize the propellant. To improve the ionization efficiency, three rare-earth permanent ring magnets mounted around the discharge chamber create a magnetic field which lengthens the path of the electrons from the cathode to the annular anode that makes up the wall of the discharge chamber, thus increasing the collision probability with neutral gas atoms. The plasma generated is a cold, unmagnetized plasma floating at a potential close to anode potential. Some of the xenon ions produced in this electron-bombardment process drift toward the upstream grid electrode—the screen grid—maintained at cathode potential. A large fraction of these ions are focused and accelerated in the region between the screen grid and the downstream grid—the accelerator grid—by an inter-electrode potential field of appropriate strength and geometry.

It should be stressed that the beam focusing is achieved by the shape of the electrostatic field lines that result from the applied potential and the electrode geometry (spacing, aperture diameter and thickness) as shown in Fig. 2.3. The purpose of the two grid electrodes—constituting the ion optics—is thus threefold: extraction, focusing, and acceleration of the ions produced in the discharge chamber. Immediately downstream of the (negative) accelerator grid, the ions are decelerated to ambient space-plasma potential where global space-charge neutrality is ensured by the electrons emitted into the plume by the neutralizer electrode. Thus, the negatively-biased accelerator grid also serves the key function of preventing the electrons emitted by

NSTAR throttle level	Nominal thruster power	Beam supply voltage	Beam current	Accel. grid voltage	Neut. keeper current
TH	kW	V	A	V	A
0	0.47	650	0.51	-150	2.0
1	0.60	850	0.53	-150	2.0
2	0.74	1100	0.52	-150	2.0
3	0.85	1100	0.61	-150	2.0
4	0.97	1100	0.71	-150	2.0
5	1.09	1100	0.81	-150	2.0
6	1.21	1100	0.91	-150	2.0
7	1.33	1100	1.00	-150	2.0
8	1.44	1100	1.10	-180	1.5
9	1.57	1100	1.20	-180	1.5
10	1.70	1100	1.30	-180	1.5
11	1.82	1100	1.40	-180	1.5
12	1.94	1100	1.49	-180	1.5
13	2.06	1100	1.58	-180	1.5

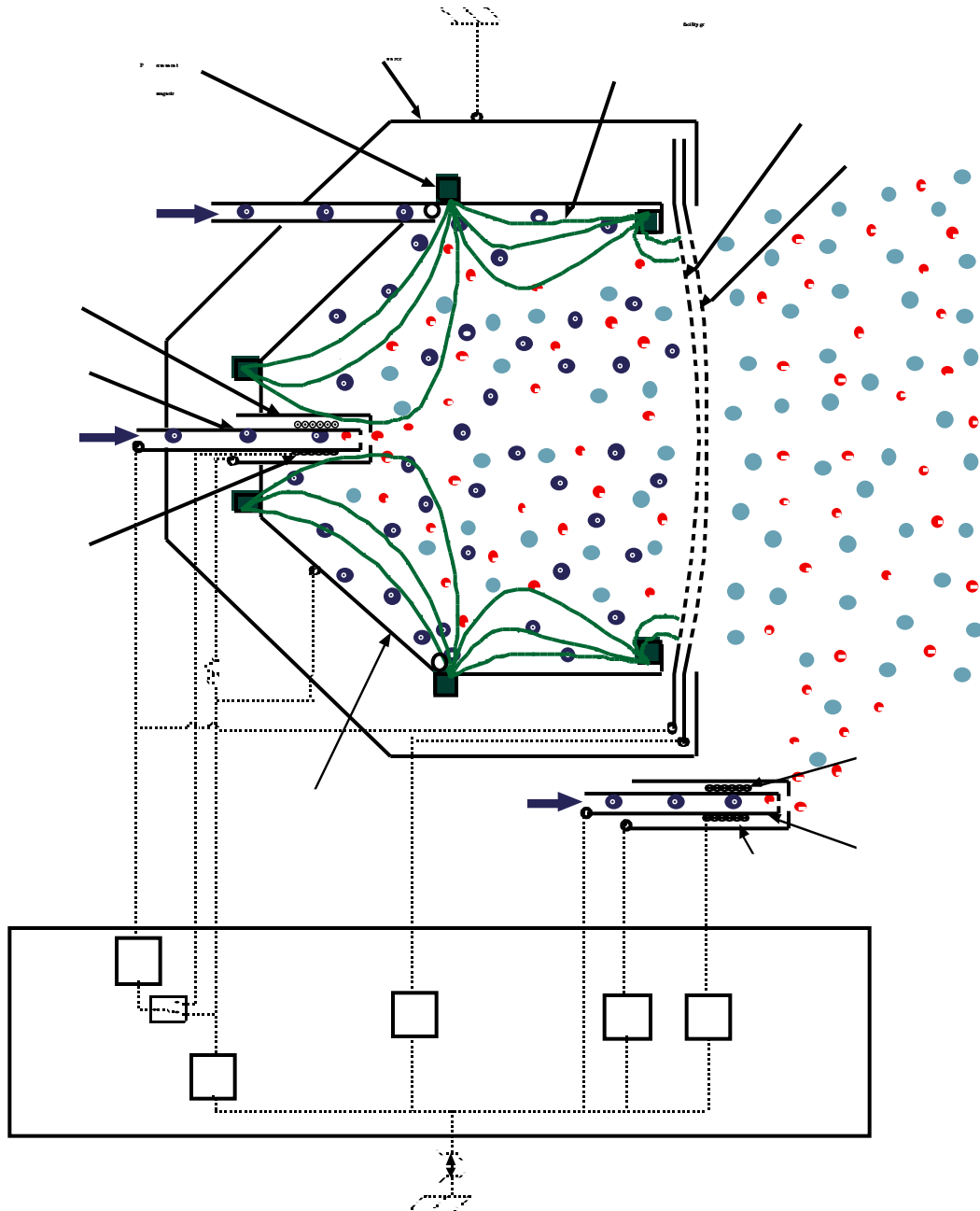


Figure 2.1: Schematic diagram of the NSTAR ion engine. Voltages given are approximate values corresponding to beginning of life, full power. They are given with respect to neutralizer common,  $\approx -2$  V with respect to spacecraft ground (in space) or  $\approx -12$  V with respect to facility ground. Schematic courtesy of J. Polk, JPL.

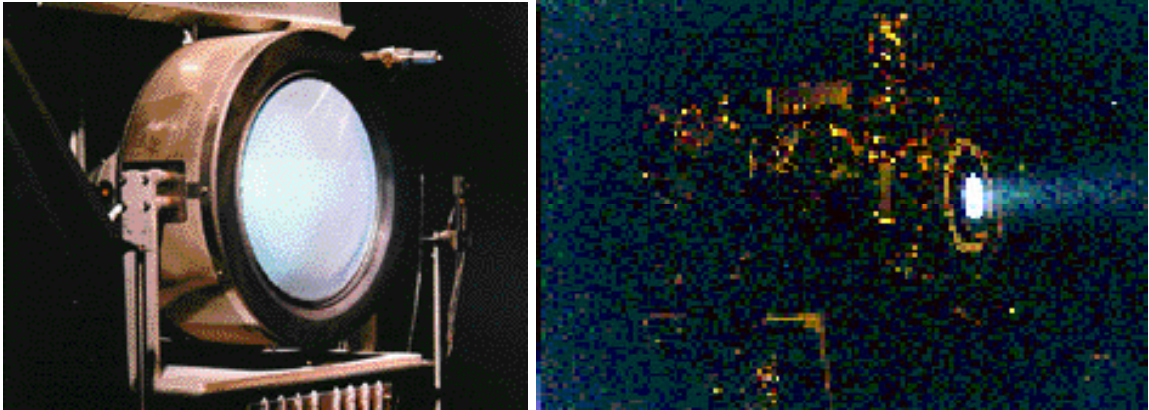


Figure 2.2: The NSTAR 30-cm ion engine; (a) engineering model thruster in 8200-hour wear test at JPL; (b) flight thruster on *Deep Space 1* during acceptance test at JPL.

the neutralizer from backstreaming into the discharge chamber. As a result from the processes described above, electrical power has been converted by the thruster into kinetic energy deposited into the working fluid—the plasma plume. Some ionized propellant atoms leak out of the discharge chamber through the grid apertures at thermal velocity.

Electrical and flow parameters for the NSTAR thruster at different throttle levels are provided in Table 2.1. Both cathode mass flow rates are almost identical and only the discharge cathode mass flow rate is indicated in the table. Both discharge and neutralizer cathodes are enclosed inside keeper electrodes whose roles are to facilitate the creation of the initial plasmas with local arcs.

As the engine operates, some of the ions produced in the discharge chamber, as well as those created further downstream in collisions between energetic ions and slow neutral atoms, impinge on a variety of engine parts. As a result of this ion bombardment, such engine parts will wear at a rate proportional to the impinging

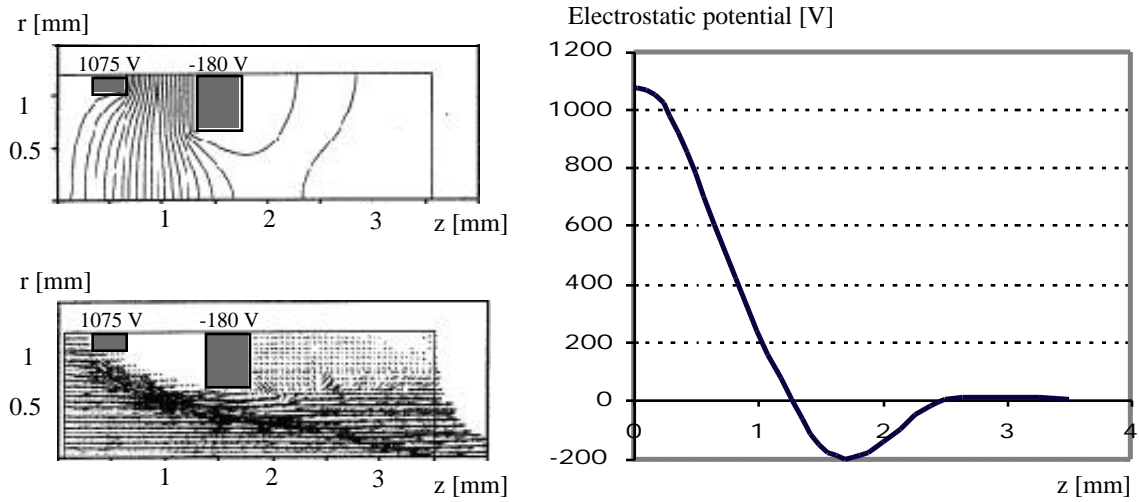


Figure 2.3: Electrostatic potential and ion current density in an individual ion optics aperture. Electrostatic potential contours (a) and ion current density vectors (b), courtesy J. Wang, JPL. Electrostatic potential vs. axial position along centerline (c).

ion current density and as a function of the ion kinetic energy.

## 2.2 Failure Modes

In the forty years since the first test of an electron-bombardment ion rocket was reported [36], extensive testing has been carried out on ion engines. Historically, eighteen distinct failure modes have been identified and reported in the literature (Ref. [37] and references therein). From the particular failure modes applicable to the NSTAR thruster and from the long-duration testing activity implemented in the NSTAR program, a total of ten damage-accumulation failure modes applicable to the NSTAR engine have been identified to date [29] and are listed below.

1. Electron-backstreaming due to enlargement of the accelerator grid apertures by ion sputtering.

2. Structural failure of the accelerator grid due to charge-exchange ion erosion.
3. Unclearable short between the screen and accelerator grids due to a flake of material formed from the deposition and subsequent flaking of sputtered material.
4. Structural failure of the screen grid due to erosion by ion sputtering.
5. Structural failure of the accelerator grid due to direct ion impingement from defocused beamlets caused by flakes of material on the screen grid.
6. Depletion of the cathode low-work-function material.
7. Cathode heater failure due to thermal cycling.
8. Unclearable short between the keeper electrode and the cathode due to a flake of material formed from the deposition of material sputtered off the cathode orifice plate.
9. Erosion of the keeper orifice plate resulting in its structural failure.
10. Erosion of the neutralizer orifice plate due to operation in plume mode for extended duration.

These damage-accumulation modes can be grouped in three categories, depending on whether they are primarily related to accelerator grid erosion, screen grid erosion, or cathode end of life.

### **2.2.1 Accelerator Grid Erosion**

Failure modes 1–3 have the same root cause, *i.e.*, sputtering of the molybdenum accelerator grid by, mostly, charge-exchange ions with kinetic energies up to 180

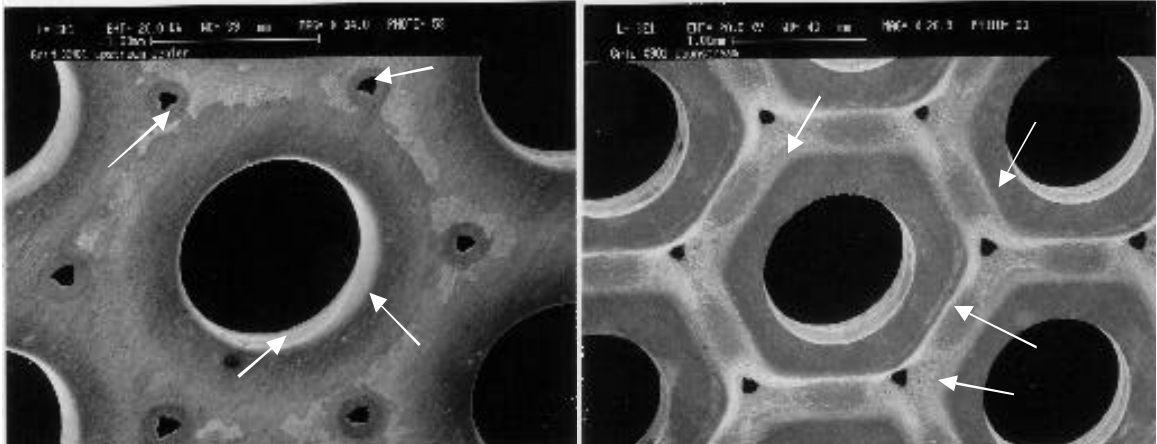


Figure 2.4: Accelerator grid erosion pattern for a 10-kW xenon ion thruster; (a) upstream; and (b) downstream side of the grid electrode. From Ref. [47].

eV, corresponding to the accelerator grid voltage. The charge-exchange ions are created within or near the negative potential well in the vicinity of the accelerator grid (Fig. 2.3) by charge-exchange collisions between energetic primary ions and slow, neutral atoms. They are produced at a rate proportional to the neutral gas density and the number density of the beam ions. This phenomenon and the distinction between space-based and ground-based operations will be discussed further in Chapter 7. Erosion of the extraction grid system by charge-exchange ions has been the subject of numerous discussions in the last ten years [38–46]. The difference between failure modes 2–4 lies with which consequence arises first from the sputtering process. Figure 2.4 details the erosion pattern observed on the accelerator grid after the first extended operation of a high-power xenon ion thruster [47].

The first failure mode is the result of the enlargement of the accelerator grid holes by the erosion process. For a given ion current density through the aperture and screen grid voltage, the negative voltage to be applied to the accelerator grid-electrode in

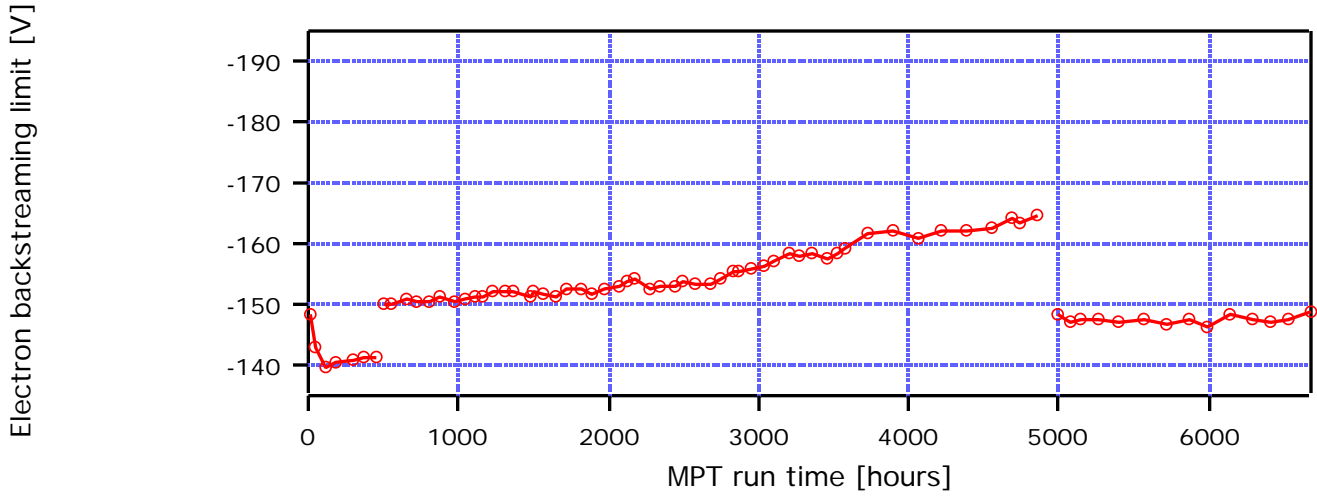


Figure 2.5: Electron backstreaming limit vs. time during NSTAR mission profile test [49]. The power level was TH12 until 448 hours, then TH15 until 4937 hours, and TH8 afterwards.

order to prevent neutralizer-emitted electrons from backstreaming into the discharge chamber increases as the aperture diameter increases. Once this voltage exceeds the capability of the power supply on board the spacecraft ( $-250$  V on *Deep Space 1*), the engine cannot maintain its full operating capability. During engine operation, the progress of the accelerator grid hole enlargement process can be monitored by decreasing the accelerator grid voltage (in magnitude), thus progressively allowing electrons to backstream into the discharge chamber. As a result, because the beam power supply cannot distinguish extracted ions from backstreaming electrons, the apparent discharge loss—the cost of producing the extracted beam current—is seen to decrease. The accelerator grid voltage at which the discharge loss decreases by 1% is defined as the backstreaming limit [48], and is shown against hours of operation in Fig. 2.5.

The second failure mode supposes that the erosion by ion bombardment of the accelerator grid is allowed to proceed until structural failure of that electrode. This

occurs when the “pits and grooves” charge-exchange erosion pattern (Fig. 2.4) wears completely through the grids. An analytical model of accelerator grid failure can be found in Ref. [50].

Failure mode 3 will be caused primarily by metallic flakes formed on the screen grid by deposition of material sputtered from the accelerator grid, although it can also conceivably be caused by flakes formed on the discharge chamber walls that spalled and migrated toward the ion optics system under the small acceleration experienced during engine operation in space. Such flakes can short the 0.6-mm (at beginning of life and at room temperature) inter-electrode gap and cause an engine failure. Although the NSTAR system includes a grid-clearing circuit that applies a 30-second pulse of 4 A in the short to vaporize it [51], a failure caused by the presence of a flake too large—or with too low a resistance—to be cleared constitutes a credible risk. As a final note on grid shorts, a distinction needs to be made between shorts that result from the wear processes discussed in these pages, and single-event failures due to shorts caused by non-wear-related debris. Such a particulate caused the initial short on the flight thruster at the beginning of the *Deep Space 1* mission. Details about this incident and the recovery are provided in Ref. [12].

In addition to the electron backstreaming limit, mentioned earlier, two other periodic measurements using the engine electrical parameters provide indirect diagnostics of the ion optics erosion processes during long-duration testing: perveance limit and screen grid transparency to ions.

The perveance limit is a measure of how well the grid electrodes are focusing the ions extracted from the discharge chamber. It is measured by progressively defocusing the beam, *i.e.*, by reducing the screen grid voltage  $V_s$ , while monitoring the increase in ion current  $I_a$  collected by the downstream accelerator grid. Once the slope of

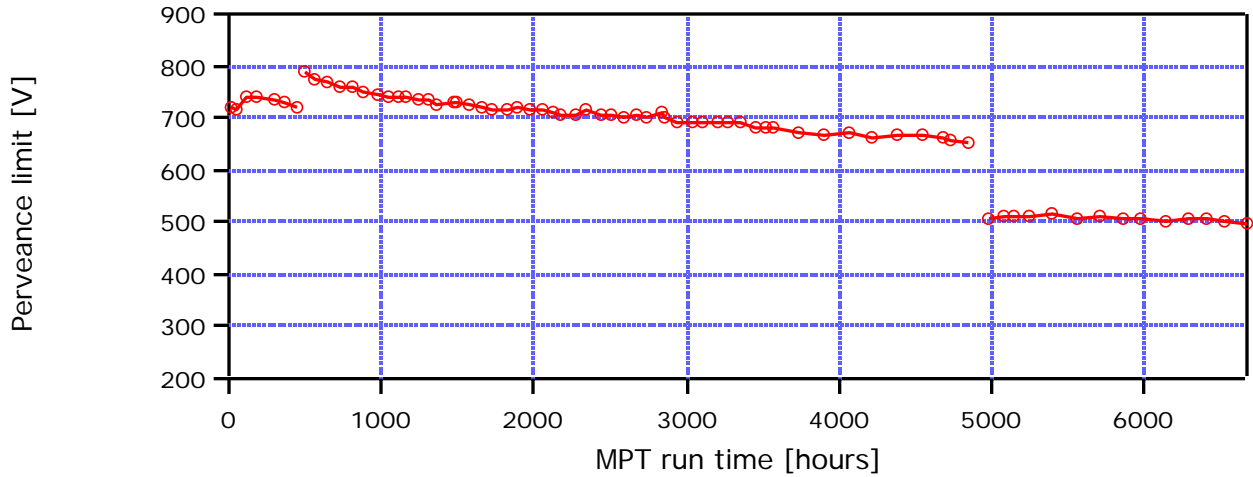


Figure 2.6: Perveance limit vs. time during NSTAR mission profile test. [49]. The power level was TH12 until 448 hours, then TH15 until 4937 hours, and TH8 afterwards.

the  $I_a$ - $V_s$  characteristic has reached a value of  $-0.02$  mA/V the screen grid potential is said to have reached the perveance limit [48]. The margin between the operating value of  $V_s$  and the perveance limit—the perveance margin—indicates how far the beamlets are from impinging directly on the accelerator grid, a condition that would lead to extremely rapid accelerator grid deterioration. A decreasing perveance limit—or increasing perveance margin—provides an indication of accelerator grid aperture enlargement. An example plot of perveance limit versus hours of operation is shown in Fig. 2.6.

Screen grid transparency to ions is a measure of the effectiveness of the ion optics to extract the beam. It is measured by biasing the screen grid to  $-20$  V with respect to cathode potential, so that discharge chamber electrons are prevented from contributing a current to the screen grid. The sum of the measured screen grid current and the extracted beam current is the total current directed toward the screen grid. The screen grid transparency is then defined as the ratio of the extracted beam current

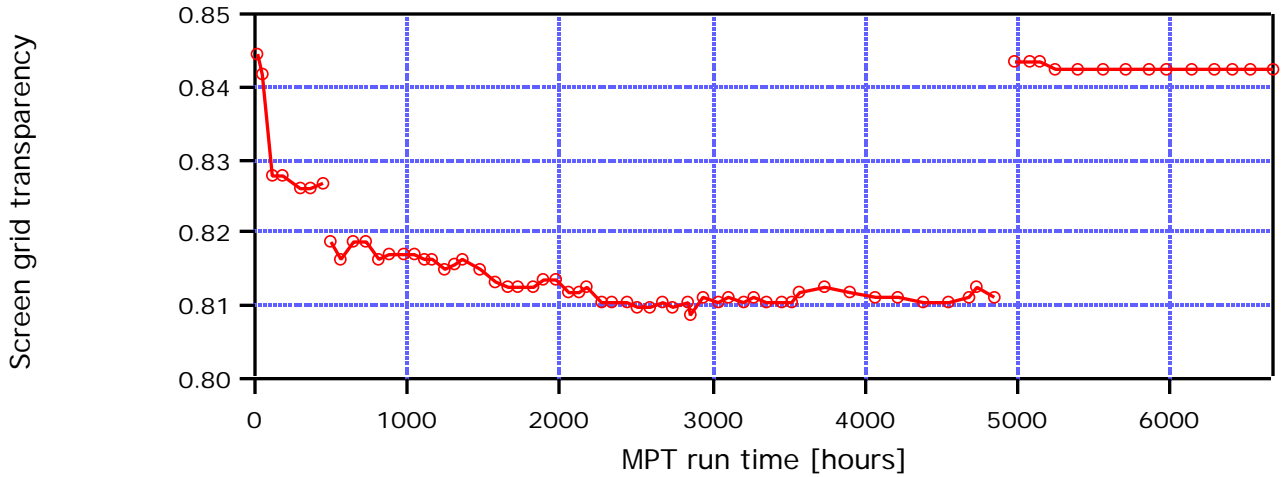


Figure 2.7: Screen grid transparency to ions vs. time during NSTAR mission profile test [49]. The power level was TH12 until 448 hours, then TH15 until 4937 hours, and TH8 afterwards.

to the total current directed toward the screen grid [48]. A decreasing screen grid transparency to ions over time can be an indicator of sputter-deposited material on the downstream side of the screen grid from accelerator grid erosion (a condition that can lead to failure mode 3). Such a trend may also be related to accelerator grid aperture enlargement. An example is shown in Fig. 2.7.

## 2.2.2 Screen Grid Erosion

Severe screen grid erosion (mode 4) was reported after a 2000-hour test [52]. This problem was addressed by decreasing the nominal discharge voltage to 25 V and avoiding low flow, high propellant utilization efficiencies.

The first step resulted in a lower voltage difference between the screen grid and discharge chamber plasma, thus reducing the energy of the bombarding ions, while also contributing to lower the ratio of doubly- to singly-charged ions produced in the discharge. Doubly-charged xenon ions produced in the discharge chamber strike the

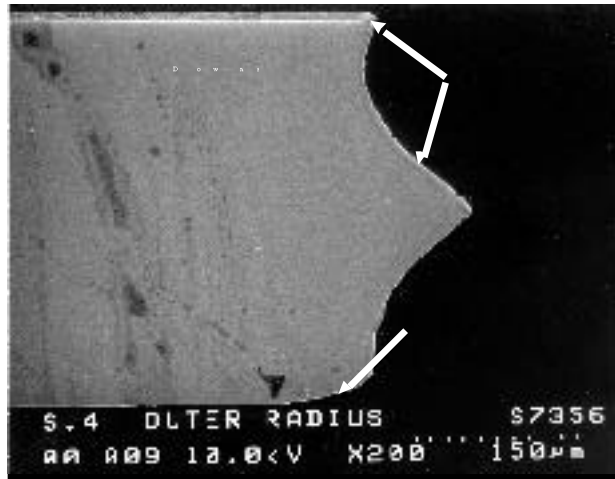


Figure 2.8: Cross-section of screen grid webbing after 8200-hour wear test.

screen grid—or cathode components—with twice the energy of single ions. The second step—avoiding “lean” operating conditions—ensured that the discharge voltage could be kept near its lowered nominal value throughout the engine throttling range and contributed to ensure a low fraction of doubly- to singly-charged ions [53]. Subsequent tests showed that screen grid erosion had been dramatically reduced [54,55], but this failure mode does remain a candidate. Fig. 2.8 shows the erosion pattern of an individual screen grid hole. Once again, this failure mode originates in an erosion process involving low-energy xenon ions on a molybdenum surface.

Failure mode 5 is caused by the formation of flakes of sputtered material, mostly from the screen grid, redeposited on the discharge chamber surfaces [52]. Such flakes can eventually spall off the annular wall and migrate to the screen grid where they can cause individual beamlets to become defocused. This can lead to direct impingement on the accelerator grid of high-energy ( $\approx 1.3$  keV) xenon ions, which in turn can lead to rapid structural or functional failure.

This failure mode has been addressed in part by tying the screen grid to cathode

potential instead of letting it float below cathode potential, thus decreasing screen grid erosion and lowering the amount of eroded material, and in part by adding a fine sputter-containment stainless steel mesh approximately 760  $\mu\text{m}$  thick over the titanium cylindrical and conical sections of the discharge chamber to preclude spalling of deposited films [52]. Although these modifications greatly mitigated the risk, this failure mode does however remain a credible failure mode for the NSTAR thruster [37]. The sputtering processes in this failure mode involve singly- and multiply-charged xenon ions on molybdenum at an energy corresponding to the discharge voltage, *i.e.*, 25 V nominally. Although this mode is considered here to be related to screen grid erosion because this electrode is the source of the sputtered material, it should be noted that defocused beamlets can also be caused by flakes of molybdenum sputter-deposited on the downstream side of the screen grid due to accelerator grid erosion [29], as shown in Fig. 2.8.

To conclude with the failure modes primarily associated with grid erosion, it can be noted that monitoring the engine discharge power—the cost of producing the extracted ions—at constant beam current, can provide additional information about component wear (Fig. 2.9). In particular, increased accelerator grid hole diameter will induce an increased “cold flow” loss of neutral propellant atoms through the ion optics that contain the discharge plasma, while a decreased screen grid transparency would mean that more ions are collected at the screen grid. Both conditions would be expected to be revealed by an increase in the discharge power necessary to maintain the regulated beam current [48, 49, 55]. A complete discharge chamber performance model was developed by Brophy [56] and the effect of engine wear on performance is discussed further in Ref. [57].

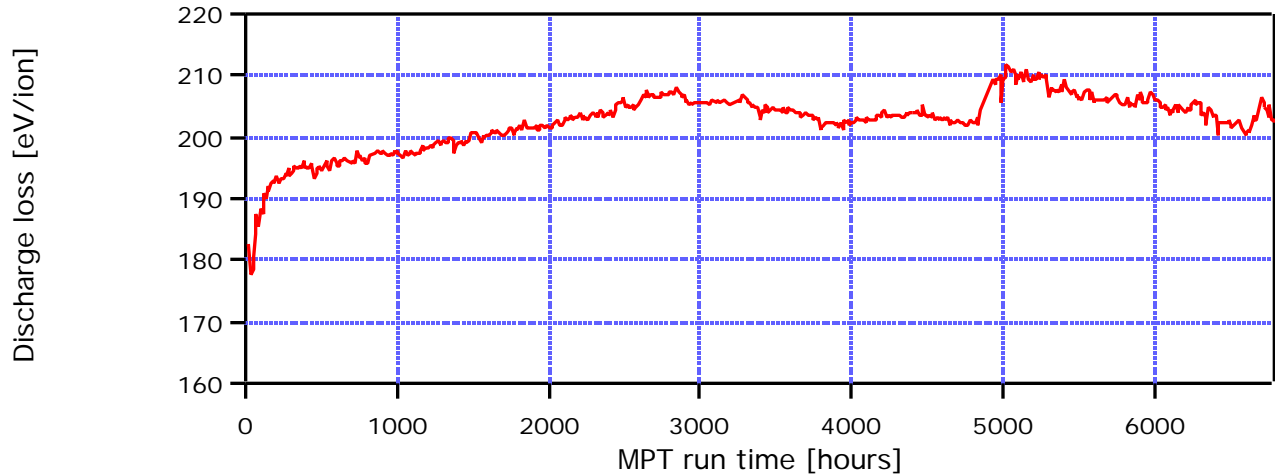


Figure 2.9: Discharge loss vs. time during NSTAR mission profile test [49]. The power level was TH12 until 448 hours, then TH15 until 4937 hours, and TH8 afterwards.

### 2.2.3 Cathode End of Life

The discharge and neutralizer hollow cathodes can constitute single-point failures in electron-bombardment ion engines. The life-limiting phenomena associated with the cathodes, which can result in failure modes 6–10, are briefly explained below.

During normal operation of a hollow cathode, a hot impregnated tungsten dispenser releases barium to the surface of the cathode to keep the work function low and allow for high emission currents, approximately 11–14 A for the NSTAR engine. Failure mode 6 results when the low-work-function material in the cathode has been depleted. Although a total emitted charge capability of 334 kA-hr has been demonstrated on a xenon hollow cathode [58, 59], suggesting a lifetime in the range 30400–23900 hours, several important differences in the ion engine system environment (voltage supply, operating temperature and flow rates) suggest that this estimate remains highly uncertain for NSTAR [29].

A cathode heater failure (mode 7) can be produced by a large number of on/off

cycles. The neutralizer heater and the discharge cathode heater are required at the beginning of the thruster start sequence for about 210 seconds before the cathodes are ignited and can operate in a self-heating mode [49, 55]. Although significant ion bombardment-induced erosion of the discharge cathode heater has been reported [52], this failure mode is likely to be credible only for missions requiring thousands of thermal cycles and is primarily a materials issue [29, 37].

Failure modes 8–10 stem from the process of erosion by ion bombardment. During engine operation, the discharge cathode is subject to bombardment by ions from the discharge chamber plasma, while the neutralizer cathode is damaged by the ions present in the cathode plume. The behavior of xenon hollow cathodes is complex and still poorly understood, and in particular much work is still needed to understand the formation mechanisms of ions with energies greater than the cathode keeper potential (12–15 V for the neutralizer keeper). Such ions, nevertheless, are likely to be responsible for the cathode erosion mechanism. While their presence has been suggested by experimental data [60–63], two previously proposed mechanisms for the production of high-velocity ions, the z-pinch and potential hill models, have been found to “both be incorrect or insufficient for a full explanation” [64].

Failure mode 8 can occur on either the discharge or the neutralizer cathode when flakes are formed by the material sputtered from the cathode orifice plate due to ion-bombardment erosion and deposited on the upstream side of the keeper. This situation can result in the failure of the cathode if such a metallic flake detaches from the surface and shorts the cathode itself and the cathode keeper. Thin deposits comprised primarily of tungsten were found at the upstream edge of the discharge and neutralizer cathode keeper orifice in the post-test analyses of the 8200-hour NSTAR life demonstration test. The deposits, shown in Fig. 2.10, were of up to 50  $\mu\text{m}$  in

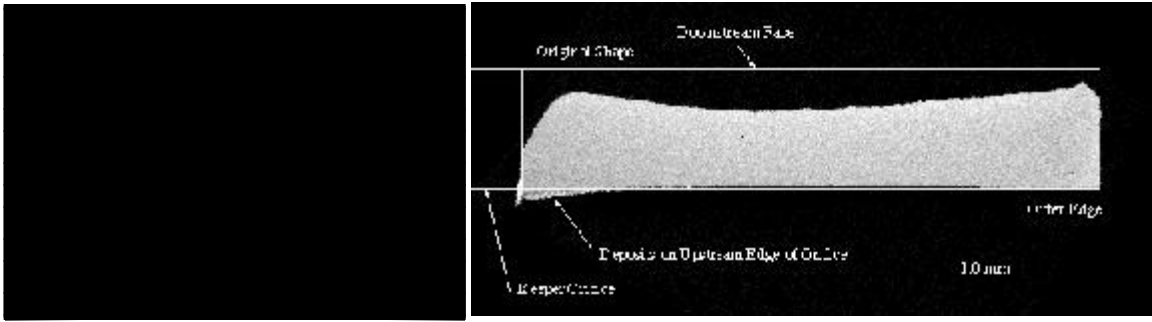


Figure 2.10: Cathode erosion at end of engineering model thruster 8200-hour LDT. (a) cathode assembly; (b) Cross-section of cathode keeper electrode [65].

thickness for the discharge cathode [55].

The tungsten orifice plate and molybdenum keeper electrode for both the neutralizer and the discharge chamber cathodes are subject to ion-bombardment erosion. Cathode orifice plates exhibited significant to severe wear in an earlier long-duration test of the NSTAR ion thruster [52] but the subsequent addition of a keeper electrode in front of both hollow cathodes seems to have mitigated this problem [55]. The keeper electrode for both cathodes are now however sites of significant wear (failure mode 9), and particularly in the case of the discharge cathode [55]. Figs. 2.10 and 2.11 show examples of cathode damage by ion-bombardment erosion in two different wear tests. Recently, the ongoing Mission Profile Test (MPT) of the *Deep Space 1* spare flight thruster has suggested increased cathode erosion at throttled conditions [65]. Experiments are currently underway at JPL to investigate precisely what conditions lead to increased cathode erosion rates.

Finally, failure mode 10 stems from operating the neutralizer cathode in a mode—the plume mode—characterized by a larger keeper voltage and large keeper voltage oscillations [48, 49, 55]. It is desirable to keep as low a xenon flow rate as possi-

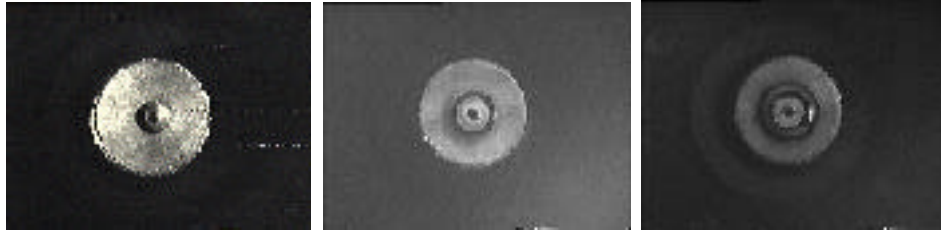


Figure 2.11: Cathode erosion during on-going spare flight thruster MPT after (a) 447 hours; (b) 9473 hours; and (c) 12342 hours of operation [65].

ble through the neutralizer because the propellant expended is not accelerated and therefore does not contribute to the generation of thrust—indeed, increasing the neutralizer flow rate amounts to decreasing the specific impulse at constant thrust and constant power. As the neutralizer flow rate is decreased, however, a transition from the normal, steady “spot-mode” operation to plume mode will occur. The flow rate at which this mode transition is observed has been found to increase as the engine ages [55]. Failure mode 10 can therefore be avoided by keeping an appropriate propellant flow rate through the neutralizer, which may be done at the expense of thruster performance after extended lifetimes [29].

In conclusion, while virtually all single-event and most damage-accumulation failure modes historically observed in ion engines can now be avoided due to improved design, manufacturing processes, acceptance testing, and operating conditions and procedures, ten distinct damage-accumulation processes can noticeably affect the NSTAR engine performance over its lifetime and are expected to be the primary life-limiting phenomena [29]. Out of these ten competing failure modes, eight are related to low-energy sputtering of (mostly molybdenum) engine components by xenon ions.

## 2.3 Assessment of Engine Lifetime by Analysis and Testing

In order to allow for realistic mission planning and to give flight program managers the confidence to use the technology, quantitative assessments of the failure risk of the NSTAR ion engine as a function of mission life are required. This can be accomplished by a statistical approach combining both long duration testing and engineering analysis.

Performance of a large number of long duration (typically one- to several-year) engine tests alone to demonstrate engine lifetime is highly impractical because of unacceptable costs and prohibitive delays to complete system development and qualification. In particular, it requires a frozen design over the entire validation cycle. In addition, most data from tests or flights consist of “trials” with few or no failures, which renders the amount of (non-failure) data necessary for such a purely statistical approach extremely large. This is even particularly more so in the case of damage-accumulation failures, as opposed to event consequent failures with usually smaller variability in their distribution. For instance, in order to have even 50% confidence that the probability of failure of a system is no larger than 1/100 over a service life expressed as  $M$  missions,  $69M$  mission simulation zero-failure tests would have to be conducted [66]. High service life reliability at high confidence therefore clearly cannot be demonstrated by testing alone. On the other hand, deterministic methods of engineering analyses are not sufficiently credible, in particular in situations where the wear-out mechanisms are not fully understood and the system’s independent operating parameters are not known with sufficient certainty. Such methods can only yield “worst-case scenario” results and, as a consequence, lead to overly conservative

designs.

The methodology of failure risk assessment by analysis *and* testing incorporates all of the available information from both test experience and engineering analysis, and is described in Ref. [66]. It implements a probabilistic treatment that allows the uncertainties in both the independent parameters and the wear-out mechanisms to be interpreted into a quantified failure risk. Here the uncertainties in the engine operating parameters come from the tolerances on the real-world propellant flow controllers or power supplies, while the uncertainties on the wear-out mechanisms come from a lack of knowledge about physical phenomena. The statistical analysis of reliability data with few or no failures is based on the fit of a Weibull distribution to the reliability data of the system and the calculation of estimates and confidence limits for the corresponding Weibull parameters [67].

The first step is to generate distributions that describe the dependent parameters given the known tolerances in the independent parameters. For example, the NSTAR thruster has seven independent (controlled) parameters and seven dependent parameters, shown in Table 2.2 along with five calculated performance parameters of interest to mission designers. This step requires knowledge of the relative sensitivities of the dependent parameters to the engine independent parameters over their respective range. This information was gained by a sensitivity analysis implementing the Taguchi approach to the design of experiments (see for example Ref. [68]). As a result, the uncertain parameters are entered in the equations describing erosion models as distributions rather than specified, exact numbers, with variabilities that reflect the corresponding lack of knowledge. For instance, sputter yields can be evaluated by means of a variety of existing, direct or indirect experimental data interpolated or extrapolated using different theoretical or semi-empirical methods, or by compu-

Independent parameters for engine	Dependent parameters	
	Engine	Performance
Beam supply voltage (V)	Beam voltage (V)	Thrust (mN)
Beam current (A)	Accel. grid current (mA)	Specific impulse (s)
Accelerator voltage (V)	Discharge voltage (V)	Efficiency
Neutralizer keeper current (A)	Discharge current (A)	Disch. loss (eV/ion)
Main flow rate (sccm)	Neut. keeper voltage (V)	Propellant efficiency
Cathode flow rate (sccm)	Coupling voltage (V)	
Neutralizer flow rate (sccm)	Power (kW)	

Table 2.2: NSTAR engine and performance parameters, after Ref. [55].

tational models. The uncertainty range used in the erosion model will need to cover the corresponding range of possible values.

The distributions associated with the input parameters in the model are then propagated by the model to generate, for the particular failure mode described by that model, a probability density function where the time to failure is the random variable. This density function can then be normalized and integrated to generate the probability distribution function for the time to failure, for that particular failure mode. Thus, for any given run time of the thruster, a conditional failure risk has been quantified that reflects the current state of knowledge of the input parameters to the engineering model [37]. As a last step, the failure risks corresponding to each modelled failure mode can be aggregated for a given mission profile to generate the failure risk for the thruster for a particular mission.

The method for probabilistic risk assessments is summarized in Fig. 2.12, and Fig. 2.13 shows the screen grid structural failure risk as a function of engine operating life (expressed in total propellant throughput) at different throttle levels. The analytical model used in this example—screen grid structural failure—is detailed in Ref. [37]. To date, analytical models that lend themselves to probabilistic modeling

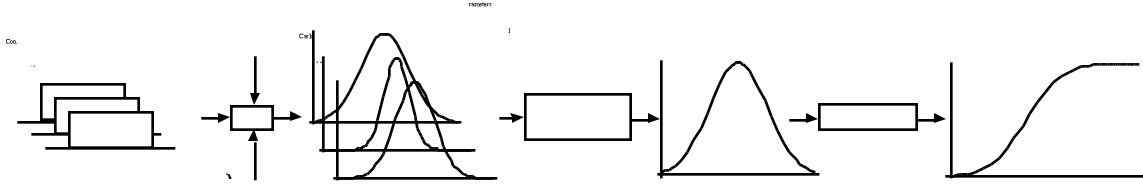


Figure 2.12: Flow chart of probabilistic risk assessment.

have been developed only for failure modes 2 and 4, *i.e.*, structural failure of the accelerator and screen grids, respectively. This methodology has been implemented on example failure modes by the NSTAR program to assess the service life of the NSTAR ion engine [29, 32, 37, 69], and to estimate the risk of failure for a typical mission profile [70].

It is noteworthy that the effect of a greater uncertainty, *i.e.*, a broader distribution for a given parameter of the model of a failure mode, is to in turn broaden the probability density function for the time to failure. This results in an increase of the conditional failure risk for this mode at a given run time, in the low-risk tail of the curve. The primary risk drivers for the failure modes addressed in the NSTAR program are the uncertainties about eroded geometry at failure, impingement ion current density and energy distributions, and net sputter yield [69].

## 2.4 Summary

Ion engines, such as the NSTAR electron-bombardment ion engine, are subject to complex erosion phenomena that accumulate during engine operation and result in decreased End-of-Life (EOL) performance, and can ultimately lead to engine failure.

Eight of the ten currently identified damage-accumulation failure modes are the

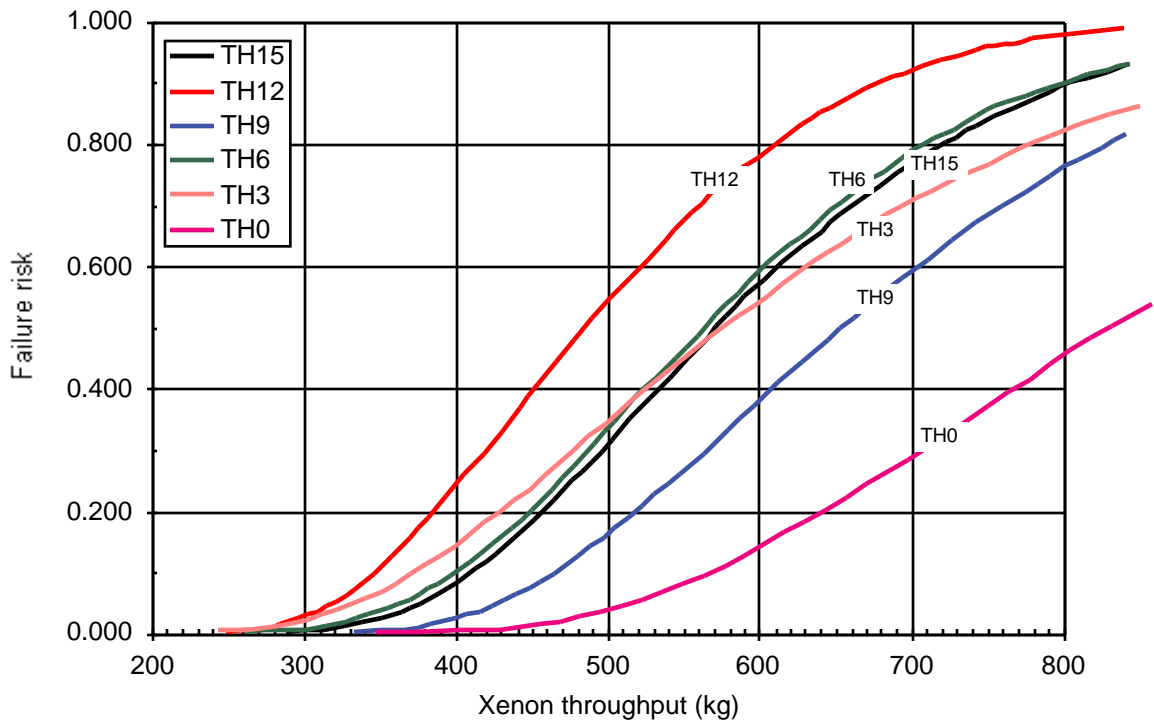


Figure 2.13: Screen grid structural failure risk vs. engine propellant throughput, after [65]. At the worst throttling level for this failure mode (TH12), 90% of failures will occur after processing more than 350 kg of propellant through the engine.

direct result of low-energy ion bombardment of engine component surfaces. In order to meet the increasing demands for improved engine lifetime and avoid overly conservative design points that sacrifice mission objectives, probabilistic techniques are necessary to assess the failure risk as a function of mission life. The risks have been shown to be driven by the uncertainties associated with the engine independent operating parameters and the models describing the physics of failure. The following chapters address the latter risk driver, and thus attempt to reduce the uncertainty on the wear-out mechanisms and resultant erosion rates involved with the leading failure modes. The experiments and modelling work described in this dissertation, however, are but a modest part of a broader effort to understand and accurately predict ion engine wear processes. The entire effort makes use of a total of seven long-duration tests carried out since 1988, in-space flight data from the *Deep Space 1* spacecraft, probabilistic analyses, and three-dimensional particle-in-cell code simulations [71].

# Chapter 3

## Physics of Sputtering by Energetic Ions

In this chapter we discuss the sputtering mechanisms relevant to the erosion processes of electron-bombardment xenon ion engines. A brief description of the physics and relevant definitions are also included for use in the subsequent chapters. Because the use of Lindhard-Scharff-Schiott (LSS) units can be somewhat misleading to the non-expert, a special effort is made to keep the dimensions transparent in Chapters 3 and 4. The reader is also referred to the nomenclature when in doubt about the dimensions of a given quantity. This chapter is concluded with a discussion of the threshold energy for sputtering.

### 3.1 Description and Historical Applications

The interaction between an incident particle and a solid target can give rise to many different phenomena, mostly dictated by the energy of the projectile particle [72]. At extremely low energy ( $<5$  eV), an incoming noble-gas atom may be backscattered, or

may come to thermal equilibrium with the surface before subsequently evaporating. The effect of such low-energy particles, *e.g.*, constituents of the outer atmosphere impinging on spacecraft surfaces in low Earth orbit, are negligibly small.

When the kinetic energy of the incoming particles exceeds the *lattice displacement energy*  $U_d$  of the target atoms—the minimum energy to knock a target atom far enough into the lattice so that it will not immediately hop back into its original site, about 15–40 eV for most metals [73]—atoms of the lattice may be pushed into new positions, causing surface migrations of atoms and surface damage. Displaced atoms lose an energy corresponding to the *lattice* (or bulk) *binding energy*—the energy of a lattice site, or vacancy formation energy, usually 1–2 eV [73]. When a surface atom is given an energy with a component normal to the surface greater than the *surface binding energy*  $U_b$ —the energy holding a surface atom to the lattice, less than 10 eV [73]—it will be ejected into the gas phase in a process called *physical sputtering*. Since ion bombardment can create a surface that is far from its thermodynamic equilibrium, *i.e.*, with metastable surface phases, the impinging particles can also induce a chemical reaction which produces an unstable compound at the surface: this is the concept of *chemical sputtering*.

The erosion due to physical sputtering is described by the sputtering yield,  $Y$ , a *statistical variable* defined as the mean number of atoms removed from a solid target per incident particle:

$$Y = \frac{\text{number of atoms removed}}{\text{number of incident particles}} \quad (3.1)$$

Because at such energies ( $\sim 10$  eV–10 keV), in general, the potential energy of the incoming particle will go into electron transitions while the kinetic energy primarily goes into lattice-atom vibrations or displacements [72], physical sputtering effects are

not expected to differ between ions and neutral atoms. In addition, at low energies, a positively charged ion approaching a metallic surface is typically expected to be neutralized within 4–6 Å from the surface, while collisional interaction distances are around 1 Å [74,75]. For this reason, the term “ion” when mentioned in the context of surface sputtering is really used as a synonym for “primary projectile” and does not bear any meaning as to the charge state of the particle.

As the kinetic energy of the projectile particles reaches the 100–1000-eV range, kinetic emission of gamma (secondary) electrons starts being added to the potential (Auger) emissions. At yet higher energies (well into the keV-range), the scattering cross-sections become so small that the collision cascades within the bulk of the target material occur far from the surface. Sputtering, a surface atomic scale process, thus becomes first very insensitive to particle energy, and then actually decreases with increasing energy. Finally, at MeV energies, the processes involved enter the realm of radiation damage [72].

A great amount of research on sputtering over the last five decades has been motivated by interest in a great variety of subjects [76]: in fusion energy research, sputtering raises the concerns of reactor wall erosion and plasma contamination; in micro-electronics, sputter deposition or etching are desirable fabrication or surface modification processes; in surface analysis, depth profiling, composition and structure analysis are useful tools that result from sputtering processes. For the most part however, this research has been focused on high-energy (greater than a few keV) sputtering yields. In particular, the sputtering mechanisms for light ions first received attention from attempts at understanding the erosion of planetary surfaces by the solar wind [77,78] or investigations of the ion impact desorption of surface impurities by hydrogen plasmas in fusion technology [79,80]. There has been comparatively less

interest in very low-energy sputtering by heavy ions, a lack of data that is hindering our effort to understand and accurately predict the wear-out mechanisms and rates observed in electron-bombardment ion engines, and electric propulsion devices in general. As a result, low-energy heavy-ion sputtering yields to date are predicted by extrapolations from higher-energy measurements with the use of inherently uncertain semi-empirical formulae.

The ion-bombardment erosion caused by noble-gas ions on clean metal surfaces invokes physical sputtering. In the following sections we present an overview of the physical description of low-energy sputtering by energetic ions, measurement techniques, and results.

## **3.2 Theory of Physical Sputtering**

A quantitative treatment of physical sputtering requires an understanding of the energy transfer mechanisms in atomic collision and penetration phenomena. Depending on the regimes considered and the various degrees of approximation invoked, a detailed understanding of sputtering also requires physical inputs that include genuine surface and bulk properties, projectile kinetic (and possibly potential) energy and incidence angle, atomic masses of the collision partners and, perhaps most importantly, an accurate model of ion-atom and atom-atom interaction potentials.

### **3.2.1 Physics and Mechanisms**

As a starting approximation, we use a classical two-particle elastic scattering model to describe physical sputtering. We will see later in this chapter that an appropriate description of the collisional processes involved may require a more complex interaction

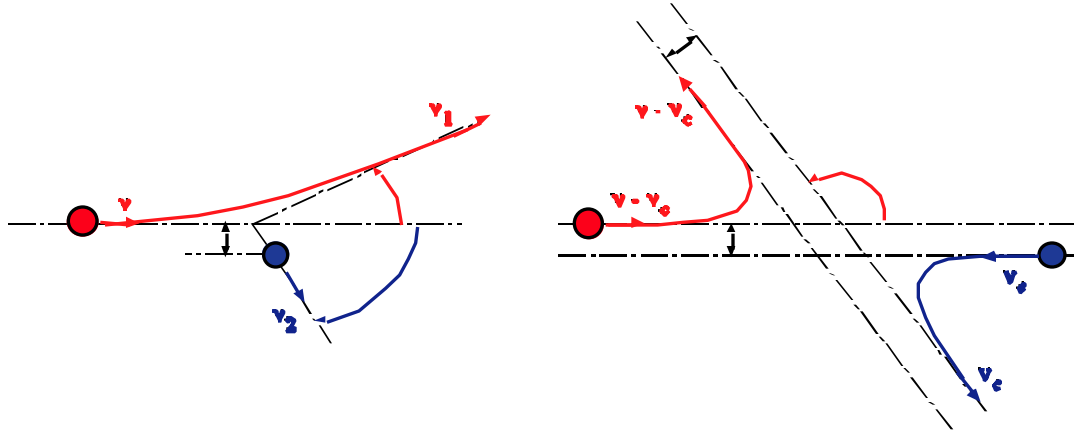


Figure 3.1: Classical two-particle scattering; (a) in laboratory coordinates, and (b) in barycentric coordinates.  $\mathbf{v}$ ,  $\mathbf{v}_1$ ,  $\mathbf{v}_2$  and  $\mathbf{v}_c$  are the velocity in the laboratory reference frame of, respectively, the incident particle before and after the collision, the target particle (assumed initially at rest) after the collision, and the center of mass of the two particles.

potential energy.

The energy  $T$  transferred by the incoming particle with energy  $E$  to the target particle is a result of elastic-collision theory (see for example Ref. [81]) dictated by the conservation laws of energy and (longitudinal and transversal) momentum

$$T = \gamma E \sin^2 \frac{\Theta}{2} \quad (3.2)$$

where  $\Theta$  is the scattering angle in the center-of-mass frame of reference for the two particles (Fig. 3.1), and

$$\gamma = \frac{4M_1M_2}{(M_1 + M_2)^2} \quad (3.3)$$

is the energy-transfer coefficient.  $M_1$  and  $M_2$  are the atomic masses of, respectively, the projectile and the target particle. In order to get the *cross-section* for the energy transferred, the probability for each final scattering angle is needed.

To obtain the details of the scattering trajectory, a static, central-force potential

field  $V(r)$  can be introduced so that  $\Theta$  is given by the integration of the single equation of motion along the collision path [81]

$$\Theta = \pi - \int_{-\infty}^{+\infty} \frac{b \, dr}{r^2 \left[ 1 - \frac{V(r)}{E_c} - \left( \frac{b}{r} \right)^2 \right]^{\frac{1}{2}}} \quad (3.4)$$

This is the general orbit equation for two-body central-force scattering, where  $E_c$  is the kinetic energy of the center of mass,  $b$  is the collision impact parameter (Fig. 3.1) and  $r$  is the distance between the two particles. It is valid as long as kinetic energy and momentum are conserved for the system, and as long as the central potential force is static and spherically symmetric. Armed with Eqs. 3.2 and 3.4, one can then proceed in principle to calculate the collision cascade exactly.

Sputtering by elastic collisions can have three regimes: the single knock-on, the linear cascade or the spike regime [82]. In single knock-on events, primary recoil atoms (PKA) receive an energy sufficient to get sputtered but not to generate recoil cascades; in linear cascades, recoil atoms generated by ion-atom collisions are given enough energy to generate secondary knock-on atoms (SKA) among the lattice atoms; and finally, in the spike regime, the density of recoil atoms in a limited region is such that most atoms are considered to be in motion.

The spike regime, or even the linear collision cascade regime, become less important at energies near threshold. Behrisch [83] summarized the possible sputtering mechanisms shown in Fig. 3.2. They are classified according to whether or not they require backscattering of the incoming ion from the interior of the target ( $S_{II}$  versus  $S_I$ ) and whether they require a collision cascade or not (1–4 versus 5–8). A final distinction is made between mechanisms where a surface atom or a bulk atom is ejected from the solid target. The diagram only shows those collisions that resulted in an atom overcoming the lattice displacement energy or the surface binding energy, but

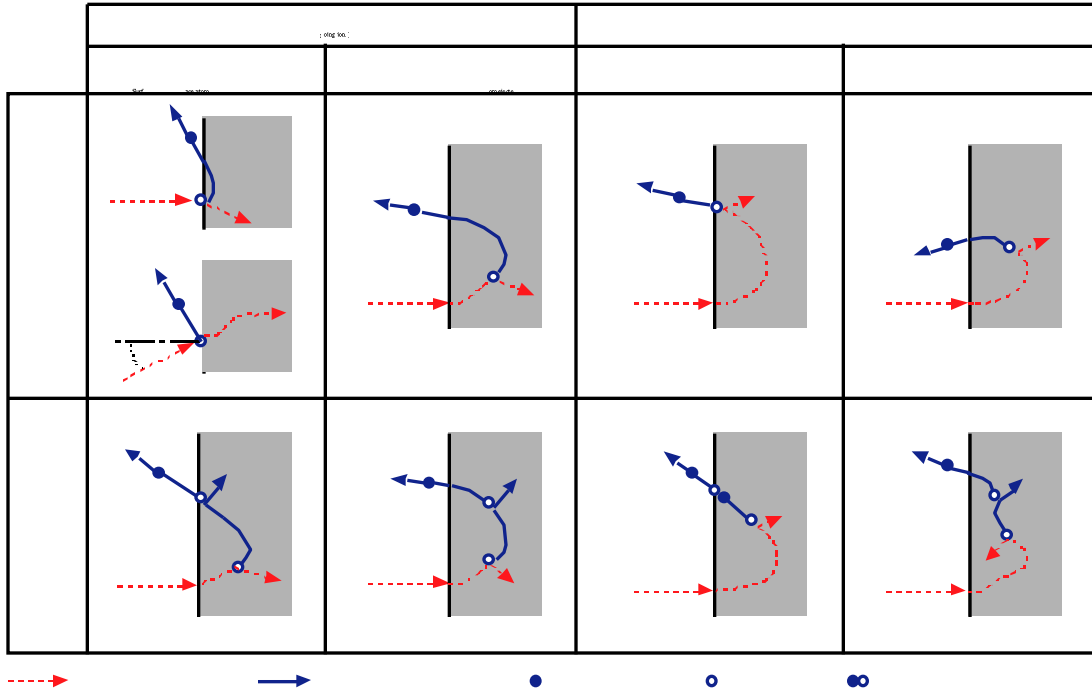


Figure 3.2: A “billiard-ball” description of sputtering mechanisms, after [83].

the curved trajectories in the target are of course the result of a number of small-angle scattering events.

Behrisch intended this description for sputtering by light ions, *i.e.*,  $M_1 < M_2$ , but the mechanisms also apply to heavy-ion sputtering. However, the processes involving an outgoing ion ( $S_{II}$ ) are less probable than with light ions since backscattering of a heavy ion (impossible for a head-on collision) will demand more scattering events. In the case of normal ion incidence, a minimum of two collisions are necessary for producing a sputtered atom. Indeed we recall, again from results of elastic-collision theory (Fig. 3.1), that unless *both* particles are in motion,  $0 \leq \phi \leq \frac{\pi}{2}$  and  $0 \leq \theta \leq \theta_{max}$  where

$$\theta_{max} = \begin{cases} \pi & \text{for } M_1 < M_2, \\ \arcsin \frac{M_2}{M_1} & \text{for } M_1 > M_2. \end{cases} \quad (3.5)$$

Thus, the scattering angle for an incoming heavy ion is necessarily smaller than  $\frac{\pi}{2}$ , and atoms sputtered as a result of (few) low-energy collisions are more likely to be sputtered at grazing incidences [84–87]. The important thing here is that for low-energy, heavy ions, the privileged sputtering mechanisms will be those that do not require backscattering of the ion from the interior of the target. Mechanisms  $S_1$  (Fig. 3.2) therefore are expected to dominate. As the energy is reduced near the threshold energy for sputtering, the collision cascades become extremely limited so that mechanisms 1 and 2 are the most likely to occur.

### 3.2.2 Interatomic Potential Models

We have shown that given an appropriate model of the interatomic potential  $V(r)$ , the collision cascade and the resulting sputtering yield can in principle be calculated exactly, under the assumptions that  $V(r)$  is stationary and spherically symmetric, and that the conservation laws for energy and momentum for the system of two particles hold.

Unfortunately, a pure classical two-particle elastic scattering model using the Coulomb repulsion between the nuclei alone only provides a reasonable description of physical sputtering at high energies, *i.e.*, when the *reduced energy*  $\epsilon$

$$\epsilon = \frac{M_2}{M_1 + M_2} \cdot \frac{a_I}{Z_1 Z_2 e^2} \cdot E \quad (3.6)$$

is much greater than unity [82]. In this definition,  $Z_1 e$  and  $Z_2 e$  are the nuclear charge of, respectively, the projectile and the target particles, expressed in LSS units, and  $\epsilon$  is dimensionless. The quantity  $a_I$  is the *screening radius* proposed by Lindhard [88], and may be defined as a function of the Bohr radius  $a_0 = 0.529 \text{ \AA}$  by

$$a_I = \frac{(9\pi^2/128)^{1/3}}{(Z_1^{2/3} + Z_2^{2/3})^{1/2}} a_0 \quad (3.7)$$

Projectile ( $M_1$ )	Target ( $M_2$ )				
	C (12)	Ti (48)	Mo (96)	Ta (181)	W (184)
Ar (40)	45.8	85.6	142.7	243.1	246.5
Kr (84)	199.7	289.7	415.3	629.9	636.5
Xe (131)	498.5	642.4	842.6	1177.8	1188.9

Table 3.1: Thomas-Fermi energy  $E_{TF} = E/\epsilon$ , in keV, for different projectile-target combinations.  $M_1$  and  $M_2$  are in amu.

The definition of a screening radius, based on the Sommerfeld approximation to the classical atomic model of Thomas-Fermi [89], reflects the fact that the transfer of energy from the projectile to the target is complicated by the complex electronic screening of the two nuclei by their electron distributions. The use of *reduced*—or Thomas-Fermi—coordinates allows the classical potentials to have the same form regardless of the atomic numbers, so that the potential distributions for all atoms, to a reasonable approximation [81], are universal. Energy is expressed in terms of the Thomas-Fermi energy unit  $E_{TF} = E/\epsilon$  and lengths are normalized by the screening radius  $a_I$ . Table 3.1 shows values of  $E_{TF}$  for different ion-atom combinations.

At energies such that  $\epsilon \gg 1$ , the scattering of the moving atom (or ion) by a stationary target atom is accurately described by a Rutherford scattering model using the Coulomb potential, such that the differential scattering cross-section

$$d\sigma(E, T) = \frac{d\sigma}{dT} dT$$

is given by [82]

$$d\sigma(E, T) = \pi \frac{M_1}{M_2} Z_1^2 Z_2^2 e^4 \frac{dT}{ET^2} \quad (3.8)$$

Since the collision cross-sections go as  $1/E$ , the particles are in effect “smaller” at high energy and the nuclei can approach closer to each other than the screening radius, so that the electronic screening of the nuclei is weak. At low energy, however, ( $\epsilon \lesssim 1$ ) the

physics of quantized screened Coulomb collisions must be considered and the potential describing the scattering events becomes much more complex. The most widely used universal models of interatomic interaction are the Sommerfeld approximation to the Thomas-Fermi potential [89], the Molière approximation [90], the Lenz-Jensen [91,92] and the Bohr potential [93]. In addition, and for the purpose of calculating the stopping and range of ions in solids with the Monte-Carlo simulation code TRIM, Ziegler, Biersack and Littmark developed the so-called “ZBL” potential [81]. Their detailed model for calculating interatomic potentials is given as

$$V = V_{nn} + V_{en} + V_{ee} + V_k + V_a \quad (3.9)$$

where “ $V_{nn}$  is the electrostatic potential energy between the nuclei,  $V_{ee}$  is the pure electrostatic interaction energy between the two electron distributions,  $V_{en}$  is the interaction energy between each nucleus and the other electron distribution,  $V_k$  is the increase in kinetic energy of the electrons in the overlap region due to Pauli excitation and  $V_a$  is the increase in exchange energy of these electrons” [81]. Thus, complete interatomic potentials between atoms can be defined, but they can also be rather complex. The three first terms on the right-hand side in Eq. 3.9 represent the screened Coulombic component, while the last two are related to electronic energy loss. Each of the classical potentials mentioned earlier can in fact be considered to be comprised of a Coulombic term along with a *screening function*  $\Phi$ .

### 3.2.3 Cross-Sections

A general differential cross-section formula is given in Ref. [73] that is valid for five different classical interatomic potentials: the Thomas-Fermi, Thomas-Fermi-Sommerfeld, Bohr, Lenz-Jensen, and Molière potentials. We only mention here the

form most commonly used in the theory of sputtering.

Based on the power approximation to the Thomas-Fermi model of interatomic interaction, *i.e.*, with a potential of the form  $V(r) \propto r^{-1/m}$  where  $m$  is a parameter, Lindhard [88] approximated the scattering cross-section at low energy ( $\epsilon \lesssim 1$ ) by the expression

$$d\sigma(E, T) \approx C_m E^{-m} T^{-1-m} dT \quad (3.10)$$

with

$$C_m = \frac{\pi}{2} \lambda_m a_I^2 \left( \frac{M_1}{M_2} \right)^m \left( \frac{2Z_1 Z_2 e^2}{a_I} \right)^{2m} \quad (3.11)$$

The parameter  $m$  is related to the steepness of the interatomic potential, and can also be interpreted as an indicator of projectile particle energy. Its value varies slowly from  $m = 1$  at high energy to  $m \approx 0$  at low energy. The values of  $\lambda_m$  are tabulated as a function of  $m$  in Ref. [82] and go from 0.5 for  $m = 1$  to 24 for  $m = 0$ . Eq. 3.10 thus approaches Eq. 3.8 at high energy ( $m = 1$ , *i.e.*, pure Rutherford scattering), and approaches the constant cross-section

$$d\sigma(E, T) \approx \frac{\pi}{2} \lambda_0 a_I^2 T^{-1} dT \quad (3.12)$$

at low energy ( $m \approx 0$ ). In Eqs. 3.8, 3.10 and 3.12, the energy  $T$  transferred to the target particle in the collision is bounded by the values allowed by Eq. 3.2.

An important quantity in the study of the interactions of energetic ions with solids is the *stopping cross-section*  $S(E)$ , a measure of the energy loss per unit distance travelled  $dx$  of the ion moving through the solid target of atomic number density  $N$ :

$$\frac{dE}{dx} = -NS(E) \quad (3.13)$$

The total stopping cross-section (also called *stopping power*),  $S(E)$ , is usually split into two components, the *nuclear* stopping cross-section  $S_n(E)$ —the elastic component—

and the *electronic* stopping cross-section  $S_e(E)$ —mostly inelastic energy loss.<sup>1</sup> The nuclear energy loss is treated independently of the electronic energy loss because at high velocities ( $\epsilon \gg 1$ ) the latter dominates the deceleration of the ion, while at lower energies  $S_n$  is the cross-section that is of interest in sputtering [82]. At low energies  $S_e$  becomes approximately proportional to the velocity and the cube root of the electronic density  $\rho$  in the medium [81]:

$$\frac{dE}{dx} \propto v\rho^{1/3} \quad (3.14)$$

The difficulty here resides in the choice of an appropriate atomic charge distribution, either consistent with classical atomic models for an isolated ion-atom pair, or consistent with the charge distribution of solid matter. Ref. [81] gives a comparison of classical versus solid-state screening functions for selected elements and crystal structures. The Molière and Lenz-Jensen atoms are found to be in reasonable agreement with the solid-state screening for the inner electronic shells, but beyond the L-shell (for reduced radii  $\gtrsim 4$ ) none of the classical screening functions adequately approach solid-state screening.

The nuclear stopping power,  $S_n$ , is the average energy transferred in elastic collisions when summed over all impact parameters

$$S_n(E) = \int_0^\infty T d\sigma(E, T) \quad (3.15)$$

The nuclear stopping power then depends on the atomic model used to describe the interaction, and in particular on the form adopted for the screened Coulomb interac-

---

<sup>1</sup>The terms *electronic* and *inelastic*, when referring to energy loss, are often used interchangeably in the literature, but they are not exactly identical. Electronic energy loss can stem from excitation or ionization of target atoms or of the projectile itself, excitation of target electrons, or direct kinetic energy transfers to the target electrons through electron-electron collisions. In this sense, therefore, all electronic energy loss is not inelastic [81].

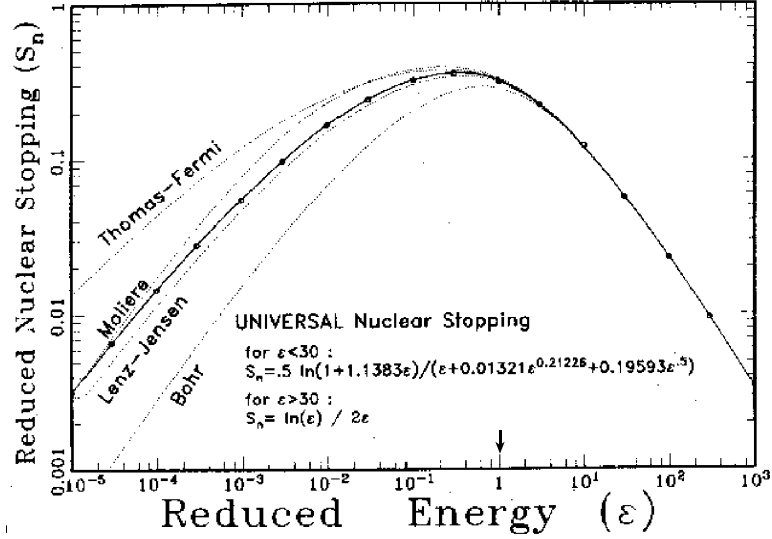


Figure 3.3: A comparison of stopping cross-sections in Thomas-Fermi coordinates for different interatomic potentials. The solid line is a fit to the *universal* (ZBL) reduced stopping power plotted as small circles. (From Ref. [81], courtesy of Pergamon Press.)

tion.  $S_n(E)$  is plotted in Thomas-Fermi variables for different screening functions in Fig. 3.3. The curve labelled “Thomas-Fermi” is known to be too high, while the curve labelled “Lenz-Jensen” slightly underestimates the stopping cross-section [82]. Equations 3.10 and 3.11 are based on the former, and are expected to be accurate within a few percents in accuracy for weak screening, *i.e.*, high energy ( $\epsilon \gg 1$ ,  $m \approx 1$ ) but within “at best a factor of 2” for heavy screening, *i.e.*, low energy ( $\epsilon \ll 1$ ,  $m \approx 0$ ) [82]. In the case of the power approximation of the Thomas-Fermi cross-section [88], the nuclear (elastic) stopping power takes the form

$$S_n(E) = \frac{1}{1-m} C_m \gamma^{1-m} E^{1-2m} \quad (3.16)$$

This is the form used in Sigmund’s theory of sputtering, which we will briefly describe later.

### 3.3 Sputtering Threshold and Surface Binding Energy

The existence of a sputtering *threshold* energy, below which “no” sputtering occurs, is in itself debatable. Indeed, the sputtering yield  $Y$  was defined as a statistical quantity expressing the expected number of atoms removed per incident ion, and trying to define a threshold energy is akin to trying to determine below which ion energy the probability of sputtering an atom from the surface is zero. Supposing that we start with a solid sample at 0 K and begin raising the temperature, surface defects will appear and a finite statistical probability will exist that a surface atom can acquire sufficient energy to leave the surface [94]. In other words, the effective surface binding energy for all atoms on a real surface has a distribution with a low-energy tail that extends to extremely small values. Rigorously speaking, therefore, the surface has a finite vapor pressure and the notion of sputtering threshold is illegitimate.

From a practical standpoint, however, it can be useful to define a sputtering threshold as the kinetic energy for the incident ions below which no *observable* sputtering occurs. At energies well above the surface binding energy, in the linear cascade regime, the sputtering yield  $Y$  is proportional to the energy deposited in the top monolayers by nuclear collisions. As the energy is decreased toward and near the average surface binding energy, however,  $Y$  is seen to decrease dramatically (on a logarithmic scale) with decreasing energy. The energy is then said to be in the vicinity of the sputtering “threshold.” This, however, inevitably turns the notion of sputtering threshold energy into a relative one, and, as a consequence, the literature abounds with a great variety of experimental measurements and definitions of sputtering thresholds.

As we will see shortly, most analytical formulae that describe the energy-dependence

of the sputtering yield require a sputtering threshold as input. For a first-level approximation, and using again the hard-sphere, binary collision model—the billiard-game analogy—it can be seen from Eq. 3.2 that the energy retained by the projectile in a purely reflective, *i.e.*,  $\Theta = \pi$  and  $T = \gamma E$  (a possibility only if  $M_1 < M_2$ ) is  $(1 - \gamma)E$ . After a large number  $k$  of small angle collisions with scattering angle  $\Theta_{small}$ , however, the energy retained by the primary projectile, assuming a monoatomic target, is given by

$$E_k = \left[ 1 - \gamma \sin^2 \left( \frac{\Theta_{small}}{2} \right) \right]^k E \quad (3.17)$$

If we write that  $k\Theta_{small} \approx \pi$  so that the momentum of the projectile is turned outwards in order to sputter a surface atom—mechanism 3 in Fig. 3.2—then  $E_k$  becomes

$$E_k \approx \left( 1 - \frac{\gamma\pi^2}{4k} \right) E \quad (3.18)$$

Thus, ions may be reflected with negligible energy loss and can knock out surface atoms if the maximum transferable energy is greater than the surface binding energy  $U_b$ , *i.e.*, if

$$\gamma E \geq U_b \quad (3.19)$$

In most cases,  $U_b$  is assumed identical to the atomic heat of sublimation,  $U_s$  [95–100].

It is also often found to be related to the lattice displacement energy by  $U_b \approx U_d/4$ . Therefore, a simple definition of sputtering threshold can be given by

$$E_{th} = \frac{U_b}{\gamma} \quad (3.20)$$

For xenon on molybdenum, this definition would result in a value of 7 eV for  $E_{th}$  with a surface binding energy for molybdenum of 6.83 eV [73]. This is a *lower* bound for the threshold energy—under the assumptions of the hard-sphere model—at normal ion incidence and is in fact expected to be too low for heavy ions since mechanisms

$S_{II}$  in Fig. 3.2 are less likely for  $M_1 > M_2$ . We note that lower threshold values can be expected at oblique incidences [86, 98].

The definition for  $E_{th}$  in Eq. 3.20 was first proposed by Bradley in 1954 [101] and was later modified by Wehner [102] who suggested that  $E_{th}$  was proportional to  $U_s/\gamma$  by a factor of 8–20. It was also experimentally observed [103, 104], however, that the “thresholds” seemed to differ very little for different ions but more for different target materials. The mass ratio of the collision partners, in other words, did not seem to be of any importance, and this was attributed to the fact that the collision times were long enough that several neighboring atoms could come into play before the primary collision was over [72]. The fractional energy transfer  $\gamma$  therefore dropped from some models used to predict the sputtering threshold and the approximations  $E_{th} \approx 4U_s$  [72, 104] or  $E_{th} \approx U_s$  [105] were suggested. Other experimental results by Askerov and Sena in 1969 [106], however, pointed again to a strong dependence of  $E_{th}$  on the ratio  $U_s/\gamma$  and this approximation was subsequently mentioned by other authors [99, 107, 108]. Although the sputtering threshold remains controversial to date, its strong correlation with the surface binding energy and the projectile-to-target mass ratio is now well established but has not been linked to any particular material properties.<sup>2</sup>

More recently several authors have proposed analytical expressions for the relative threshold energy  $E_{th}/U_s$  as a function of the mass ratio  $M_1/M_2$  based on fits of experimental and/or calculated data as well as theoretical arguments. A review of such expressions is given in Ref. [86]. The most commonly used are the one proposed

---

<sup>2</sup>A  $Z_2$ -dependence has been observed, however, and Askerov and Sena did suggest in Ref. [106] that within a given period for the target element the sputtering threshold energy “decreases according to the filling of the atomic  $d$  shell.”

by Bohdansky [96]

$$E_{th} = \begin{cases} \frac{U_b}{\gamma(1-\gamma)} & \text{for } M_1/M_2 \leq 0.3, \\ 8U_b(M_1/M_2)^{2/5} & \text{for } M_1/M_2 > 0.3. \end{cases} \quad (3.21)$$

and the expression proposed in Ref. [109] in the so-called “third Matsunami formula”

$$E_{th} = U_s \left[ 1.9 + \left( \frac{M_1}{M_2} \right) + 0.134 \left( \frac{M_1}{M_2} \right)^{-1.247} \right] \quad (3.22)$$

Finally and in light of the most recent experimental data, Yamamura and Tawara [100] proposed the following universal relations

$$\frac{E_{th}}{U_s} = \begin{cases} \frac{6.7}{\gamma} & \text{for } M_1 \geq M_2, \\ \frac{1+5.7(M_1/M_2)}{\gamma} & \text{for } M_1 \leq M_2. \end{cases} \quad (3.23)$$

and Manteniaks [110] derived from existing experimental data the following relationship for mercury and xenon ions

$$E_{th} = U_s \left[ 4.4 - 1.3 \log \left( \frac{M_2}{M_1} \right) \right] \quad (3.24)$$

In all, a total of ten different expressions are available for any given mass ratio in order to estimate the relative threshold energy at normal ion incidence, based on different theories or experimental data. The existing experimental values and the range of “threshold” energies predicted by the available analytical formulations are summarized in Table 3.2. The lower limit from Eq. 3.20 was only taken into account for tantalum and tungsten in this table, since it is expected to be unreasonably low for relatively heavy ion bombardment.

Clearly, sputtering thresholds are very poorly defined. The coarse models and fits used in Table 3.2 do not account for any particular structure of the target, *e.g.*, no difference is seen for carbon between graphite and diamond, because although the lattice displacement energies  $U_d$  differ, the surface binding energy  $U_b$  is identical [73].

Target element	C	Ti	Mo	Ta	W
$M_2$ [amu]	12.0	47.9	95.9	180.9	183.9
$U_b$ [eV]	7.41	4.89	6.83	8.10	8.68
Experimental data	$\gtrsim 100$ (a)	18 (b)	27 (b), 48 (c)	30 (b)	30 (b), 57 (c)
Analytical range	30–353	20–78	27–64	8–66	9–61

Table 3.2: Experimental and analytical values of the sputtering threshold energy (eV) for xenon ions and different target elements. Experimental values from (a) Ref. [111]; (b) Ref. [104]; and (c) Ref. [96], where the thresholds were obtained indirectly from an argument on similarities. Target elements data from Table 6.1 in Ref. [73].

A theory for the sputtering thresholds of crystalline targets was however proposed in 1961 by Harrison and Magnuson [94].

As a final comment, it should be noted that  $E_{th}$  is always related to the surface binding energy  $U_b$ , which itself is often considered to be equal to the sublimation energy  $U_s$ . This, however, is not physically justified since sputtering, an atom-by-atom collisional process, is fundamentally different from sublimation, a thermal process. Indeed, Olson *et al.* [85] pointed out that “sputtering thresholds” may in fact have an effective value much less than the heat of sublimation.

In summary, while it is debatable that there is a “sputtering threshold energy” on a real surface, it is of interest to evaluate what the threshold energy might be on an ideal surface. Below this theoretical energy one might expect that sputtering yields would reach negligible values for practical applications. In addition, the value for the theoretical threshold energy is an important parameter in almost all of the existing analytical models for the energy dependence of sputtering. Which approximation is to be used depends on which sputtering mechanism dominates (Fig. 3.2). The important distinction is that sputtering by light ions is primarily driven by backscattering of the ions from the interior of the target (reflective collision process,  $S_{II}$ ), whereas for heavy ions collision cascades generated by direct impingement of the incoming ions

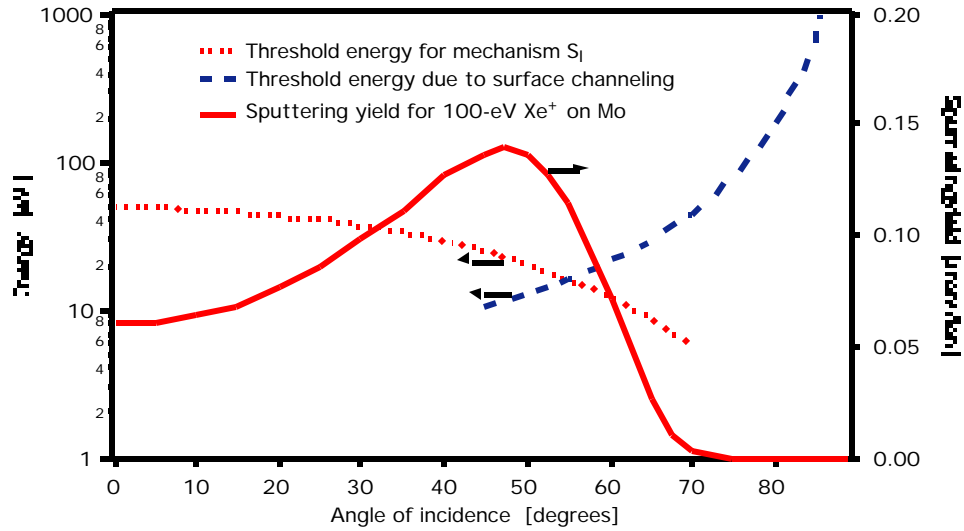


Figure 3.4: Sputtering threshold energy and yield as a function of ion angle of incidence for xenon on molybdenum.

dominate the sputtering mechanism (displacement process,  $S_I$ ). This distinction is an extremely important driver for the threshold energy, as well as for the angular dependence of the low-energy sputtering yield [98].

As an example, we have used the models in Ref. [98] for the effect of angle of incidence on sputtering threshold and yield depending on which mechanism dominates (Fig. 3.2) to plot the threshold energy for xenon ions on molybdenum as a function of angle of incidence. For heavy ions and at not-too-oblique angles mechanism  $S_I$  dominates and the threshold energy is a decreasing function of the angle of incidence, while for grazing incidences surface channeling comes into play (Fig. 3.4). Surface channeling is due to the fact that the probability for the incoming ion to penetrate the first layer of the solid surface and sputter surface atoms starts to decrease significantly at grazing incidence angles because of surface scattering.

## 3.4 Summary

Sputtering is an atom-by-atom collisional process that occurs in three distinct regimes: single knock-on, where the atoms sputtered are essentially PKAs, up to a few hundred eV; linear cascades, where SKAs and higher-generation recoil atoms are produced, at keV energies; and spike, where the spatial density of moving atoms is large [82], at tens of keV or higher. Sputtering can be best characterized by the relevant cross-sections for the energy transferred in the single knock-on regime, and by the energy deposited per unit depth—defined by the stopping power for the ion-target combination—in the linear cascade regime.

At high energies, the interaction can be treated as pure repulsion between nuclear charges, while at low energy the nuclear charges are partially screened by the electron clouds. The stopping power is comprised of a nuclear (elastic) and an electronic (mostly inelastic) component. Nuclear stopping can be described as a pure Coulombic interaction between the nuclei, superimposed with an electronic screening effect, while electronic stopping is mostly a function of the electron distribution assumed around the collision partners and can be considered proportional to the projectile velocity. Because there is little penetration of the electron clouds for slow particles, the electronic energy loss can be considered very small at energies near threshold.

At very high energies, in the spike regime, sputtering is highly non-linear and can be described by a shock-wave model or by considerations on heat conduction in the spike region. For linear cascades, or at very low energies in the single knock-on regime, an analytical treatment of sputtering requires the choice of an atomic model, whose corresponding potential and screening function serve as inputs to the calculation of the individual collisions or collision cascades. In addition, a number of physical inputs are also required, including the surface binding energy and roughness, the lattice

displacement and binding energy, the target atomic density and bulk morphology, and of course the ion kinetic energy and angle of incidence.

At extremely low energies, however, in the region near threshold (a few eV up to about a hundred eV), a number of assumptions in the theory of sputtering break down: the “effective size” of the target atoms becomes large enough that the projectile interacts with more than one atom at the same time, *i.e.*, the assumption of independent binary collisions becomes dangerously questionable; the linear cascade theory is not valid because the sputtered atoms are essentially PKAs; and the stopping powers obtained using the different classical atomic descriptions start to differ greatly at low energy ( $\epsilon \lesssim 1$ ).

# Chapter 4

## Analytical and Computational Treatment of Sputtering

In this chapter we start by proposing a model to estimate the sputtering threshold energy while taking into account inelastic energy losses for ions or atoms reflected in the near-surface layer of a random (amorphous) solid, under the binary collision approximation. We then review practical semi-empirical formulations applicable for slow, heavy ions, and we implement a three-body collision model to predict near-threshold sputtering yields for xenon on molybdenum. Finally, we present results of Monte-Carlo simulations of sputtering using the program TRIM.

### 4.1 Threshold Energy Model with Inelastic Losses

As mentioned earlier, electronic energy losses in projectile-target collisions are expected to be small at low projectile velocities because the overlap between the colliding particles electron distributions is very limited. At energies in the threshold region, however, we showed in Eq. 3.18 that the most favorable mechanism for sput-

tering under the binary collision approximation involves a large number of small-angle scattering interactions below the target surface, in order to minimize elastic energy losses, which are proportional to  $E^{1-2m}$ . This, in turn, suggests that electronic energy loss—which is proportional to velocity, or  $E^{1/2}$ —might not be negligible when integrated over a large number of collisions. In fact, electronic stopping would be expected to dominate nuclear stopping at low energy, if  $m < 1/4$ . We describe below a model that accounts for inelastic losses. This model is similar to that proposed by Eckstein *et al.* [86] but here we let the collision be specified by the incident particle energy and the unique scattering angle in barycentric coordinates,  $\Theta$ , related to the scattering angle in the laboratory frame of reference,  $\theta$ , by

$$\sin(\Theta - \theta) = \frac{M_1}{M_2} \sin \theta \quad (4.1)$$

All small-angle collisions have the same scattering angle for a minimum energy loss process [112], but in this model we force the collision that generates the PKA to be a maximum energy transfer collision, so that  $\Theta = \pi$  for that interaction. Therefore we have  $k$  scattering interactions and one zero-scattering collision. If we consider the general case of an incidence angle  $\vartheta$  and emission angle of the sputtered atom  $\beta$ , we have the conditions  $0 \leq \vartheta, \beta \leq \pi/2$  and

$$\theta = \frac{1}{k}(\pi - \vartheta - \beta) \quad (4.2)$$

Finally, we introduce the inelastic energy loss  $\Delta E$  incurred along the particle path. As suggested by Eckstein, we consider the inelastic energy loss to be proportional to the target atomic number density  $N$  and the mean free path  $l = N^{-1/3}$ , so that

$$\Delta E = N^{2/3} S_e \quad (4.3)$$

where  $S_e$  is the electronic stopping power. We use the expression for  $S_e$  given by Lindhard and Scharff [113]:

$$S_e(E) = 1.21 \frac{Z_1^{7/6} Z_2}{(Z_1^{2/3} + Z_2^{2/3})^{3/2}} \sqrt{\frac{E}{M_1}} \quad (4.4)$$

$S_e(E)$  is in units of  $\text{eV} \cdot \text{\AA}^2$ ,  $E$  is in eV and  $M_1$  in amu. We assume in the following that the change in particle energy over the collision path is small enough that the inelastic stopping is constant over the energy range considered. We will evaluate  $S_e$  at an energy close to threshold, *i.e.*,  $E \approx 30$  eV for molybdenum.

We now start by first considering the case of sputtering under mechanism 3 in Fig. 3.2. This is the preferred mechanism—the one that should result in the lowest threshold energy—for light-ion sputtering. In this mechanism, the primary projectile with initial energy  $E$  undergoes  $k$  collisions to rotate its momentum outwards before finally sputtering a PKA in a head-on (maximum energy transfer) collision. After the first collision the projectile energy  $E_1$  is given by Eq. 3.2, *i.e.*,

$$E_1 = E \left( 1 - \gamma \sin^2 \frac{\Theta}{2} \right)$$

As in Eq. 3.17, we write the energy retained by the primary projectile after a number  $k$  of small-angle collisions, but this time taking into account an inelastic (electronic) component in the energy loss. After the second collision, the projectile energy  $E_2$  is now given by

$$E_2 = (E_1 - \Delta E) \left( 1 - \gamma \sin^2 \frac{\Theta}{2} \right) \quad (4.5)$$

and after  $k$  collisions it can be written as

$$E_k = E \left( 1 - \gamma \sin^2 \frac{\Theta}{2} \right)^k - \Delta E \sum_{i=1}^{k-1} \left( 1 - \gamma \sin^2 \frac{\Theta}{2} \right)^i \quad (4.6)$$

To write the condition for sputtering we use the common assumption of a planar

surface potential [82, 95, 114] described by

$$P(E, \beta) = \begin{cases} 1 & \text{for } E \cos^2 \beta \geq U_b, \\ 0 & \text{for } E \cos^2 \beta < U_b. \end{cases} \quad (4.7)$$

where  $P(E, \beta)$  is the emission probability for the recoil atom with energy  $E$  and emission angle  $\beta$  at the surface. We note that this surface potential model implies that sputtered atoms can experience refraction on leaving the surface [73]. In this model,  $\beta$  is the emission angle *before* refraction. The threshold condition for sputtering after  $k$  small-angle collisions is therefore given by

$$\gamma(E_k - \Delta E) \cos^2 \beta = U_b \quad (4.8)$$

so that the sputtering threshold energy with an inelastic loss term for reflected (preferably light) ions is obtained as

$$E_{th} = \frac{U_b + \gamma \Delta E \cos^2 \beta \sum_{i=0}^{k-1} \left(1 - \gamma \sin^2 \frac{\Theta}{2}\right)^i}{\gamma \cos^2 \beta \left(1 - \gamma \sin^2 \frac{\Theta}{2}\right)^k} \quad (4.9)$$

In this equation,  $\Theta$  is determined by Eqs. 4.1 and 4.2. We note that a minimum total of two collisions is necessary, *i.e.*,  $k \geq 1$ : this excludes mechanism 1' in Fig. 3.2, which does not involve inelastic stopping, from this simulation.

We now turn to sputtering under mechanism 1 in Fig. 3.2, which is the dominant—*i.e.*, most probable—sputtering mechanism for relatively heavy ions ( $M_1 > M_2$ ). Again, we consider the emission of a primary recoil atom produced by a maximum energy transfer collision, this time in the first ion-atom collision. All subsequent  $k$  scattering events are small-angle interactions between the PKA and other target atoms, so that  $\gamma = 1$  and  $\Theta = 2\theta$  for a monoatomic solid. In a similar fashion, we obtain the following expression for the sputtering threshold energy for the mechanism

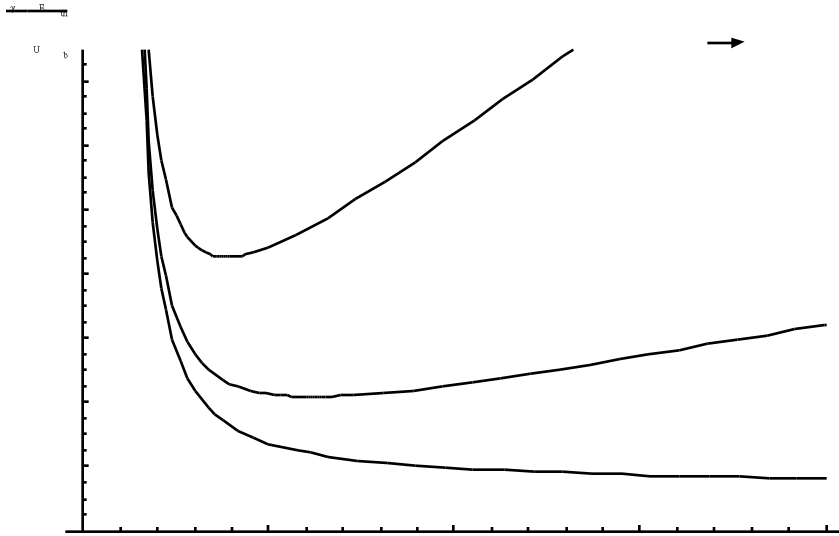


Figure 4.1: Relative sputtering threshold versus number of collisions for xenon ions on molybdenum, assuming no inelastic energy losses; a quarter, and a full Lindhard-Scharff inelastic stopping power.

avored by heavy ions:

$$E_{th} = \frac{U_b + \Delta E \cos^2 \beta \sum_{i=1}^k \left(1 - \sin^2 \frac{\vartheta}{2}\right)^i}{\gamma \cos^2 \beta \left(1 - \sin^2 \frac{\vartheta}{2}\right)^k} \quad (4.10)$$

We emphasize that both Eqs. 4.9 and 4.10 can be used regardless of the mass ratio  $M_1/M_2$  because both mechanisms are generally present in actual sputtering, but Eq. 4.9 will yield the *lowest* threshold for light ion sputtering while Eq. 4.10 will yield the lowest threshold for heavy ion sputtering. We note, however, that Eq. 3.5 forces the additional constraint on the number of collisions

$$k \geq \frac{\pi - \vartheta - \beta}{\arcsin\left(\frac{M_2}{M_1}\right)} \quad (4.11)$$

if the threshold for mechanism 3, *i.e.*, using Eq. 4.9, is sought for heavy ions.

Figure 4.1 shows the results of the model described by Eq. 4.10 for the case of xenon ion bombardment of molybdenum at normal incidence. In this figure we have

Target element	$C_{graphite}$	$C_{diamond}$	Ti	Mo	Ta	W	
$M_2$ [amu]	12.0	12.0	47.9	95.9	180.9	183.9	
$\hat{\beta}$ [deg.]	17	30	35	32	18	18	
$E_{th}$ [eV]	LS	159	183	44	60	63	68
	1/4 LS	77	92	24	28	29	31

Table 4.1: Sputtering threshold values for xenon ion bombardment on different target materials, assuming a quarter and a full Lindhard-Scharff inelastic stopping power.  $\hat{\beta}$  is the sputtered atom emission angle for lowest threshold.

normalized the threshold energy  $E_{th}$  by the ratio  $U_b/\gamma$ , *i.e.*, the lower bound for sputtering thresholds established by Eq. 3.20. The emission angle  $\beta = 32^\circ$  was found to minimize the returned threshold value, which is also a decreasing function of angle of incidence  $\vartheta$ . As expected, the relative threshold decreases monotonically towards one for increasingly large numbers  $k$  of projectile scattering interactions if no inelastic losses are taken into account. A minimum is reached for a finite number of collisions, however, if the assumption of elastic collisions is dropped. The case where we apply a stopping power equivalent to a quarter of the Lindhard-Scharff model, as suggested by Eckstein [86], seems to yield values relatively close to the little existing experimental data shown in Table 3.2. The results are summarized in Table 4.1 for comparison.

Figure 4.2 shows a comparison of results for six different target materials using the quarter Lindhard-Scharff model, for normally-incident ions and for a sputtered atom emission angle of  $30^\circ$ . The curves relative to tantalum and tungsten were generated using Eq. 4.9—corresponding to the sputtering mechanism 3 in Fig. 3.2—while the other curves use Eq. 4.10—sputtering mechanism 1. It can be seen that the more efficient reflection of relatively light ions results in a smaller number of collisions necessary to turn the particle momentum back toward the exterior of the target. The rather significant difference between graphite and diamond stems from the different

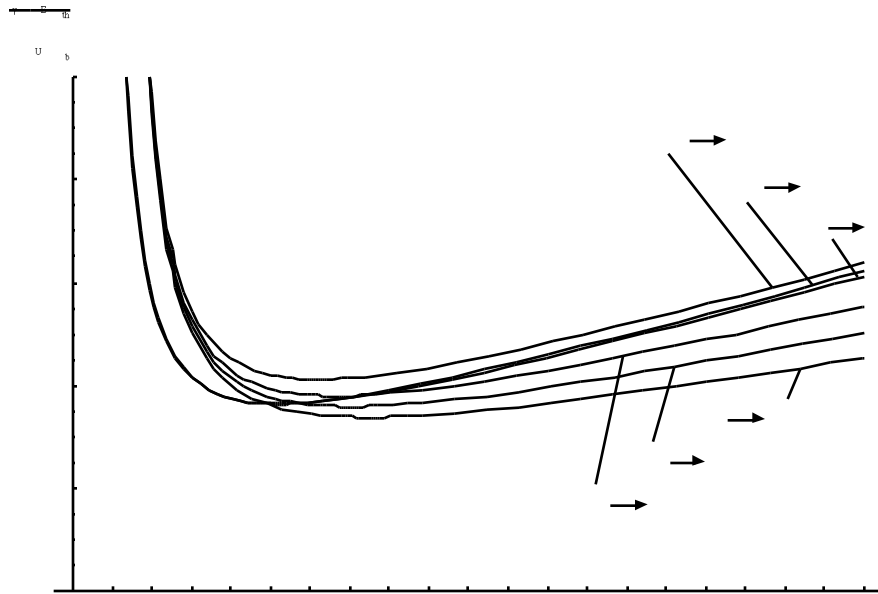


Figure 4.2: Relative sputtering threshold at normal incidence versus number of collisions for xenon ions on different target materials, using a quarter Lindhard-Scharff inelastic stopping power.

atomic number densities.

In conclusion, while this particular model has the merit of considering inelastic losses and provides a beginning of explanation for experimentally observed, higher-than-expected thresholds, it remains very dependent on the expression of the electronic stopping power, which is also “subject to considerable doubt at these low energies” [115]. We must also recall that the validity of the binary collision approximation at energies near threshold is questionable.

## 4.2 Analytical Formulae for the Energy Dependence of Sputtering yields

### 4.2.1 The Sigmund Theory

The most authoritative theoretical study of sputtering was done in 1969 by Sigmund [95]. In this theoretical study, an integrodifferential equation was developed for the sputtering yield, based on an approximation to the solution of the linearized Boltzmann transport equation.

Sigmund based his theory on the fundamental assumptions that the (monoatomic) target medium be isotropic and homogeneous, so that the transport of particles can be described by Boltzmann's equation, and on an isotropic distribution of the particle velocities. The medium is assumed to be semi-infinite, with a planar surface. Along the way, Sigmund uses the additional assumption that the collisions are binary so that he may use either the power approximation of the Thomas-Fermi scattering model (Eq. 3.10), or a Born-Mayer interaction potential of the form

$$V(r) = A_{BM} \exp\left(-\frac{r}{a_{BM}}\right) \quad (4.12)$$

in order to obtain adequate expressions for the cross-sections. In the Born-Mayer potential,  $A_{BM}$  is a constant, and  $a_{BM}$  is the screening radius, for which Sigmund proposes the value  $a_{BM} = 0.219 \text{ \AA}$ . Finally, Sigmund uses the last key assumption that the energy is well above the effective surface-barrier energy ( $E > 100\text{--}200 \text{ eV}$ ) in order to reconstruct an analytical solution from the moment equations. His main conclusion is that sputtering is proportional to the energy deposited near the surface by the incoming ion, so that his formula for backward sputtering is of the general

form

$$Y(E) = \Lambda F_D(E) \quad (4.13)$$

where  $F_D(E)$  is the density of deposited energy at the surface in units of eV/Å, given by

$$F_D(E) = \alpha N S_n(E) \quad (4.14)$$

Here  $\alpha$  is a dimensionless, energy-independent function of the mass ratio  $M_2/M_1$ , given in Ref. [95] for different approximations to the distribution function of the deposited energy.  $S_n$  is the nuclear stopping cross-section, in units of eV·Å<sup>2</sup>. The material factor  $\Lambda$  is a property of the target, and it has the form

$$\Lambda = \frac{3}{4\pi^2 C_0} \cdot \frac{1}{NU_b} \approx \frac{0.042}{\text{Å}^2} \cdot \frac{1}{NU_b} \quad (4.15)$$

where we have used  $\lambda_0 = 24$  and the screening radius  $a_{BM}$  in Eq. 3.11 for the numerical approximation of  $C_0$ .  $S_n$  can be described by a universal formula with the use of Linhard's reduced energy unit  $\epsilon$  and a *reduced* nuclear stopping cross-section  $s_n(\epsilon)$  for Thomas-Fermi interaction [88]

$$S_n(E) = 4\pi a_I Z_1 Z_2 e^2 \frac{M_1}{M_1 + M_2} s_n(\epsilon) \quad (4.16)$$

In this equation,  $a_I$  is the screening radius defined in Eq. 3.7, and  $\epsilon$  was defined in Eq. 3.6. The dimensionless nuclear stopping power  $s_n(\epsilon)$  is tabulated in Ref. [95] and can also be written, using Eqs. 3.6 and 3.16 with the power approximation, as

$$s_n(\epsilon) = \frac{\lambda_m}{2(1-m)} \epsilon^{1-2m} \quad (4.17)$$

We finally note that in the special case of energies smaller than 1 keV, Sigmund's formula (given by Eq. 4.13) reduces to

$$Y(E) \approx \frac{3}{4\pi^2} \alpha \frac{\gamma E}{U_b} \quad (4.18)$$

when the appropriate (low-energy) expression is used to calculate  $S_n(E)$  from Eq. 3.16, *i.e.*,  $m \approx 0$ .

We mention that Thompson [116] also proposed in 1968 a model for sputtering, based on the analysis of the energy spectrum of atoms sputtered by high-energy heavy ions in random collision cascades. His formula for sputtering at normal incidence,

$$Y = \frac{\pi^2 a_0^2 N^{2/3}}{8 e} \cdot \frac{E_R}{U_b} \cdot \frac{M_1(Z_1 Z_2)^{5/6}}{M_1 + M_2} \quad (4.19)$$

where  $E_R = 13.6$  eV is the Rydberg energy, does not contain the kinetic energy  $E$  of the incident ion. It is valid in the regime where sputtering can be considered energy-independent, in the tens of keV range.

To date, Sigmund's theory of sputtering remains the basis for most attempts to model the energy dependence of sputtering yields with universal analytical formulae. There are no fundamental assumptions in the Sigmund theory that are clearly violated at energies even as low as a few hundreds of eV. At energies near threshold, however, the binary collision approximation may break down, and we recall that the analytical solution to the Boltzmann equation proposed by Sigmund requires  $E \gg U_b$ . Beyond these fundamental assumptions, a number of other assumptions or approximations involved need particular attention at very low energy, *e.g.*, the velocity distribution of recoils may not be considered isotropic any longer, and the Thomas-Fermi interaction potential is believed to introduce a systematic error at low energies [115]. Equation 3.10 may yet remain a reasonable approximation in the eV region if  $m$  is taken close to zero [95]. A Born-Mayer potential ( $m \approx 0.055$ ) may also be appropriate [95]. Finally, the question of what constitutes an exact value for the surface binding energy remains a weak point, along with the determination of  $\alpha$ , which essentially converts stopping power into energy deposited in the target atoms in the surface region [117].

## 4.2.2 Semi-Empirical Formulae

A thorough review of the literature on analytical treatments of the sputtering yield [75, 96, 97, 109, 114, 117–130] reveals that, beyond Thompson’s and Sigmund’s fundamental theories, over seventeen distinct analytical approaches are proposed. Among them, the two approaches described in Refs. [128–130] are specific to the high-energy (non-linear) spike sputtering regime and are not relevant to sputtering processes in ion engines. Briefly, the first approach [128, 129] is a hydrodynamical analysis based on a shock wave model to explain non-linear sputtering yields in heavy-ion bombardments on high-Z materials, while the second [130]—the heated zone model—proposes to use a solution of the heat conduction equation to calculate the sputtering yield from the radial distribution of temperature in a cylindrical spike. Of all the other approaches, only two are not based on the Sigmund theory [75, 118]. We mention only the four most relevant below.

Two groups, one at the Max Planck Institut für Plasmaphysik in Garching, Germany, and the other at the National Institute for Fusion Science in Nagoya, Japan, have proposed a *semi-empirical* relation for the energy dependence of the sputtering yield. Both groups, encouraged by the similarities in the curves for sputtering yield versus energy for a wide range of ion-target combinations, and in an effort to establish a universal relation, have based their respective formula on the general equation derived by Sigmund (Eq. 4.13), to which they added empirical parameters or dependences to better fit the published experimental data. The initial formulae, in Refs. [119] and [121] respectively, have been successively modified, particularly in the early eighties, in a parallel effort to include threshold and electronic stopping effects, and to keep the fit parameters updated as additional experimental data became available (Refs. [114, 119, 120] and [97, 100, 109, 122, 123] respectively). The latest revisions

of these relationships, respectively given in 1993 [120] and in 1996 [100] and called respectively the Bohdansky formula and the third Matsunami formula, are given by

$$Y(E) = 0.042 \left( \frac{R_p}{R_a} \right) \frac{\alpha S_n(E)}{U_b} \left[ 1 - \left( \frac{E_{th}}{E} \right)^{\frac{2}{3}} \right] \left[ 1 - \left( \frac{E_{th}}{E} \right) \right]^2 \quad (4.20)$$

and

$$Y(E) = 0.042 \frac{Q\alpha^*}{U_s} \cdot \frac{S_n(E)}{1 + \Gamma k_e \epsilon^{0.3}} \left[ 1 - \sqrt{\frac{E_{th}}{E}} \right]^s \quad (4.21)$$

where we recall that the numerical constant 0.042 has dimensions of  $\text{\AA}^{-2}$  (Eq. 4.15). In both equations, the sputtering threshold energy  $E_{th}$  is considered a fit parameter, along with the quantities  $Q$  and  $s$ . The functions  $\alpha$ ,  $\alpha^*$ , and  $\Gamma$  are analytical functions of atomic masses, and are also based on curve fits. The quantity  $k_e$  is the (dimensionless) Lindhard electronic stopping coefficient [113]. The ratio  $R_p/R_a$  of the projected to average ion path lengths in the Bohdansky formula is a correction factor that is significant only for light ion sputtering, and is given as a function of the ion to target atom mass ratio. Finally, the two equations use a different analytical form for  $s_n(\epsilon)$  in the expression of the nuclear stopping power  $S_n(E)$  in Eq. 4.16, as they are based on two different potentials [100]. The different values for the fit parameters and the necessary analytical expressions for any given ion-atom combination are given in the corresponding references.

The differences between the two formulae essentially come from a different treatment of the electronic energy loss: implicitly, through the fit parameters in the Bohdansky formula, and explicitly through an energy dependence in the Matsunami formula. The correction factor  $R_p/R_a$ , important for high-energy light ions, has an equivalent through a different expression for  $\alpha^*$  for heavy or light ion sputtering in the Matsunami formula. The slightly different exponents for the energy-dependent terms in the two equations are mainly due to a small difference in the value chosen for

$m$  in the power potential approximation (Eqs. 3.10 and 3.16), 1/3 for the Bohdanský formula, and 0.4 for the third Matsunami formula. Essentially, the two equations can be expected to perhaps differ significantly for high-energy, light ions, where electronic stopping plays a larger role, but in the situation of interest here—low-energy, heavy ions—they are expected to yield very similar results.

Shulga [127] very recently established a formula based on Sigmund’s result for low-energy (<1 keV) sputtering that he revisited to include an explicit dependence on the target atomic number density  $N$ . In this study, Shulga decoupled the density dependence from the target element dependence, and obtained an equation that takes the form

$$Y(E) = A_s \frac{N^{p_s}}{U_b^{q_s}} Y_s(E) U_b \quad (4.22)$$

where  $Y_s$  is used here to denote Sigmund’s low energy sputtering yield defined in Eq. 4.18. The quantities  $A_s$ ,  $p_s$  and  $q_s$  are fit parameters, obtained for xenon with a fit of the sputtering data on thirty different target materials from Refs. [111, 131]. They have values 4.51, 0.539, and 1.296, respectively, for 200 eV xenon ions. The relative error reported by Shulga on this fit is 37.7%.

Wilhelm [75] published in 1985 the only *physical* model, to the author’s knowledge, that does not rest on the binary collision approximation and is specific to low-energy sputtering in the near threshold region. Wilhelm’s approach is a quantum-statistical analysis of a three-body surface sputtering mechanism involving the incoming ion and two target atoms, and results in the approximate form

$$Y(E) \approx \frac{1}{24} h_{2/1} \sigma(E_{th}) N^{2/3} \left( \frac{(M_2/M_1)^2}{1 + 2M_2/M_1} \right)^{3/2} \frac{(E - E_{th})^2}{E_{th}^2} \mathcal{H}(E - E_{th}) \quad (4.23)$$

In this equation,  $h_{2/1}$  is a dimensionless coefficient resulting from the quantum statistical treatment of the interactions that can in principle be evaluated, although un-

fortunately this is rather difficult practically. The quantity  $\sigma(E)$  is the total (energy-dependent) cross-section for elastic ion-atom scattering, and  $\mathcal{H}$  is the Heaviside step function.

Although this relationship may seem extremely promising, Wilhelm pointed out that the theoretical values for  $h_{2/1}$  and the total cross-section  $\sigma(E)$  are very difficult to obtain, and the suggestion was to use experimental data to estimate the cross-sections. One seems to be left, therefore, with merely using the  $(E - E_{th})^2$  dependence of the sputtering yield—an already extremely valuable information indeed—and fitting this form to the available data, a solution that has been implemented before for xenon on molybdenum [53, 110]. This was done by Wilhelm for mercury ions using the data published by Askerov and Sena [106] below 100 eV, but unfortunately no such data exists for xenon. In addition, the theoretical curves for mercury using the lowest-energy points in the experimental data was found by Wilhelm to depart the experimental curves at energies as low as 30 eV above threshold, which suggests that his relationship is indeed limited to extremely low energies. Finally, experimental sputtering yield data obtained at near-threshold energies tend to be questionable due to the formation of surface impurity (*e.g.*, oxide) layers at the surface of the sample [117, 132].

### 4.2.3 Discussion

The Wilhelm theory contains three uncertain parameters: the sputtering threshold energy  $E_{th}$ , the total (energy dependent) cross-section for elastic ion-atom scattering  $\sigma(E)$ , and the dimensionless coefficient  $h_{2/1}$ . In the following, we propose an analytical evaluation of the Wilhelm expression (Eq. 4.23) without relying on a fit of higher-energy experimental data.

We first turn to the threshold energy. If the entire range of values proposed for the sputtering threshold of xenon on molybdenum (Table 3.2) is used, the variation in low-energy sputtering yield in the range 50–100 eV using the Wilhelm theory is found to be +18% to -100%. Some analytical values for the sputtering threshold, however, seem to be unreasonably high given the experimentally measured value of 27 eV [104], and we will consider here the uncertainty associated with a threshold in the range 27–48 eV.

In order to calculate the total elastic ion-atom scattering cross-section for xenon and molybdenum, the two potentials that can provide the best answers at very low energies are either a power approximation to the Thomas-Fermi potential with the exponent  $m$  taken close to zero, or a Born-Mayer potential [82, 95, 115]. We use the value  $E_{th} \approx 28$  eV, obtained using the model described earlier with a quarter Lindhard-Scharff electronic stopping power, which was close to the value observed in the experiments of Stuart and Wehner [104]. For  $m = 0$ , the total elastic scattering cross-section for xenon on molybdenum is found to be  $\sigma(E_{th}) \approx 1.24 \times 10^{-15} \text{cm}^2$ , if a cutoff energy transfer of 0.1% is chosen as the lower bound for the integration. In the case of the Born-Mayer potential, we use the *hard-core approximation* [133], where the potential  $V(r)$  is replaced by a hard sphere of radius  $R_0$  given by [82]

$$V(R_0) = \frac{M_2 E}{M_1 + M_2} \quad (4.24)$$

so that the radius of the hard sphere is energy-dependent. The potential  $V(r)$  is given by Eq. 4.12 where the constant  $A_{BM}$  is the *universal* expression proposed by Andersen and Sigmund [134]:

$$A_{BM} = 52 (Z_1 Z_2)^{3/4} \text{ eV} \quad (4.25)$$

Using a Born-Mayer potential decreased the low-energy sputtering yield by 36% com-

Energy (eV)	Sput. yield (atoms/ion)	Uncertainty (percent) due to	
		threshold	cross-section
100	$5.5 \times 10^{-2}$	$\begin{smallmatrix} +11 \\ -82 \end{smallmatrix}$	-36
90	$4.1 \times 10^{-2}$	$\begin{smallmatrix} +11 \\ -84 \end{smallmatrix}$	-36
80	$2.9 \times 10^{-2}$	$\begin{smallmatrix} +12 \\ -87 \end{smallmatrix}$	-36
70	$1.9 \times 10^{-2}$	$\begin{smallmatrix} +13 \\ -91 \end{smallmatrix}$	-36
60	$1.1 \times 10^{-2}$	$\begin{smallmatrix} +14 \\ -95 \end{smallmatrix}$	-36
50	$5.2 \times 10^{-3}$	$\begin{smallmatrix} +18 \\ -100 \end{smallmatrix}$	-36
40	$1.5 \times 10^{-3}$	$\begin{smallmatrix} +26 \\ -100 \end{smallmatrix}$	-36
30	$4.3 \times 10^{-5}$	$\begin{smallmatrix} +142 \\ -100 \end{smallmatrix}$	-36

Table 4.2: Quantitative uncertainties in the Wilhelm theory for xenon on molybdenum. The given baseline sputtering yields assume a threshold energy of 28 eV and a power potential approximation with  $m = 0$ .

pared to the Thomas-Fermi potential with  $m = 0$ .

Finally, the coefficient  $h_{2/1}$  contains matrix transition elements that result from Wilhelm’s quantum-statistical treatment of the interactions. This coefficient could be evaluated if the force potential of the three-body sputtering process, in particular, were known. This is unfortunately not the case, and the best that can be said is that  $h_{2/1}$  is of the order of 1 [75, 135].

Table 4.2 summarizes the uncertainties discussed above, and Fig. 4.3 shows a comparison of the four relevant analytical formulae described above, along with the low-energy Sigmund formula, for the sputtering yield of xenon on molybdenum. Added are the results of computations using the program TRIM, to be described in the following section.

Because Sigmund makes it clear in his theory that his formula is not expected to hold below 100–200 eV, we do not extend the corresponding curve to low energies. The same applies to the Shulga formula, which essentially proposes a correction to the

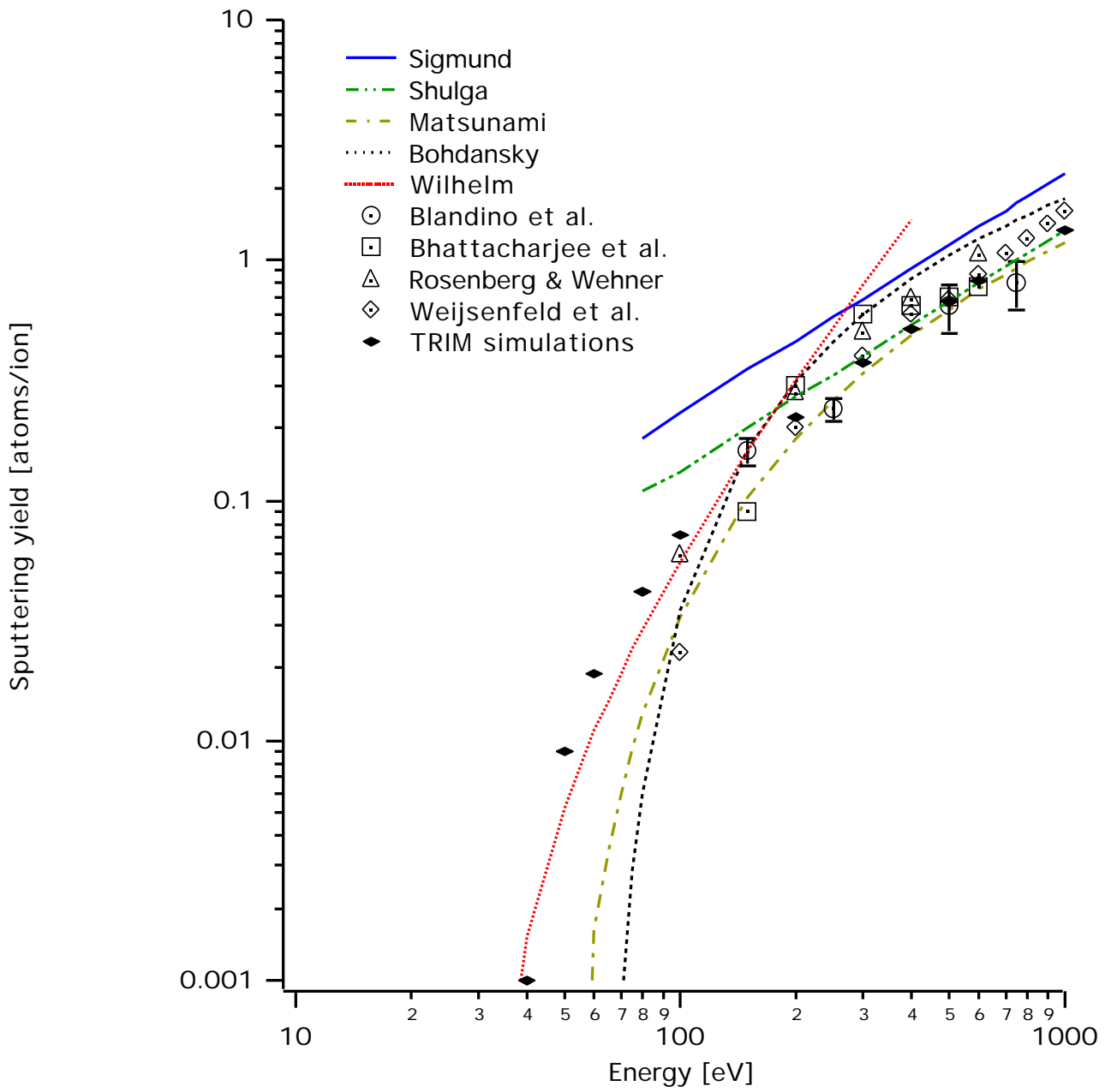


Figure 4.3: Analytical formulae, computer simulations, and previous experimental data for the energy dependence of the sputtering yield of molybdenum by xenon ions. The experimental data are from Weijnsfeld *et al.* [136], Rohsenberg and Wehner [111], Bhattacharjee *et al.* [137], and Blandino *et al.* [138].

Sigmund formula for the effect of atomic number density for a given target element. In the case of the Bohdansky and Matsunami formulae, we chose to extend their results to low energy, although both semi-empirical formulations are based on the Sigmund theory, because both authors have introduced “threshold effects”—forcing a threshold as a fit parameter—and have claimed that their results extend to sputtering in the threshold region. They did not, however, publish the uncertainties associated with the curve fits that form the basis of their expressions.

As a conclusion for this section, the Wilhelm theory was found to be the only one that has a sound physical justification below 100 eV. Unfortunately, the parameters needed for a complete evaluation retain a significant uncertainty, as expressed in Table 4.2.

## **4.3 Monte-Carlo Simulations Using TRIM 2000**

### **4.3.1 The TRIM Program**

TRIM (the TRansport of Ions in Matter) is a comprehensive program included in the scientific software package SRIM (the Stopping and Range of Ions in Matter). SRIM is based on the work by Ziegler and Biersack on stopping theory [81] and is freely distributed by IBM-Research [139].

In SRIM, all ion-atom collisions receive a quantum mechanical treatment, and the stopping and range of ions can be calculated in the energy range 10 eV–2 GeV. The calculations of the ion-atom screened Coulomb collisions use statistical algorithms to allow for jumps between calculated collisions before the collision results are averaged over the trajectory gap, and interactions between overlapping electron shells (electronic stopping) are included. TRIM accepts complex, multilayered and

multicomponent (including biological) targets. Solid or gas targets can be treated, although differently, and the ion angle of incidence with respect to surface normal can be specified. Using a ZBL potential, TRIM “will calculate both the final 3D distribution of the ions and also the kinetic phenomena associated with the ion’s energy loss: target damage, sputtering, ionization, and phonon production.” The initial version of TRIM was written in 1980, and the physics underlying TRIM are described in Ref. [81].

For the particular purpose of calculating surface sputtering with TRIM, three material input parameters are of importance: the surface binding, lattice displacement, and lattice binding energies, as defined at the beginning of Chapter 3. As will be discussed below, the sputtering yield can in particular be very sensitive to the surface binding energy. In the calculations on molybdenum presented in this section, the lattice displacement energy was chosen as 33 eV, which is both suggested by the TRIM table and is the value indicated in Table 6.1, Ref. [73]. The lattice binding energy, lost by the atoms as they leave their lattice site and assumed to go into phonons, was left at the value of 3 eV indicated in the TRIM table. Finally, a value of 3.9 eV was assumed for the effective surface binding energy, which corresponds to  $U_b/1.75$  where  $U_b$  is the value given by Ref. [73]. This “calibration” value was chosen so that the code results would match the experimental results obtained for xenon ions on molybdenum at 500 eV. Reasonable changes in either the lattice displacement energy or the lattice binding energy did not lead to significant changes in the sputtering yield in this energy range.

### 4.3.2 Results on the Energy Dependence of the Sputtering Yield

The calculated sputtering yield for energetic normally-incident xenon ions on molybdenum is shown in Fig. 4.3 as a function of ion kinetic energy. The agreement with the experimental data above 100 eV is good over the whole range shown, up to 1 keV. Indeed, this was expected, as Sigmund mentioned in 1987 [115] that “by and large, there is good agreement between Monte-Carlo and transport theoretical results.” Sigmund also notes that the main reason for the success of the TRIM code probably lies in the fact that the ion-atom potential used is “superior” to the combination of Thomas-Fermi and Born-Mayer potentials toward low energy (down to  $\approx 300$  eV). It is surprisingly close to the Wilhelm formula below 100 eV, however, despite the fact that TRIM uses binary collision dynamics.

Figure 4.4 shows distribution plots of the kinetic energy component normal to the surface for all displaced molybdenum atoms that reach the surface plane ( $x = 0$ ). Only those atoms that have a normal component of the kinetic energy greater than the surface binding energy are actually sputtered. The energy value indicated on the plot is the value that the atoms have upon reaching the surface. Actually sputtered atoms are considered to lose the equivalent of the surface binding energy *after* leaving the surface plane. A plot of the average kinetic energy of all sputtered atoms *after* leaving the surface is shown versus bombarding ion kinetic energy in Fig. 4.5, along with plots of the number of backscattered ions and vacancies created per ions. The fact that a finite number of ions are backscattered illustrates that, at high energies, mechanisms  $S_{II}$  (Fig. 3.2) can contribute to sputtering even for relatively heavy ions, albeit moderately. The energy dependence of the number of backscattered ions weak-

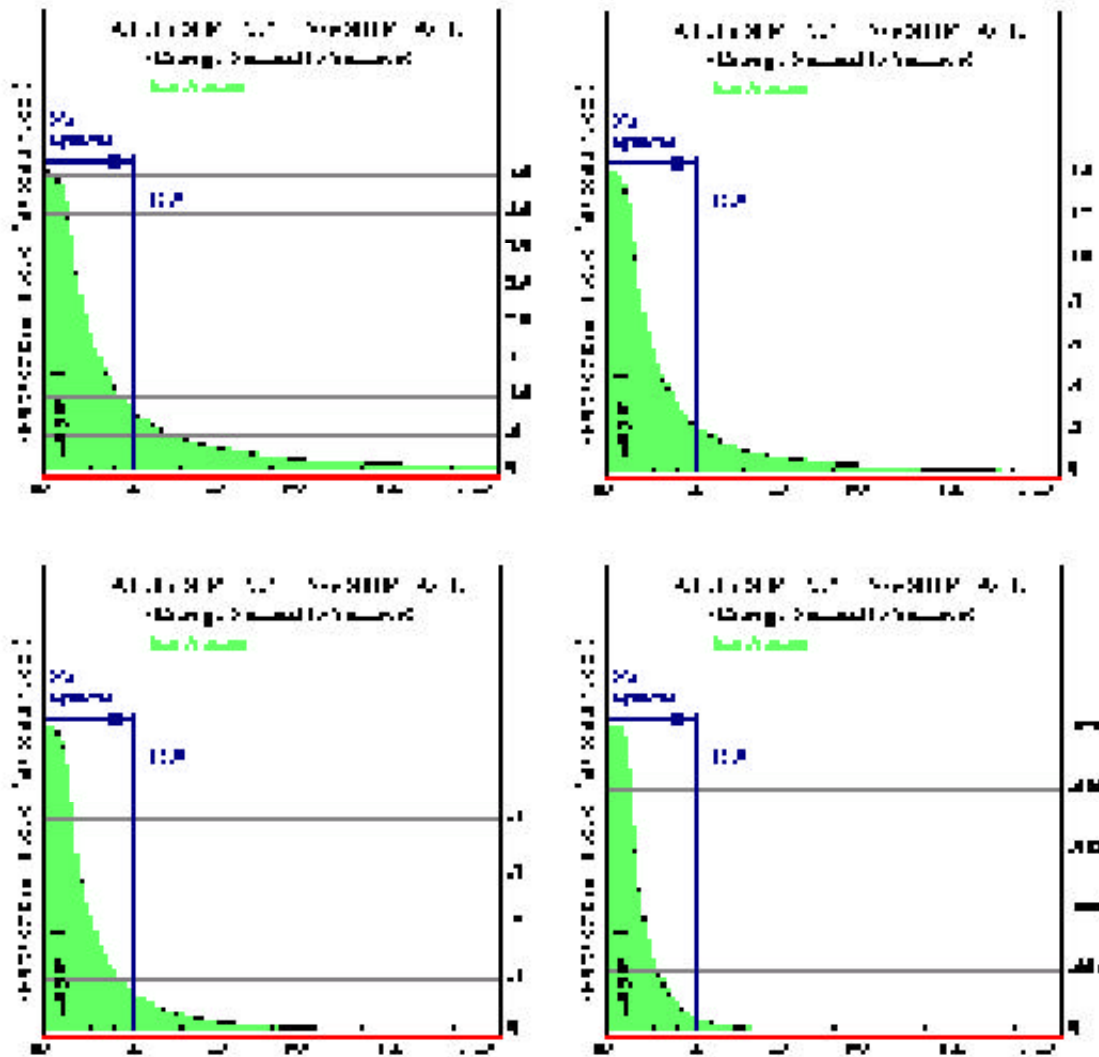


Figure 4.4: Distribution of the normal component of the kinetic energy of displaced atoms reaching the surface for a) 600; b) 200; c) 100; and d) 40-eV xenon ions on molybdenum.

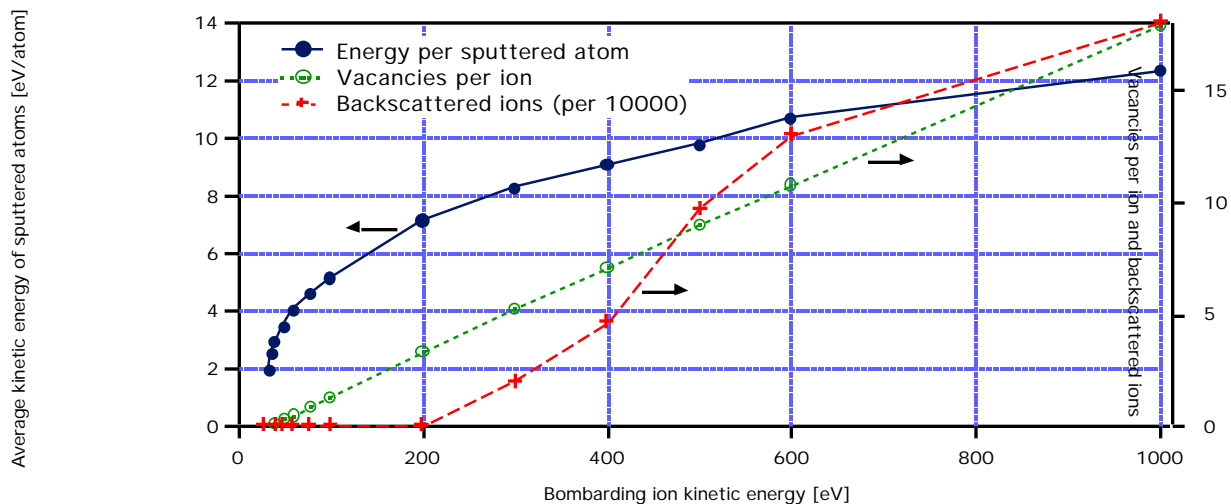


Figure 4.5: Average energy of sputtered atoms, number of backscattered ions and vacancies created per ion versus energy for xenon ion bombardment of molybdenum.

ens at higher energies, probably because of a greater penetration of the ions into the molybdenum (Fig. 4.6).

Figure 4.7 shows a plot of the contributions of ionization (a component of electronic energy loss), vacancy creation and phonons to the total energy losses of ions and recoil atoms. At higher energies, most of the energy lost by the ions is transferred to the atoms in collision cascades. For decreasing values of bombarding ion kinetic energy, a progressively larger amount of energy is lost to phonons, *i.e.*, transferred to atoms that do not gain sufficient energy to leave their lattice site.

### 4.3.3 Results on the Temperature Dependence of the Sputtering Yield

Sputtering is generally considered insensitive to target material temperature [72, 82], at least at energies not in the vicinity of the sputtering threshold energy. Because

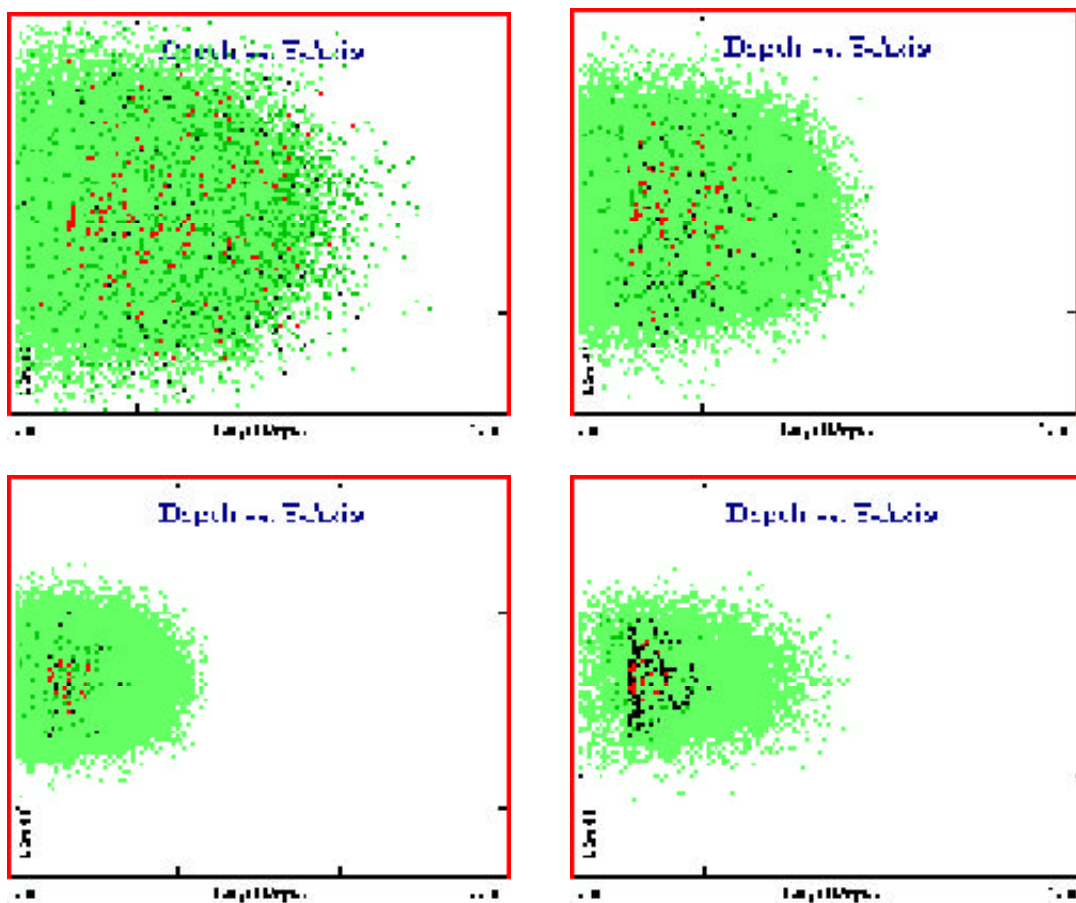


Figure 4.6: Longitudinal view of final recoil and ion positions for a) 600; b) 200; c) 100; and d) 40-eV xenon ions on molybdenum. The light dots are recoil atoms; the darker dots are ions.

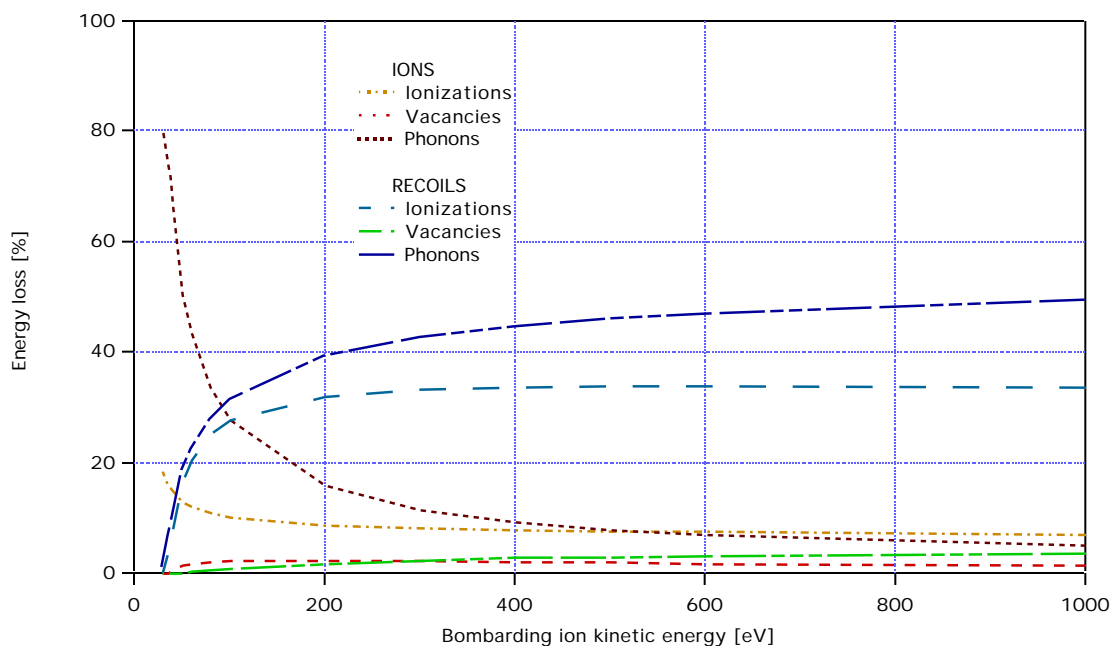


Figure 4.7: Contributions of ionization, vacancies and phonons to the energy loss of ions and recoil atoms for xenon bombardment of molybdenum.

surface sputtering can be very sensitive to the value of the surface binding energy, however, and particularly in the region near threshold, low energy sputtering yields may be found to vary significantly, at least in relative values, with temperature. This was suggested by Behrisch, who showed using the code TRIM.SP that the sputtering yield of silver by deuterium could be increased by a factor of four or more at high temperature because of the (weak) temperature dependence of the surface binding energy [99]. In this part, we investigate this phenomenon for xenon on molybdenum.

Although this may not be the case for all metals (*e.g.*, tungsten), the atomic heat of sublimation is found to decrease with temperature for most metals [140]. As shown in Fig. 4.8, the heat of sublimation for molybdenum decreases by about 2% between room temperature (298 K) and 2000 K.

We used TRIM calculations to investigate the relative sensitivity of the sputtering

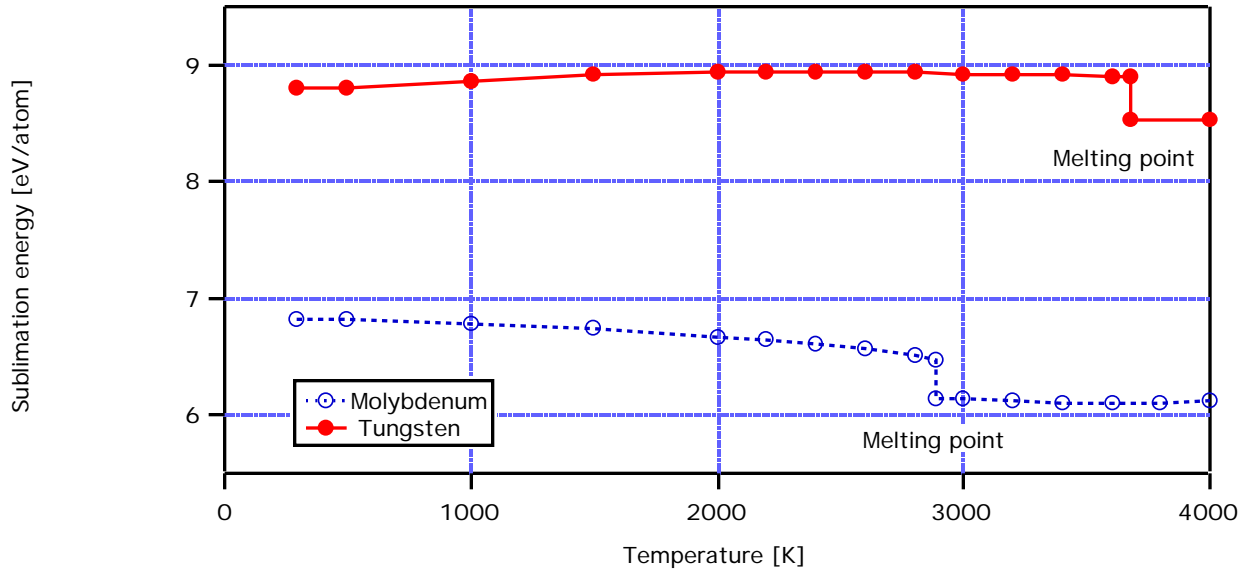


Figure 4.8: Dependence of the atomic heat of sublimation on temperature, for tungsten and molybdenum.

yield for xenon ions on molybdenum to a decrease in surface binding energy, which we consider well approximated by the atomic heat of sublimation. The increase of the sputtering yield with decreasing surface binding energy is best understood with differential plots generated from the distributions shown in Fig. 4.4. Such differential plots are shown in Fig. 4.9.

As in the case of deuterium on silver [99], the sputtering yield  $Y$  is found to be increasingly sensitive to changes in the surface binding energy  $U_b$  near threshold, as shown in Fig. 4.10 for normally-incident xenon ions on molybdenum. We note that although the sensitivity of sputtering to surface binding energy is indeed increased significantly in the threshold region, the *relative* increase in sputtering yield is not likely to exceed a few percent at the usual operating temperatures of the ion engine components subject erosion by low-energy sputtering.

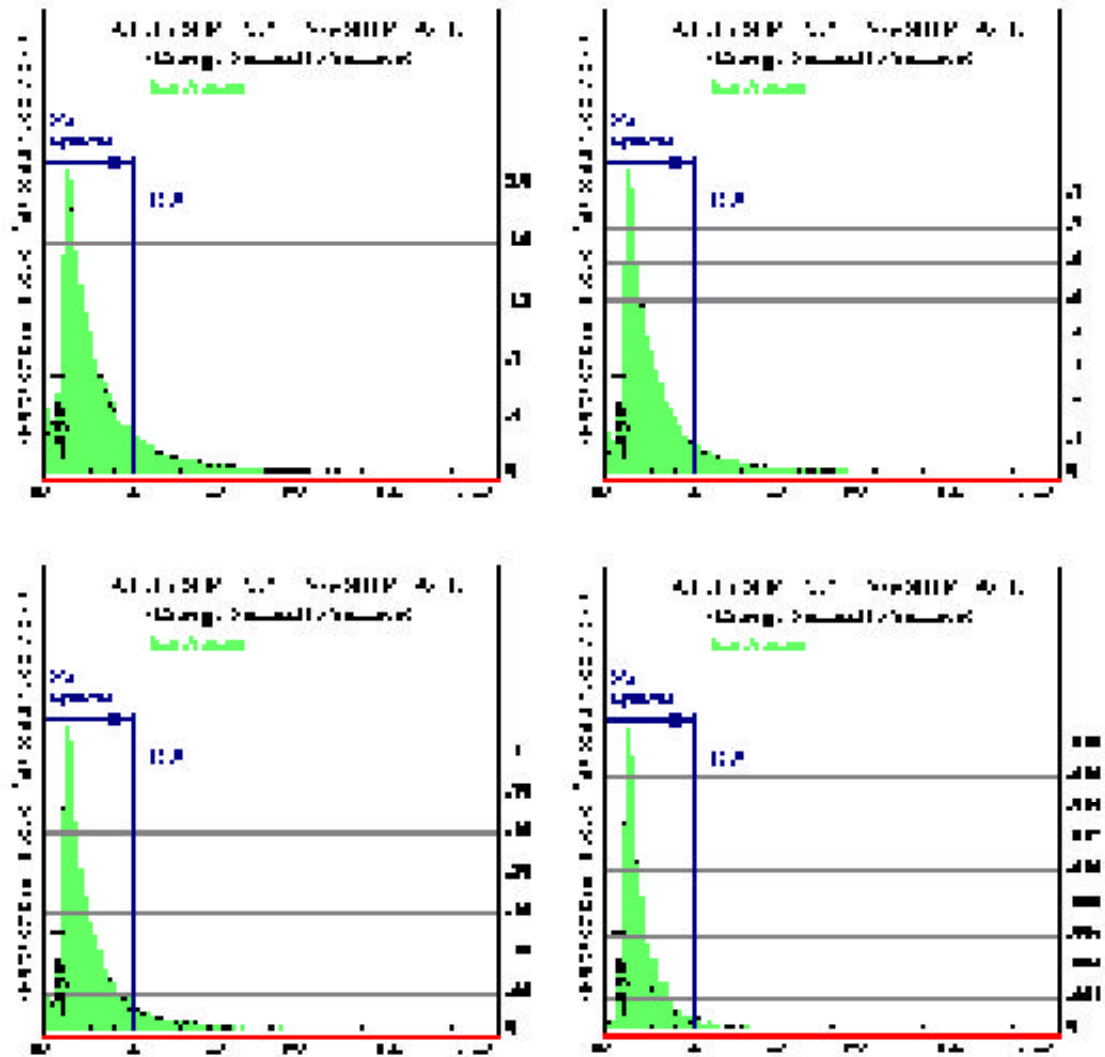


Figure 4.9: Differential plots of displaced atoms energy at the surface for xenon bombardment of molybdenum, for a bombarding ion kinetic energy of a) 600; b) 200; c) 100; and d) 40-eV xenon ions on molybdenum.

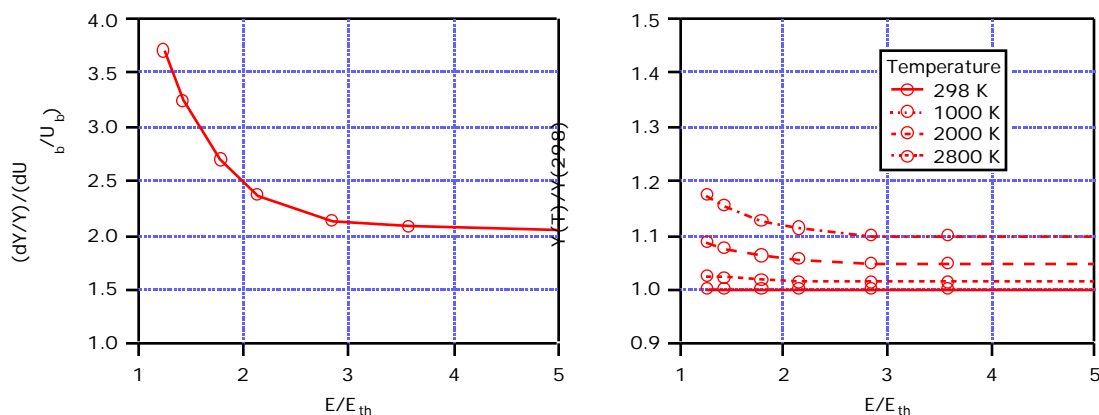


Figure 4.10: Sputtering yield dependence to surface binding energy (a) and temperature (b) at near-threshold energy for xenon on molybdenum. Sputtering yields are in relative values and kinetic energy is normalized by the threshold energy  $E_{th}$ .

## 4.4 Conclusions

In this chapter, a number of analytical tools applicable for the estimation of sputtering yields as a function of ion energy for slow, heavy ions have been reviewed. Among them, the expression proposed by Wilhelm has the best physical justification at energies near threshold, but remains difficult to use because it requires coefficients that are somewhat difficult to estimate. We proposed a value for the total scattering cross-section for use in the Wilhelm formula, and we have described a relatively simple model for estimating the sputtering threshold that considers inelastic (electronic) energy losses but still makes use of the binary collision approximation.

In addition, we showed that results of computer simulation using the TRIM Monte-Carlo code agreed well with available experimental data for energies greater than 100 eV, and followed the Wilhelm model surprisingly well below 100 eV, despite the treatment of all ion-atom interactions as binary collisions. We also studied the temperature dependence of sputtering in the near-threshold regime, and showed that

although an increased relative temperature sensitivity was found, it was not likely to introduce an error greater than a few percent on the sputtering yields of xenon ions on molybdenum, at least in the temperatures encountered during normal ion engine operations.

Finally, we noted in Chapter 3 that the surface binding energy may be different for practical surfaces than from ideal surfaces. If we assume a uncertainty on the binding energy of  $\pm 30\%$ , based on the discussion in Ref. [73], and use the sensitivity of sputtering yield to surface binding energy as a function of ion kinetic energy from Fig. 4.10a, the error in the TRIM results due to the uncertainty on the surface binding energy can be estimated. A figure showing the resulting error bars will be shown in Chapter 8.

We now turn for the next three chapters to a rather different subject—the experimental approach and results for the measurement of low-energy sputtering yields.

# Chapter 5

## The Quartz Crystal Microbalance Technique

Measuring sputtering yields for materials of interest in ion thruster technology with slow incident ions raises very serious experimental difficulties. The first one, which we address in this chapter, is that the vanishingly small amounts of sputtered material to be measured in an acceptable exposure time mandates the use of an extremely sensitive method and requires as high an ion current density as possible. In this chapter, we concentrate on the sensitivity issue and describe the use of a Quartz Crystal Microbalance (QCM) experimental technique to measure low-energy sputtering yields.

### 5.1 Low Energy Sputtering Measurement Techniques

This section briefly mentions the main experimental techniques historically implemented for the measurement of ion-bombardment induced erosion rates. A systematic review of sixteen different techniques has been written elsewhere [141], but we name six techniques here that were considered as candidates for the present experiments.

They are essentially based on one of the following observable phenomena:

- decrease of target mass;
- decrease of target thickness;
- accumulation of sputtered particles;
- presence of sputtered particles in the gas phase.

The first and most extensively used method involves measuring the weight loss of the eroded sample [102, 108, 111, 131, 136, 142–145]. While this method allows for absolute, direct measurements on all materials and is relatively simple, its sensitivity, limited to about  $10^{-3}$  atoms/ion with very high beam current densities, makes it inappropriate for the detection of erosion rates at energies near threshold. Because of its great versatility, however, it still has been used recently, *e.g.*, for the measurement of xenon ion sputtering of ceramics used in stationary plasma thrusters down to 350 eV [145].

Profilometry offers very similar benefits and disadvantages. This method involves measuring the depth of the sputtered surface with a micro-stylus, with reference to a masked area of the target. One difficulty with this method is that its precision depends on the eroded depth profile roughness [138, 146].

Askerov and Sena [106] used the change in the optical transmission of the plasma radiation to a photoresistor through the sputtered film deposited on a glass wall. Although this method has the advantage of being *in situ*, it is indirect and gives a relative value for the sputtering yield. In addition, its sensitivity is likely to be too limited when not used in conjunction with a high-density plasma as the source of ions.

Methods using radioactive tracers were proved by Morgulis and Tishchenko [103] and Handoo and Ray [147–149] to provide a great benefit in sensitivity, enabling measurements in the near threshold region. Such methods however present the inconvenience of requiring a suitable—in terms of half life and energy of the gamma-ray emissions—isotope for the material to be sputtered, which does not exist for molybdenum. Another solution may consist of activating a surface layer in the sample in a specialized facility [150].

Another large family of measurement techniques encompasses spectroscopic methods, such as optical spectroscopy [104,151,152], Auger Electron Spectroscopy (AES) [153], Rutherford Backscattering Spectroscopy (RBS) [137,154] or Secondary Neutral Mass Spectrometry (SNMS) [137]. Optical spectroscopy and SNMS are indirect methods and can only give relative sputtering yields. For instance, RBS was used by Bhattacharjee *et al.* [137] to calibrate measurements obtained with the more sensitive SNMS method. In addition, the most sensitive of these methods, optical spectroscopy and SNMS, require assumptions on the (non-isotropic) angular distribution of the emitted particles, which introduces an error in the total sputtering yield measurements.

Finally, a very sensitive method, using Quartz Crystal Microbalance (QCM) techniques, was first proposed by McKeown in 1960 [155]. It has since been implemented in several experimental studies on sputtering, for example in Refs. [156–160]. With modern-day frequency-measurement technology, using a QCM could theoretically enable direct—in fact, real time—*in situ* measurements of absolute sputtering yields as low as  $10^{-5}$  atoms/ion, even at low ion current density. A difficulty associated with this method is that it requires the sample material to be coated as an electrically-conducting, thin film (a few  $\mu\text{m}$  thick) on the piezoelectric quartz crystal. This

practically restricts it to the use of, mostly, metallic targets, and makes it less versatile than methods based on weight loss and profilometry. Because of its benefits, however, the QCM technique was elected as the method of choice in the present work, and its implementation in a relatively simple, novel way is described in the remainder of this chapter.

## 5.2 Physical Principle

The QCM is a device for the measurement of the areal mass density of thin films. It involves the use of a single quartz crystal electromechanical resonator supporting a thin film on one of its electrodes. The quartz crystal is electrically excited by a driver electrode, and resonates at a frequency that is strongly dependent on the mass of the film.

As mentioned above, the QCM technique presents the advantages of being relatively convenient to use, highly sensitive, direct, and to make possible dynamic, *in situ* measurements of absolute erosion data. It is commonly believed that correct use of this method requires a uniform dose of incident ions on the 1.4-cm diameter sample surface, but we will show here how additional care can be taken so that not only this limitation does not hold, but in fact a significant advantage can be gained from focusing the beam on a spot a few millimeters in diameter. In addition, significant and recent technical improvements have made the QCM technique even more attractive [161, 162], with advances pertaining to the oscillator (shape of the crystal and electrodes, electrode-to-quartz bonding), the transducer (supporting environment of the quartz), and perhaps even more significantly the electronics: the use of the micro-processor and modern electronics allow “intelligent” measurement

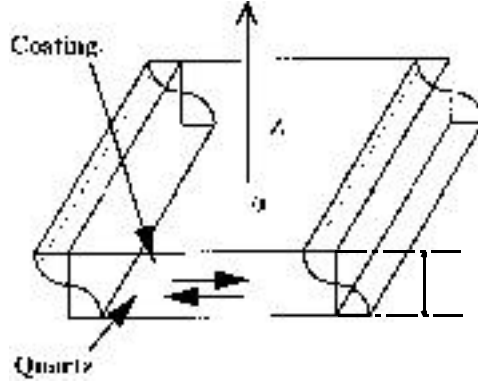


Figure 5.1: Planar resonator and fundamental thickness shear mode of vibration.

systems to not only determine the resonant frequency of the oscillator but also to verify that the crystal is oscillating in the desired mode. This greatly increased the speed, accuracy and precision (to better than 1 part in  $10^8$ ) of the instrument [161].

The relationship between the change in the resonant frequency  $\Delta f$  of a coated crystal oscillator, to the change in areal mass density  $\Delta\sigma$  at its surface, was expressed by Sauerbrey in 1959 [163] as

$$\frac{\Delta\sigma}{\sigma_0} = -\frac{\Delta f}{f_0} \quad (5.1)$$

where  $\sigma_0$  is the initial areal mass density and  $f_0$  is the initial resonant frequency of the oscillator. In the case of a planar resonator, as shown in Fig. 5.1, it can be seen that the positions  $z = \pm h$  are antinodes for the fundamental thickness-shear mode of oscillations, so that the thickness  $2h$  of the crystal corresponds to half a wavelength for this mode. We can write

$$2h = \frac{C_{AT}/2}{f_0} \quad (5.2)$$

where  $C_{AT}$  is the wave speed for a transverse wave propagating in the  $z$ -direction. The subscript AT refers to the orientation of the cut of the resonator with respect to the crystallographic axes. The standard AT-cut, referenced as (yxl)-35°15' under the 1978

Institute of Electrical and Electronics Engineers (IEEE) standard nomenclature [162, 164], is a special case of orientation that ensures oscillations in the thickness-shear mode, while having a resonant frequency rather insensitive to temperature variations, as will be discussed in the next section. This mode of vibration is the most sensitive to the addition or removal of mass for a quartz crystal resonator [162].

Introducing  $\rho_Q$ , the quartz density, and substituting Eq. 5.2 into Eq. 5.1 we have

$$\Delta\sigma = \frac{\rho_Q C_{AT}/2}{f_0^2} (f_0 - f) \quad (5.3)$$

where  $f$  is the frequency after the shift due to the surface loading. For a uniform layer on an infinite plate we therefore have

$$\Delta f = -C_f \Delta\sigma \quad (5.4)$$

where

$$C_f = \frac{f_0^2}{\rho_Q C_{AT}/2} \quad (5.5)$$

is the sensitivity constant for the resonator. With  $f_0 = 6$  MHz,  $\rho_Q = 2.649$  g/cm<sup>3</sup> and  $C_{AT} = 3322$  m/s, the values corresponding to the crystal in this study [165, 166], the sensitivity constant  $C_f$  is  $8.18 \times 10^7$  Hz·cm<sup>2</sup>/g. Thus, the removal of a uniform layer of 1 Å of molybdenum would correspond to an increase in the resonant frequency of 8.35 Hz, about a thousand times the theoretical resolution of the instrument. This simple principle has been applied to a great variety of surface science applications where monitoring deposition or etch rates is critical, *with the essential condition that the material thickness on the crystal electrode be uniform.*

### 5.3 Temperature Sensitivity

Piezoelectric quartz crystals are of great interest because they have a relatively simple mode spectrum, and a high sensitivity to mass changes. However, the coupling between the mechanical displacements and the electric potential, expressed through the piezoelectric constitutive equations, also makes the resonance frequency of such a resonator very sensitive to almost any physical change in its structure or environment. In particular, the temperature dependence of the resonant frequency can be described by a Taylor series with respect to a small temperature excursion [167]. Using the first-, second- and third-order temperature coefficients, the plot shown in Fig. 5.2 can be generated to show the effect of steady-state temperature changes on resonant frequency.

Although small change in the orientation of an AT-cut quartz crystal plate generally does not alter the mode of resonance, the effects of stress or temperature on the resonant frequency are found to be strongly dependent on the orientation of the cut with respect to the crystal axes. As seen on Fig. 5.2, the angle of cut can be chosen so that the temperature dependence is zero at the actual quartz temperature during the specific materials process considered. The crystals used in this study were 6-MHz quartz crystals with gold electrodes from Leybold Inficon, Inc., and had a nominal cut angle of  $35^{\circ}18'$ , or  $3'$  over the standard AT cut, for a reduced sensitivity to steady-state temperature variations in the region  $\approx 339\text{--}353\text{ K}$  ( $\approx 66\text{--}80^{\circ}\text{C}$ ). Still, we note that at room temperature, the frequency shift as a function of temperature for AT-cut crystals is  $0\pm 3\text{ Hz/K}$  [168], which translates into a thickness error for molybdenum of about  $0.35\text{ \AA/K}$ .

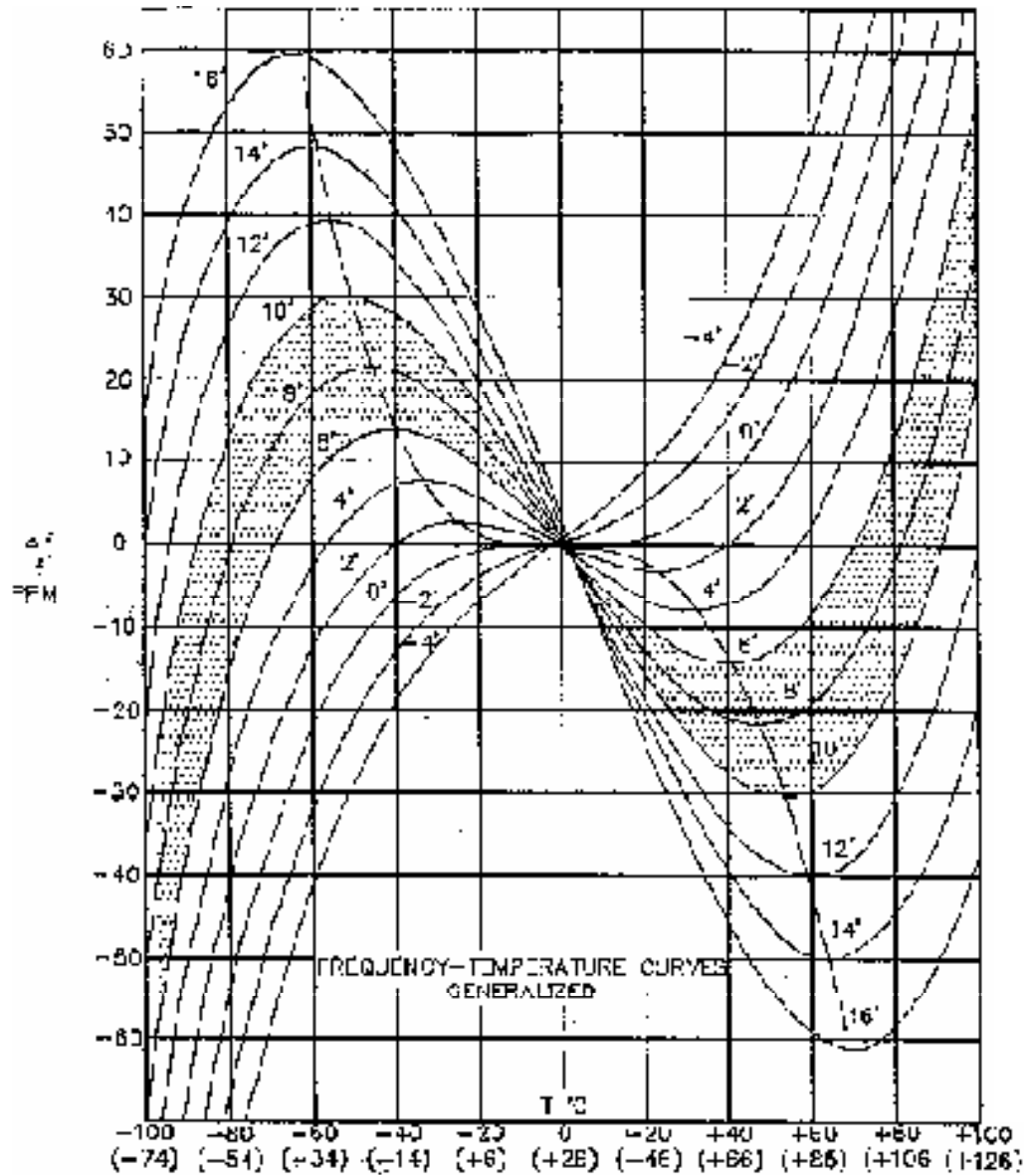


Figure 5.2: Frequency-temperature curves for the AT family of quartz crystal resonators. The angles, in minutes, represent the deviation from a  $35^{\circ}10'$  cut. The shaded area represents the tolerance on the angle of cut for the crystals used in this study. The discontinuous line is the set of zero temperature dependence points. From Ref. [161], courtesy Leybold Inficon.

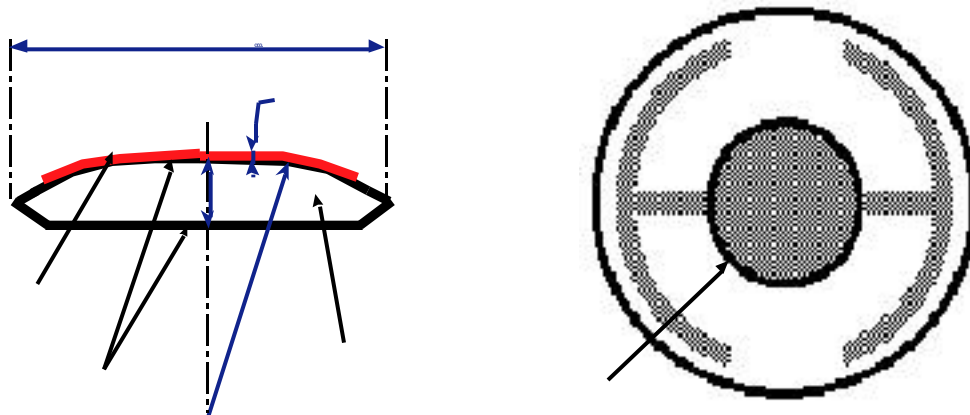


Figure 5.3: Plano-convex quartz crystal resonator. Left: edge view with top electrode coated; right: bottom view showing the driving electrode design, which allows for mechanical and electrical contact at the edges, while the excitation is confined to the center. Not to scale (the curvature has been exaggerated).

## 5.4 Differential Mass Sensitivity

Among the improvements brought to quartz crystal oscillators, the change from planar to plano-convex resonators was extremely significant. Along with the fact that the electrode responsible for the piezoelectric excitation is confined to the central region of the resonator (Fig. 5.3), the plano-convex shape participates greatly to the energy stability of such resonators by trapping the elastic waves into essentially total internal reflection, thus contributing to an extremely high quality factor for the resonator, and the resulting frequency stability [165].

As mentioned earlier, it is not always practical to have to work with a strictly uniform layer on the coated electrode. For a circular, plano-convex, finite resonator loaded with a point mass  $\Delta m$  (Fig. 5.3), Eq. 5.4 becomes [163]

$$\Delta f = -c_f(r, \theta) \Delta m \quad (5.6)$$

where  $c_f(r, \theta)$  is the differential mass sensitivity of the resonator, and  $r, \theta$  are the

local radial and azimuthal coordinates, respectively. The axis  $\theta = 0$  is oriented along the crystallographic  $x$ -direction. The mass sensitivity constant  $C_f$  is now given by the integral over the crystal surface area  $S$ , of the differential mass sensitivity  $c_f(r, \theta)$  [165], as expressed below

$$C_f = \iint_S c_f(r, \theta) ds \quad (5.7)$$

Eq. 5.7 is an important result. It shows that knowledge of the differential mass sensitivity allows the QCM to be applied to the measurement of masses known to be distributed unevenly across the resonator surface. This result is typically not mentioned in textbooks, and the validity of the generalization of Eq. 5.1 to finite resonators in order to obtain Eq. 5.7 is not obvious. Cumpson and Seah were the first to provide a rigorous derivation of this result in 1990 [165] by means of 3D perturbation theory. They obtained the fundamental result that “*the fractional change in resonant frequency on addition of a small point mass is proportional both to the added mass, and to the square of the vibration amplitude at the point to which it is added.*” Their thorough theoretical analysis of the response of AT-cut quartz crystal microbalances, along with the modal analyses of Tiersten and Smythe [169], leads to the following analytical solution for the radial and polar dependence of mass sensitivity

$$c_f(r, \theta) = c_0 \exp[-r^2(\alpha_1 \cos^2 \theta + \beta_1 \sin^2 \theta)] \quad (5.8)$$

where

$$c_0 = \frac{f_0^2 (\alpha_1 \beta_1)^{1/2}}{\pi \rho_Q C_{AT}/2} \quad (5.9)$$

and

$$\alpha_1^2 = \frac{\pi^2 \overline{C}_{66}}{8R h_0^3 M_1} \left( 1 - \frac{8k_{26}^2}{\pi^2} - \frac{2 \rho_E h_E}{\rho_Q h_0} \right) \quad (5.10)$$

$$\beta_1^2 = \frac{\pi^2 \overline{C}_{66}}{8R h_0^3 C_{55}} \left( 1 - \frac{8k_{26}^2}{\pi^2} - \frac{2 \rho_E h_E}{\rho_Q h_0} \right) \quad (5.11)$$

In the above expressions,  $M_1$ ,  $k_{26}^2$ ,  $C_{55}$  and  $\overline{C_{66}}$  are quantities derived from the elastic modulus tensor and the piezoelectric coupling constants of quartz. For the oscillators used in this study, they have the following numerical values [169]

$$\overline{C_{66}} = 2.924 \times 10^{10} \text{ N}\cdot\text{m}^2$$

$$C_{55} = 6.881 \times 10^{10} \text{ N}\cdot\text{m}^2$$

$$M_1 = 1.10 \times 10^{11} \text{ N}\cdot\text{m}^2$$

$$k_{26}^2 = 7.744 \times 10^{-3}$$

The quantities  $h_E$  and  $\rho_E$  are the electrode (coating) material thickness and density, and  $R$  is the radius of curvature of the plano-convex crystal surface, 0.212 m (2.5 diopters) here. Finally,  $h_0$  is half the maximum crystal thickness, at the center of the resonator, as illustrated in Fig. 5.3, and we have  $h_0 = 0.15$  mm. Fig. 5.4 shows a plot of  $c_f(r, \theta)$ . Since the crystal is anisotropic, *i.e.*,  $\alpha_1 \neq \beta_1$  in general, the plot is the product of two-gaussians. A stretch in the  $x$ -direction from a simple gaussian is best visible on the lower (density) plot.

As mentioned earlier and as shown by Cumpson and Seah [165], the differential mass-sensitivity at any point is proportional to the square of the vibration amplitude at that point. Fig. 5.4 thus illustrates how, due to the convexity of the resonator surface and the small size of the excitation electrode (Fig. 5.3), the energy of the oscillation is trapped at the center so that very little dissipation occurs at the edge. This explains why the quality factor of such resonators is so large, and the resonant frequency so stable. Because of the negligible effect of the boundary conditions, this also justifies that the crystal can be clamped at the electrode edges without modifying the modal amplitude function.

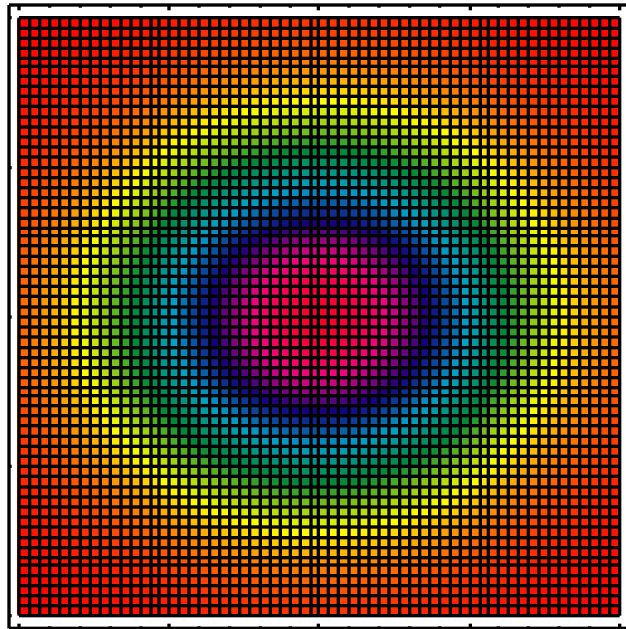
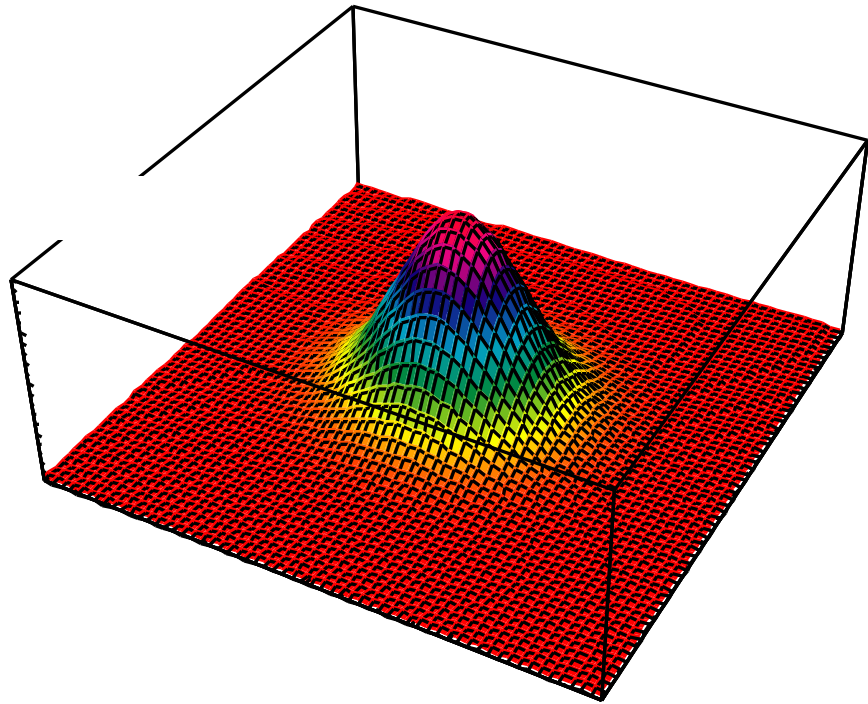


Figure 5.4: Differential mass sensitivity for a 6-MHz, plano-convex quartz crystal resonator.

As a final note, it should be added that the electronic equivalent of the crystal resonator is roughly equivalent to a sharply-tuned LCR circuit [161]. The resonant frequency is found by comparing the phase of the current driving the electromechanical oscillator to that of the current passing through the crystal, which should be zero at resonance, *i.e.*, the crystal then behaves as a pure resistance. The fact that the operation of the instrument relies on the phase of the current passing between the electrodes of the crystal justifies why a DC current on the coated electrode, *e.g.*, from the bombarding ion beam, does not interfere with the operation of the QCM.

## 5.5 Practical Implementation: The Current-Sensitivity Integral

As explained earlier, the QCM operates by sensing a shift in the resonant frequency of a single crystal piezoelectric quartz resonator. The frequency information is then converted to a measured thickness change  $\Delta\tau_{meas}$  and sent by the QCM monitor through the recorder output to the data acquisition system. That measured thickness change, however, does not account for the non-uniformity of sputtering over the sample surface due to the non-uniform ion beam current density profile.

The sputtering yield  $Y$  at any radial position  $r$  on the sample is given by Eq. 3.1, which we recall below:

$$Y = \frac{\text{number of atoms removed}}{\text{number of incident particles}}$$

which can be rewritten

$$Y = \frac{\Delta\tau(r) N ds}{\Delta t \frac{J(r)}{e} ds} \quad (5.12)$$

where  $\Delta\tau(r)$  is the local thickness change—assumed axisymmetric, as well as the

beam— $ds$  is an elementary surface area,  $N$  is the atomic number density of the sample material,  $\Delta t$  is the duration of exposure,  $J(r)$  is the local beam current density, and  $e$  is the electronic charge. The measured thickness change  $\Delta\tau_{meas}$  is a surface-average of the local thickness change over the sensor area. The crystal differential mass-sensitivity,  $c_f(r, \theta)$ , acts as a weighing function for this average, as seen below. From Eqs. 5.4 and 5.6 we have

$$C_f \Delta\tau_{meas} \rho_E = \iint_S c_f(r, \theta) dm \quad (5.13)$$

where  $C_f$  is given by Eq. 5.7,  $dm$  is a point mass element, and  $\rho_E$  is the density of the coated electrode, *i.e.*, of the material subject to sputtering. This in turn leads to

$$\Delta\tau_{meas} = \frac{1}{C_f} \iint_S \Delta\tau(r) c_f(r, \theta) ds \quad (5.14)$$

From Eq. 5.12 then

$$\Delta\tau_{meas} = \frac{1}{C_f} \iint_S c_f(r, \theta) \left[ Y \Delta t \frac{J(r)}{N e} \right] ds \quad (5.15)$$

Finally, the sputtering yield is given by

$$Y = \frac{\Delta\tau_{meas} N e C_f}{\Delta t \int_0^a \int_0^{2\pi} c_f(r, \theta) J(r) r dr d\theta} \quad (5.16)$$

where we have related the “apparent” eroded thickness  $\Delta\tau_{meas}$  for the instrument to the sputtering yield  $Y$ , by numerically integrating the product of the known beam current density profile  $J(r)$  and the analytical expression for  $c_f(r, \theta)$  given in Eq. 5.8.

In this expression,  $a$  is the radius of the sensor active area, and the integral over the surface area in the denominator of the right-hand side, normalized by  $C_f$ , will be called the Current-Sensitivity Integral (CSI). The CSI represents the effective average beam current density from the point of view of the sensor, and becomes larger, at constant total current, as the beam is focused to a smaller spot at the center of the

electrode, due to the gaussian nature of  $c_f(r, \theta)$ . The benefit of focusing is in fact twofold, as even the total beam current extracted from the ion gun tends to increase with focusing voltage. It should, however, be noted that an excessively focused beam results in a greater alignment sensitivity. It is therefore recommended to maintain a moderate focusing for the experiments, as the available beam current density will allow, thus keeping the spot size (95% of the beam current) to about 4 mm in diameter.

## 5.6 Conclusions

Among the candidate methods for experimentally measuring extremely low erosion rates, the use of a QCM is one of the most sensitive, with a theoretical eroded thickness detection limit of 0.012 Å for molybdenum based on the crystal mass sensitivity and the precision in the resonant frequency. The practical thickness resolution of the instrument, limited by the recorder output resolution (12 bits over a range of 2000 Å), is 0.5 Å. In addition to its sensitivity, the QCM method is relatively simple and inexpensive in terms of laboratory apparatus and allows direct, dynamic, and *in situ* measurements of absolute sputtering yields. The main difficulties associated with this method are its limited versatility, and its sensitivity to other physical quantities such as temperature or surface stresses, although these effects can be compensated—separately—by appropriate resonator cuts relative to the crystallographic axes.

In order to measure sputtering yields in the near-threshold region using a well defined, but low current density ion beam, we showed that it is not only possible to avoid having to spread the current uniformly over the entire surface area of the sensor, but that in fact a great advantage can be gained from the strong spatial dependence of the differential mass sensitivity of the crystal. We have shown that the

sputtering yield can be determined from the effective eroded thickness measured by the instrument, and that the effective average beam current density in the experiment can be greatly increased by focusing the beam to the center of the sensor, due to the gaussian nature of the differential mass sensitivity. We now turn to the description of the experimental setup and of the results of low-energy sputtering yield measurements implementing the method that we have just described.

## Chapter 6

# Experimental Measurements of Low Energy Sputtering Yields

In Chapter 5, we devised a method to implement a technique sensitive enough to allow for sputtering measurements in the threshold region. We now address the other experimental difficulties associated with low energy sputtering, and describe the apparatus and facility built to conduct the experiments. The sample preparation method is explained. Finally, the results are presented and discussed.

### 6.1 Apparatus and Procedure

#### 6.1.1 Vacuum Chamber

The experiments were conducted in a small vacuum chamber (Fig. 6.1) consisting primarily of a 117.5-mm (4-5/8") six-way cross fitted with conical reducers. The vacuum chamber is bolted on a Pfeiffer TPU 270 turbomolecular pump and evacuated to a total base pressure in the low  $10^{-6}$ -Pa ( $10^{-8}$ -Torr) range, after overnight bakeout

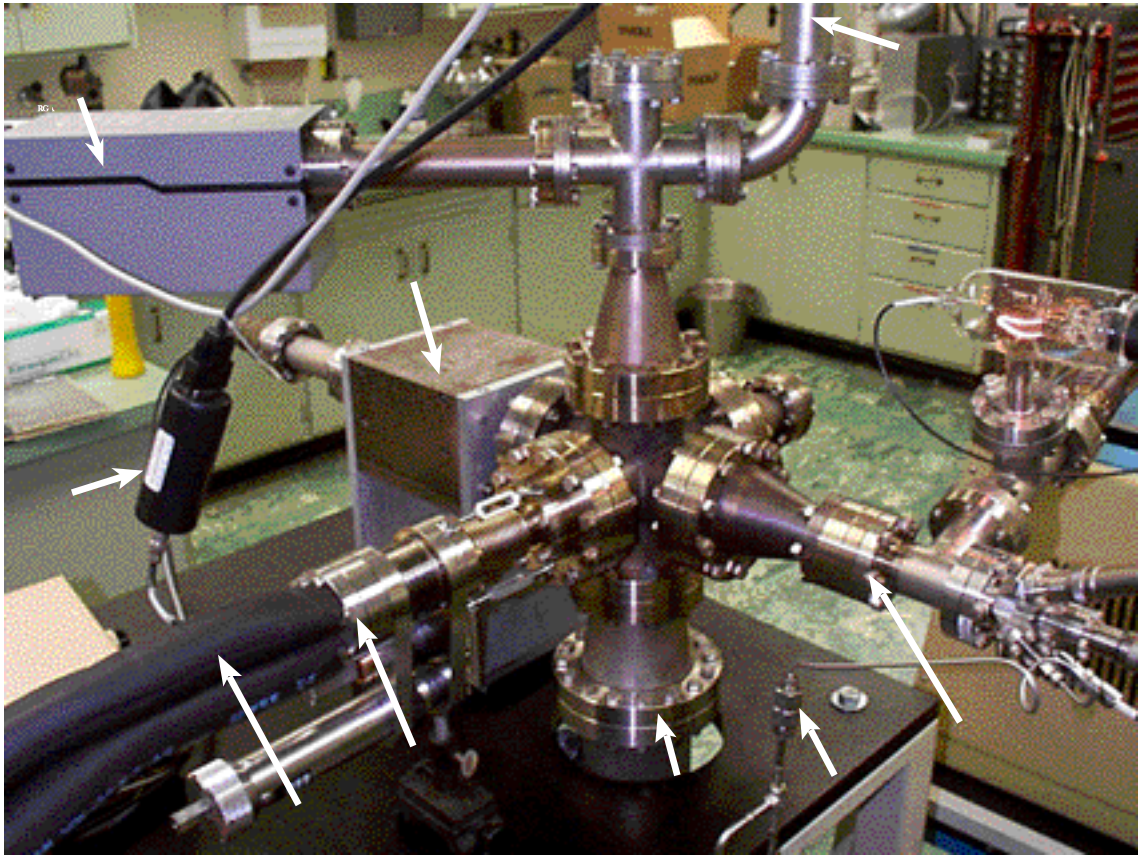


Figure 6.1: JPL facility for low energy sputtering yield measurements.

at  $\approx 200^\circ\text{C}$ .

A low background gas pressure was a critical requirement for the vacuum system. First, it needs to be low enough in order to ensure that the mean free path of the ions is larger than the source-to-target distance, so that uniformity of the beam in energy and incidence angle is not compromised. Second, and perhaps even more importantly, an ultra-high vacuum is also required in order to prevent the formation of a protective, chemisorbed impurity layer at the target surface. This critical problem is related to the ion beam current density at the target and will be addressed in greater details in Section 4.

### 6.1.2 Ion Source

The requirements for the source of ions are twofold, and essentially antagonistic. First, the ion beam should have as low an energy spread and as low a divergence angle as possible, to ensure a well-controlled ion energy and incidence angle. This implies, in particular, that the multiply-charged ion current be as small as possible, which in turn requires a low discharge voltage. Second, the beam current density at the target surface should be as high as possible in order to result in a measurable etch rate. For instance, a beam current density  $J$  of  $1 \mu\text{A}/\text{cm}^2$  at the target would, assuming a sputtering yield of  $10^{-4}$  atoms/ion, require about 34 hours to etch  $0.12 \text{ \AA}$  of molybdenum. Such an eroded thickness in molybdenum would result in a resonant frequency shift of 1 Hz for the 6-MHz QCM used in this study—a change in the measured signal of the order of 1 part in ten million. Another, final concern regarding the beam could be the presence of fast neutrals due to charge exchange collisions in, or downstream of, the ion source.

The choice for the method to generate and accelerate the ions therefore needs to be the result of a trade off between the relatively high current densities achievable with a plasma discharge (typically up to  $15 \text{ mA}/\text{cm}^2$ , and even higher for compressed plasma discharges [104, 106]) and the better-defined beam—in terms of energy, incidence angle, and purity—obtained with an ion gun. The beam current density extracted from an ion gun is constrained by the space charge limitation, proportional to the power  $3/2$  of the accelerating voltage.

In order to achieve a high level of control in energy, incidence angle, and purity of the ion beam, an ion gun was chosen to generate and accelerate the ions. We used, in the experiments described here, the ILG-2C ion gun built by Kimball Physics, Inc. A schematic is shown in Fig. 6.2. The beam energy is adjustable from 10 eV to 1

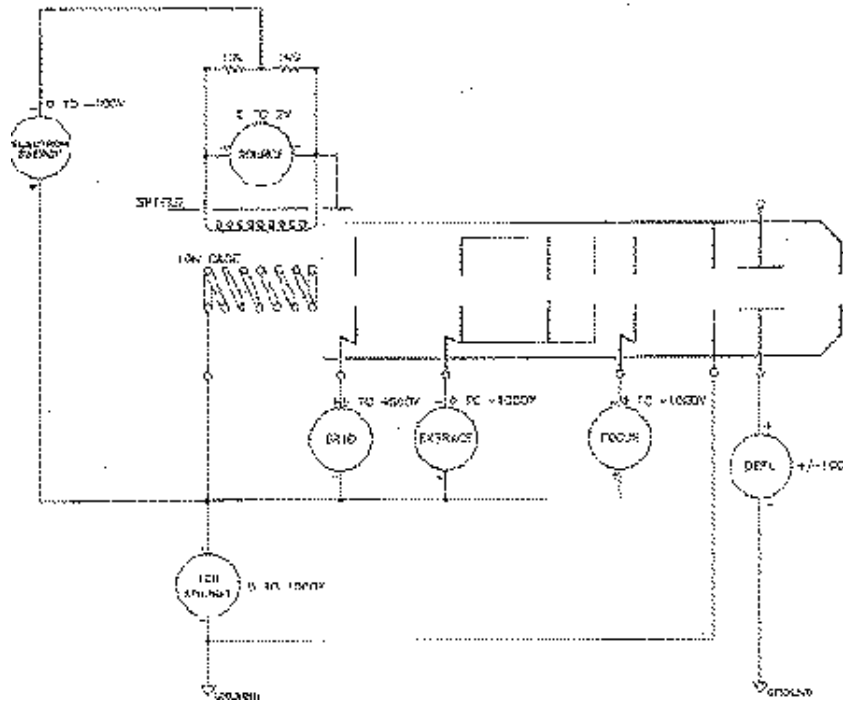


Figure 6.2: Electrical schematic of the ion gun.

keV, with a maximum total beam current on xenon of the order of 100 nA. The beam can be focused to a spot size—containing 95% of the current—less than 4 mm in diameter on the sample, which was positioned 1 cm downstream of the ion gun. The energy spread varies from 20 eV down to 4 eV for a beam energy of 1 keV and 100 eV, respectively. The energy stability (taken from the power supply specifications) is 0.01%.

The ion gun was differentially-pumped using a VEECO MS-20T leak detector equipped with a Pfeiffer TPU 050 turbomolecular pump. This provided a net pumping speed of the order of a liter per second in the source region.

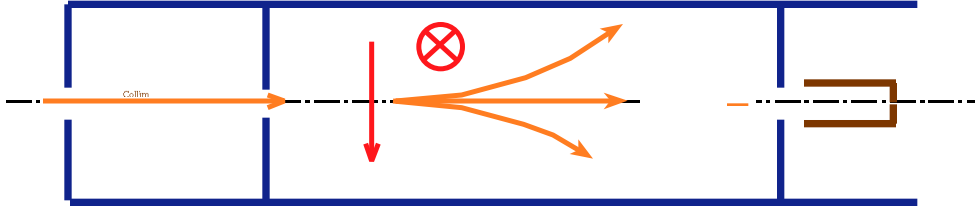


Figure 6.3: Schematic diagram of the  $E \times B$  velocity filter built for the experiments. Only the ions admitted with velocity  $V_i = V_{i0} = E/B$  follow a trajectory along the centerline and can reach the collector.

### 6.1.3 Beam Diagnostics

Ion energy distributions were obtained using a Wien velocity filter, also called an  $E \times B$  probe because it uses mutually perpendicular electric and magnetic fields normal to the ion trajectory [170]. Designed and built specifically for this experiment, it is shown schematically in Fig. 6.3. The  $E \times B$  probe was used to characterize the energy spread of the ion source, and to determine the doubly-to-singly charged ion ratio.

The energy spread in the experiments is illustrated by Fig. 6.4, where the  $E \times B$  traces are compared for beams of 100-, 400-, and 800-eV xenon ions. In relative values, the energy spread, given by the standard deviation of the best Gaussian fit, is fairly constant over the energy range considered: 3.34%, 2.53% and 2.51%, respectively. The energy distribution obtained for 100 eV was confirmed with Langmuir probe data. The energy spread at higher energies is comparable to the spread that would result from a misalignment angle of up to  $0.2^\circ$  between the incoming ions and the probe's long axis. Such a misalignment is consistent with the geometry and physical dimensions of the  $E \times B$  probe. Thermalization of the beam ions is expected to become a factor at energies of  $\sim 100$  eV and below, and can explain the increasing (relative) energy spread observed at 100 eV. At this energy, the mean free path for xenon ions in xenon at the ion gun operating pressure ( $\approx 7.5 \times 10^{-7}$  Pa, or  $\approx 1 \times 10^{-4}$  Torr) is

of the order of half a meter.

Figure 6.5 shows  $E \times B$  traces for 400-eV xenon ions for different values of discharge voltage (or electron energy). In the xenon ion kinetic energy range considered here, a discharge voltage of 50 V was chosen to optimize the beam current and the doubly-to-singly charged ion current ratio, which was limited to  $\approx 5\%$ .

Beam current density profiles were obtained for each run at the corresponding ion gun and pressure settings by means of a small Faraday cup with a 2-mm circular aperture. A sample profile is shown in Fig. 6.6 for two different values of focusing voltage.

In addition to the beam profiles taken prior to each experiment, the current collected by the sample was measured and recorded continuously. The current collected by a 34-mm circular graphite mask with an 8-mm aperture placed in front of the sample was also monitored and recorded.

#### 6.1.4 Sputtering Measurements

The Quartz Crystal Microbalance (QCM) technique, discussed in detail in Chapter 5, was used to measure the amount of molybdenum etched from the sample by the xenon ion bombardment. The QCM sensor, holding the quartz crystal resonator coated with a sputter-deposited film of molybdenum, could be moved in the direction perpendicular to the beam by means of a linear motion feedthrough. The motion feedthrough itself was mounted on a flexible coupling to allow for gross positioning and alignment corrections (Fig. 6.1).

As shown in Figs. 6.7 and 6.8, the QCM sensor and crystal holder were modified to break the electrical continuity between the molybdenum-coated electrode of the quartz crystal and the crystal holder (ground). This was done in order to allow

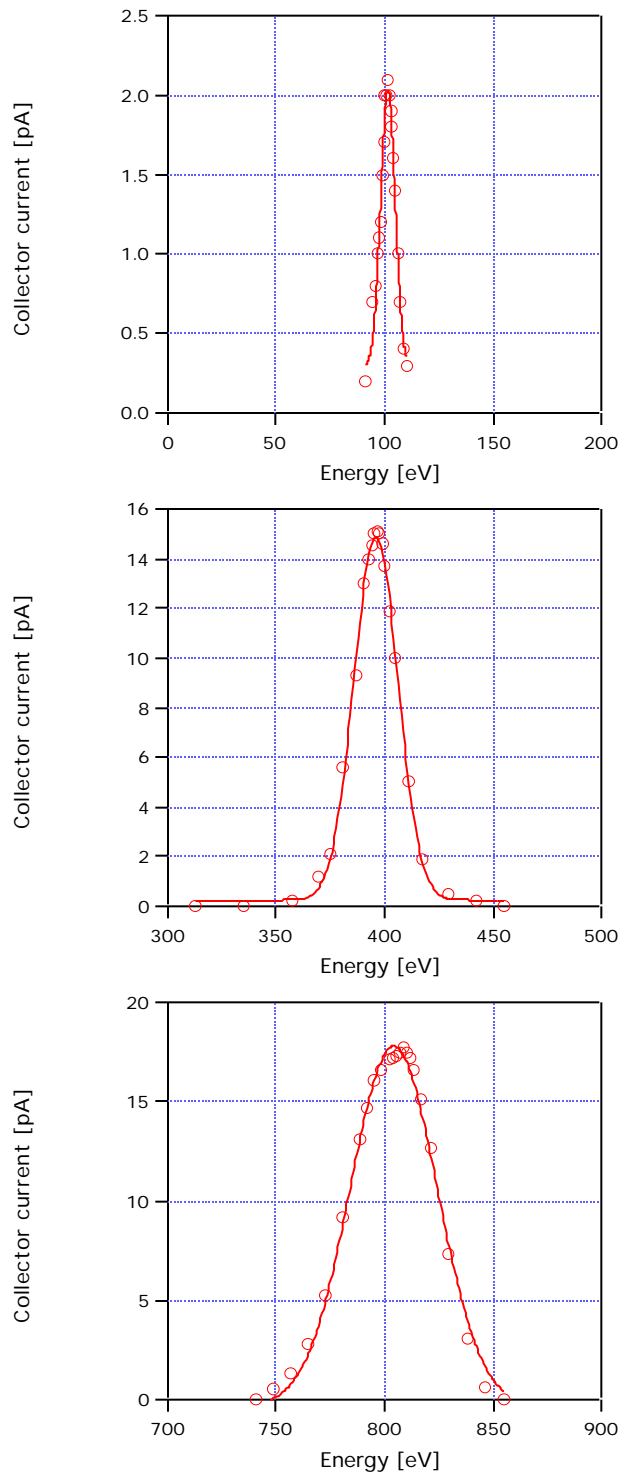


Figure 6.4:  $E \times B$  traces for 100-, 400-, and 800-eV xenon ions (from top to bottom). The lines are Gaussian fits, and the respective standard deviations are 3.34, 10.10, and 20.07 eV.

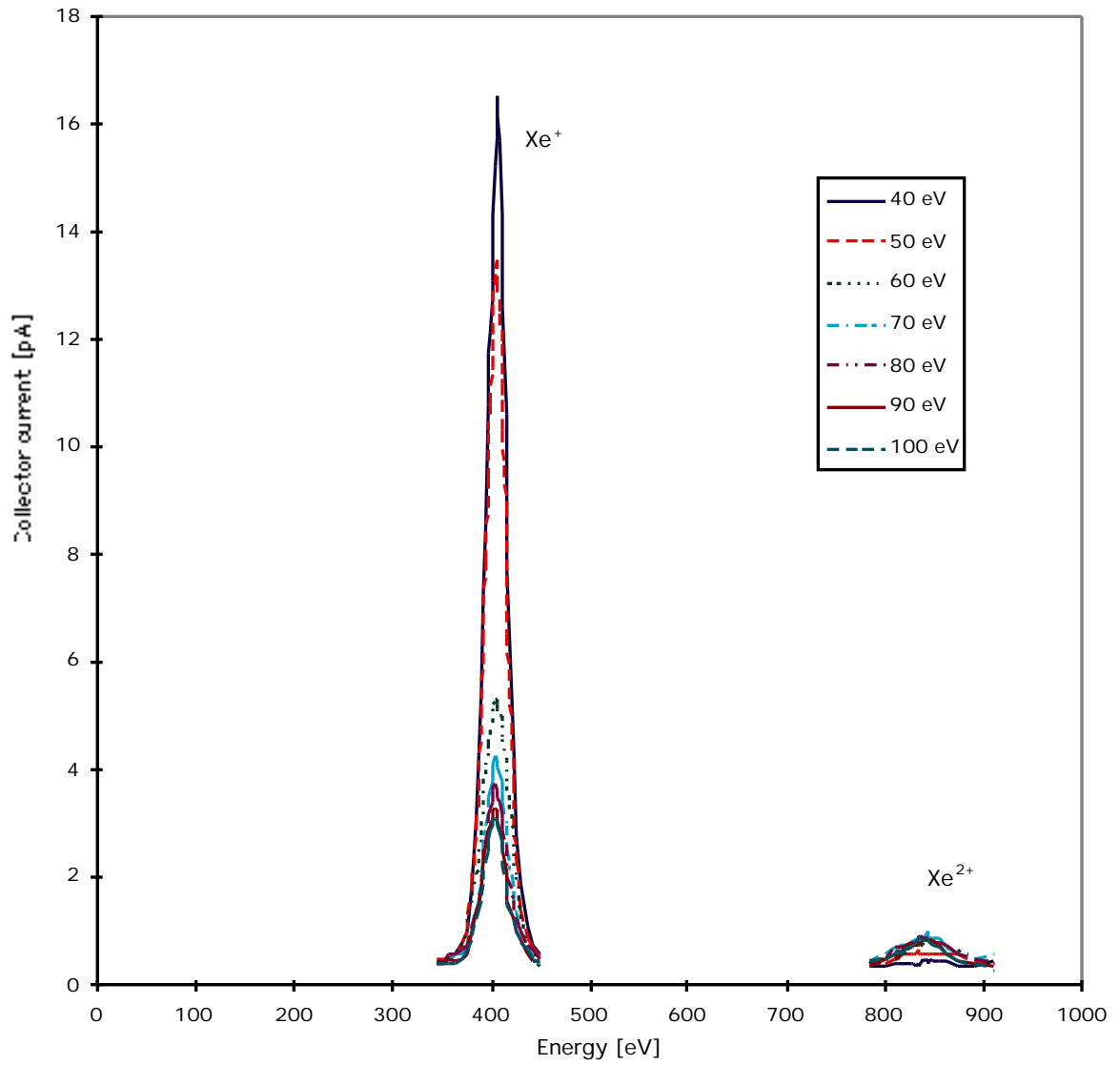


Figure 6.5:  $E \times B$  traces vs. discharge voltage for 400-eV singly- and doubly-charged xenon ions. Decreasing height for the singly-charged xenon ion peak corresponds to increasing discharge voltage.

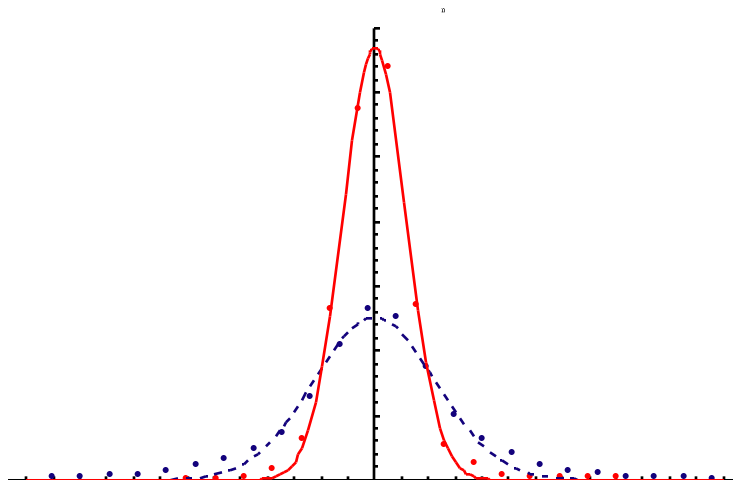


Figure 6.6: Radial beam current density profiles for two different focusing voltages.

monitoring of the portion of beam current impinging on the molybdenum sample. The coated electrode was thus grounded through a picoammeter. In addition, a 34-mm graphite mask was mounted on the crystal holder to protect the whole assembly from ion-induced erosion. The beam current collected by this mask was also monitored. An electrical schematic of the QCM sensor assembly is shown in Fig. 6.8. The arrangement was similar to the one described in Ref. [141].

### 6.1.5 Other Diagnostics

A Stanford Research Systems RG200 Residual Gas Analyzer (RGA) mounted on the chamber was used to monitor the background gas composition in the vacuum system. The diagnostics also included a T-type thermocouple junction in contact with the crystal holder. In addition, a circulating bath was used to regulate the QCM sensor temperature within  $\pm 0.2^\circ\text{C}$  at room temperature.

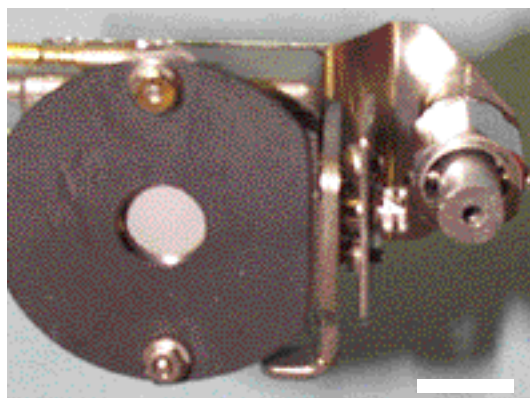
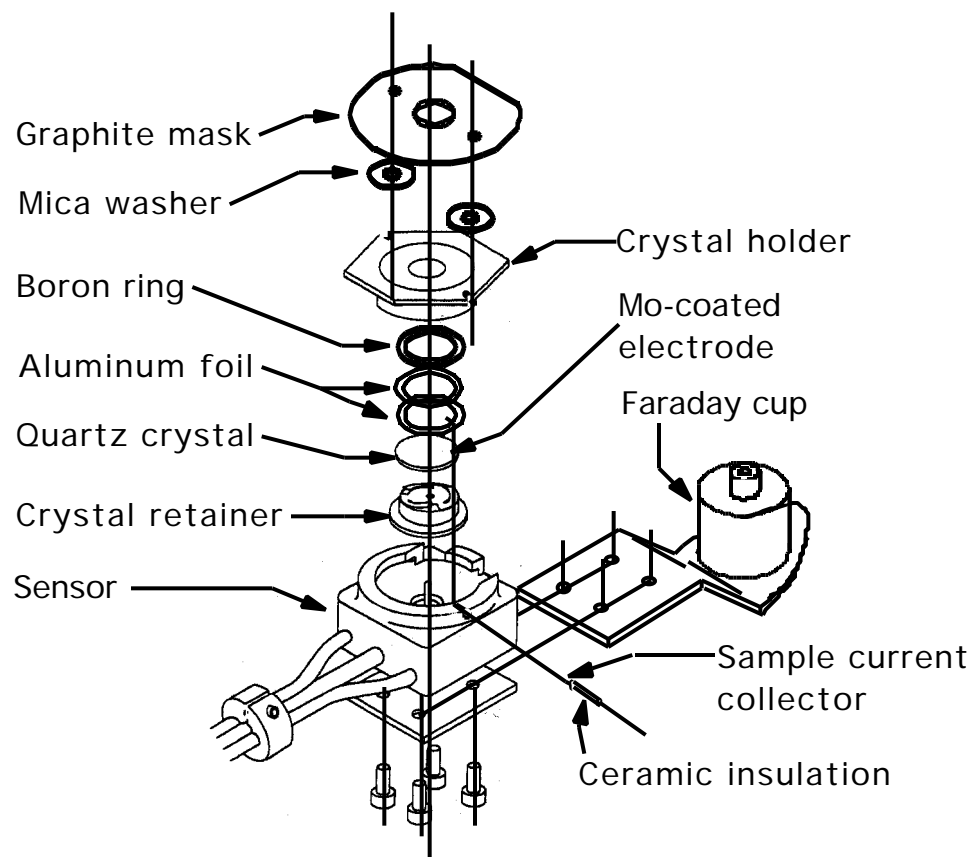


Figure 6.7: QCM sensor assembly. Exploded view, top; assembled, bottom.

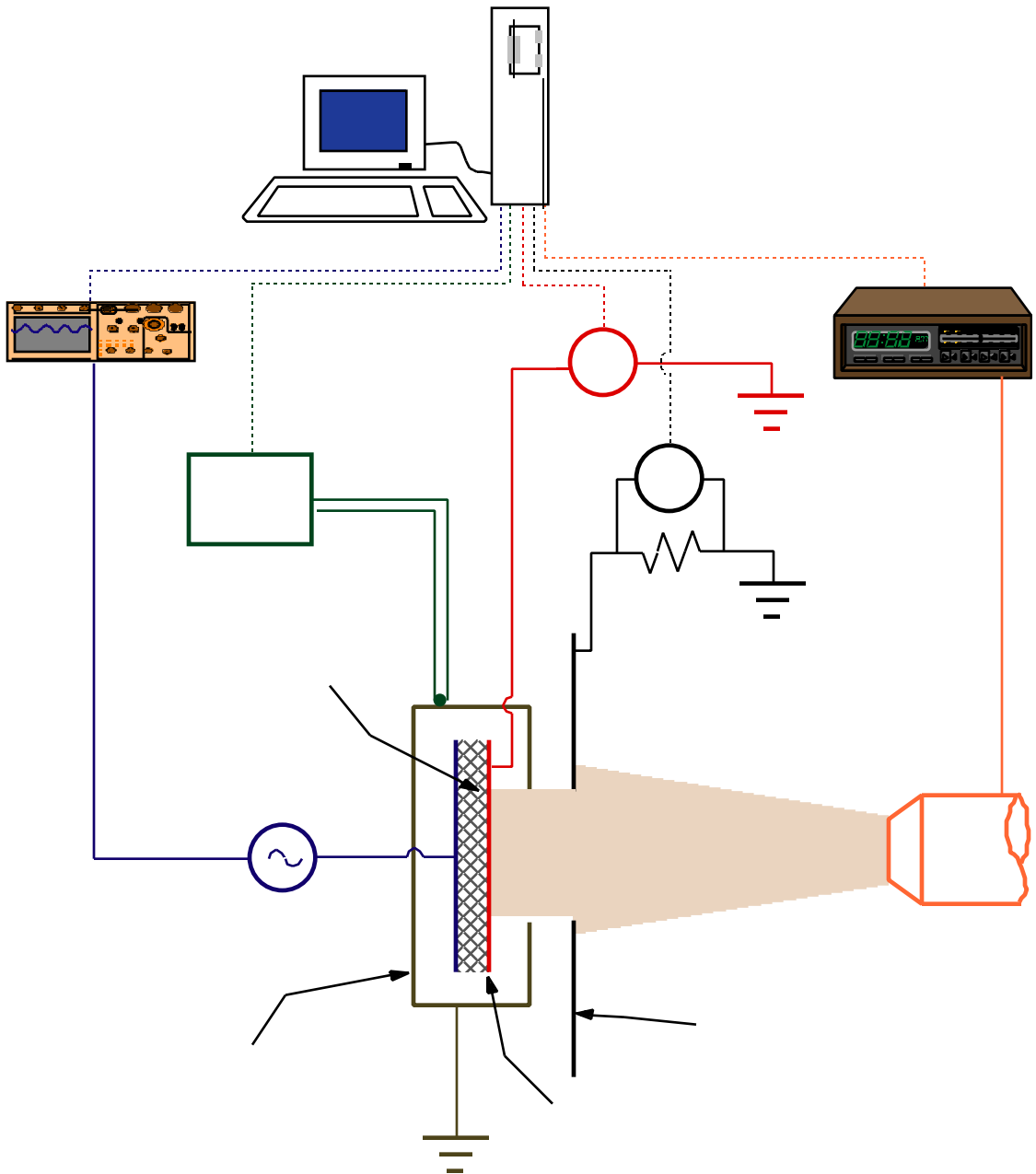


Figure 6.8: Electrical schematic of the QCM sensor assembly, and data acquisition.

### 6.1.6 Data Acquisition

All parameters monitored during the sputtering experiments were averaged over 200 to 500 measurements depending on the sampling frequency. The seventeen recorded parameters were as follows: elapsed time; ten ion gun parameters including ion energy; mask current; sample current; crystal holder temperature; molybdenum film thickness returned by the QCM monitor; ion source pressure; and vacuum chamber total pressure.

The signals were processed by National Instruments 5B-series analog signal conditioning modules with  $\pm 5$ -V outputs and acquired by computer via a National Instruments PCI-MIO-16XE-50 series DAQ board. The data acquisition routines were written in LabVIEW. In addition, the residual gas partial pressure data were recorded on a specific computer.

### 6.1.7 Experimental Procedure

The following sequence was followed when running an experiment:

1. turn on the cooling system and wait for the temperature to stabilize;
2. turn on the residual gas analyzer to acquire base pressure data;
3. select the ion gun operating point;
4. establish the proper xenon pressure of  $\approx 1.5 \times 10^{-6}$  Pa ( $2 \times 10^{-4}$  Torr) in the source region of the ion gun;
5. turn on the ion gun to the selected operating point;
6. obtain the current density profile versus radial position across the ion beam with the Faraday probe, noting the exact position of the center of the beam;

7. place the center of the molybdenum-coated quartz crystal electrode at that position and begin recording all parameters;
8. after a measurable amount of material has been eroded, turn off the ion gun and keep recording for a time comparable to the duration of exposure.

For experiments at ion energies below 400 eV and at the beginning of step 7, the sample was sputter-cleaned at 1 keV with a broader beam until at least 10 Å were removed, before resetting the energy and focusing values to the previous of step 5. In this case, another beam current density profile was acquired immediately after sputtering to confirm the beam profile. The ion gun operating points were found to be satisfactorily repeatable. Similarly and for ion energies at or above 500 eV, the data corresponding to the first 10 Å, *i.e.*, the first few monolayers, were ignored in the sputtering yield calculations, in order to ignore possible sputtering of surface impurities over the first monolayers.

Step 8 was performed to confirm that the observed erosion was solely due to the ion beam impingement and that sputtering was not competing with regenerative processes at the surface such as adsorption.

## 6.2 Sample Preparation and Properties

### 6.2.1 Preparation

The preparation of the molybdenum samples was determined by two sets of constraints. The first one was to ensure that the material properties relevant to sputtering would be reproduced in the samples, while the second one was related to the limitations specific to the QCM technique.

The first constraints were, understandably, dictated by the need to perform the measurements on material samples representative of the material on an actual ion engine grid electrode. This meant that the molybdenum samples should have material properties similar to the molybdenum used for the ion optics, at least for those properties likely to affect the sputtering yield: density and privileged directions, *e.g.*, crystalline versus amorphous structure. Possible steady-state, residual stresses in the molybdenum film were not believed to be likely to affect sputtering, unless they resulted in a problem of adhesion, because the surface remains stress-free and sputtering, even more so at low energy, is essentially a surface process.

Scanning Electron Microscope (SEM) micrographs were obtained on molybdenum engine grid bits, both from the surface at various locations in the erosion pattern, and from an edge. In the edge view shown in Fig. 6.9, the grid bit was broken in liquid nitrogen, to ensure a brittle fracture. The micrographs did not reveal any distinguishable microstructure. Rather, a laminar pattern with length scale  $\approx 1 \mu\text{m}$  was apparent, likely to be the result of the lamination in the manufacturing process of the molybdenum sheets used for the grids.

The second set of constraints resulted from the choice of the QCM technique to perform the measurements. Due to its extreme sensitivity to areal mass density ( $8.18 \times 10^7 \text{ Hz}\cdot\text{cm}^2/\text{g}$ ) and finite frequency range (6-5 MHz), only a limited amount of material can be used to load the surface of the quartz crystal. For a molybdenum film the maximum thickness to avoid damping the crystal oscillations is  $12 \mu\text{m}$ .

Two schemes were considered to prepare the samples. The first one was to bond a  $4\text{-}\mu\text{m}$  molybdenum foil on the crystal electrode, while the second method was sputter deposition.

The thin film bonding method disallowed the use of an epoxy-type glue, as the

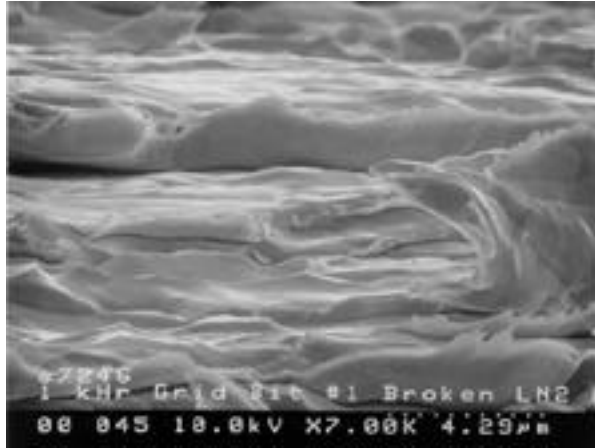


Figure 6.9: SEM micrograph of a molybdenum engine grid bit broken in liquid nitrogen, edge view. Magnification  $\times 7000$ .

bond line would have been excessively thick (greater than  $100\ \mu\text{m}$ ). Two samples were prepared using a cyano-acrylate glue with a bond line thickness of about  $1\ \mu\text{m}$ , and the shear wave speed, necessary to correct for the acoustic impedance of the glue in the QCM monitor, was measured to be about  $816\ \text{m/s}$  for a density of about  $1\ \text{g/cm}^3$ . The crystal oscillations, however, were observed to become erratic. Possible explanations are excessive dissipation of the oscillations in the bonding layer, bad adhesion under vacuum, or difficulties grounding the quartz crystal electrode supporting the sample. This first method, therefore, was deemed inappropriate. Sputter-deposition of molybdenum on the crystal oscillator was thus chosen as the method of choice.

The morphology of a metal coating deposited by sputtering is best described as a function of working pressure and temperature by a Thornton diagram [171, 172], as reproduced in Fig. 6.10. Bulklike properties can best be obtained when the structure is that of the zone T, or transition zone, consisting of a dense array of poorly defined fibrous grains [172], with a slightly compressive stress. As seen on the Thornton diagram, such a structure is obtained by sputtering preferably at a low pressure (of

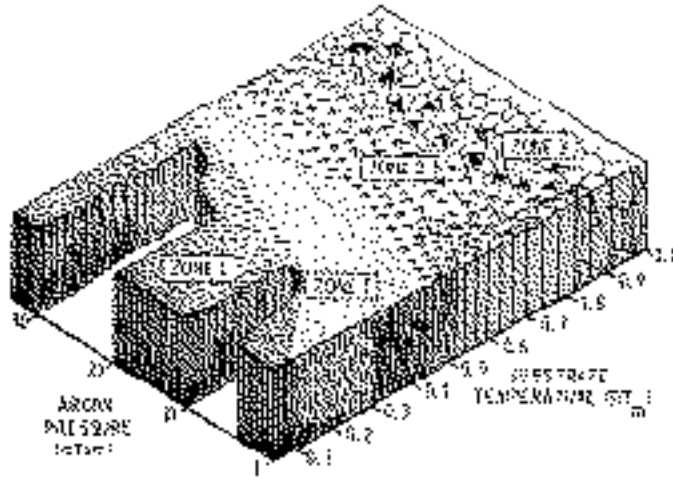


Figure 6.10: Thornton diagram: schematic representation of the influence of substrate temperature and argon working pressure on the structure of metal coatings deposited by sputtering using cylindrical magnetron sources.  $T$  is the substrate temperature and  $T_m$  is the melting temperature of the coating material. From Ref. [172], courtesy Academic Press.

the order of 0.1-1 Pa, or 1-10 mTorr) and intermediate temperatures a few tenths of a percent of the melting temperature  $T_m$  of the metal. Since planar diode sputtering typically requires pressures 10 to 100 times higher to achieve a satisfactory ionization efficiency, the low pressure requirement mandated the use of magnetron sputtering. The samples were deposited in the facility of Professor Nicolet, Division of Engineering and Applied Science, California Institute of Technology. Although it was impractical to heat the samples in the deposition chamber to enhance the mobility of the atoms in the sputter-deposited films, the samples could be biased negatively. This negative bias, while insufficient to induce significant implantation of working gas ions in the sample, had the effect of densifying the microstructure by forward sputtering, which facilitates filling the voids [173]. Table 6.1 summarizes the deposition parameters for the molybdenum samples used in this study.

Finally, the density of a thin film is usually a strong function of its thickness. In

Working gas	Argon
Working pressure	1.3 Pa (10 mTorr)
Process temperature	$\approx 100^\circ\text{C}$ (13% $T_m$ )
Bias voltage	-80 V
Deposition rate	670 Å/min

Table 6.1: Magnetron sputtering deposition parameters.

the case of aluminum for instance [174], the density increases sharply as the thickness of the deposited film increases, until  $\approx 500$  Å. Beyond this thickness, density keeps slowly increasing as a function of thickness, to reach 96% of the bulk density at 2000 Å (0.2  $\mu\text{m}$ ). Similar results have been reported for copper in Ref. [162], where the film density was shown to increase to within less than 3% of the bulk value by 2000 Å of film thickness. Problems of thermal expansion mismatch with the substrate can arise, however, for excessively large thicknesses. The molybdenum samples deposited on the gold electrode of the crystal resonator, in this study, had a thickness of 3  $\mu\text{m}$ . Additional samples were prepared with different thicknesses and bias voltage, for comparison, as well as different materials including titanium, tantalum and tungsten. Figure 6.11 shows the film structure obtained under different anode bias voltages, and Fig. 6.12 details the surface morphology.

### 6.2.2 Sample Density

Density is an important film property when studying surface sputtering. Shulga, in Ref. [127], showed that the sputtering yield for xenon ions on thirty different target materials is proportional to  $N^{p_s}$  (Eq. 4.22), where  $N$  is the atomic number density of the target material, and  $p_s \approx 0.5$  in the 200–600-eV range. We describe below four methods that were used to estimate the value of density for the films sputter-deposited on the quartz crystal electrode.

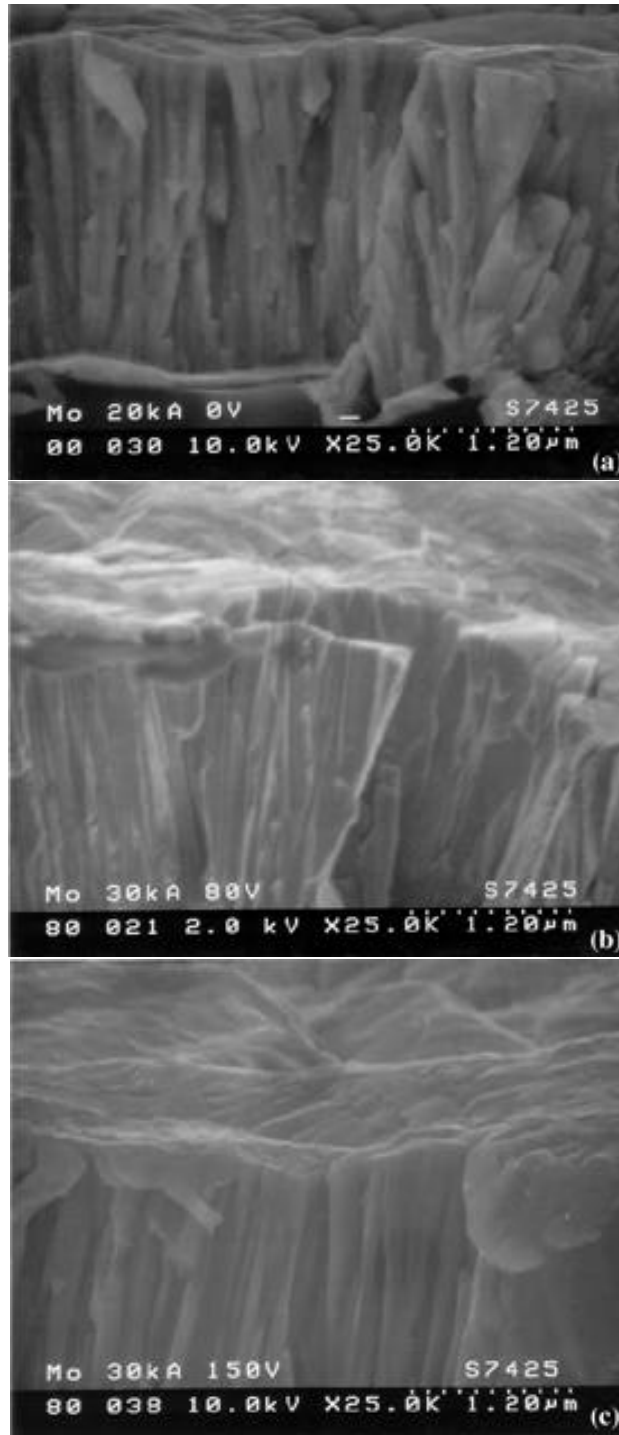


Figure 6.11: SEM micrographs of molybdenum films broken in liquid nitrogen, for different anode bias voltages during deposition. Magnification  $\times 25000$ . Thickness and bias voltage are, respectively: (a)  $20 \text{ k\AA}$ ,  $0 \text{ V}$ ; (b)  $30 \text{ k\AA}$ ,  $-80 \text{ V}$ ; and (c)  $30 \text{ k\AA}$ ,  $-150 \text{ V}$ .

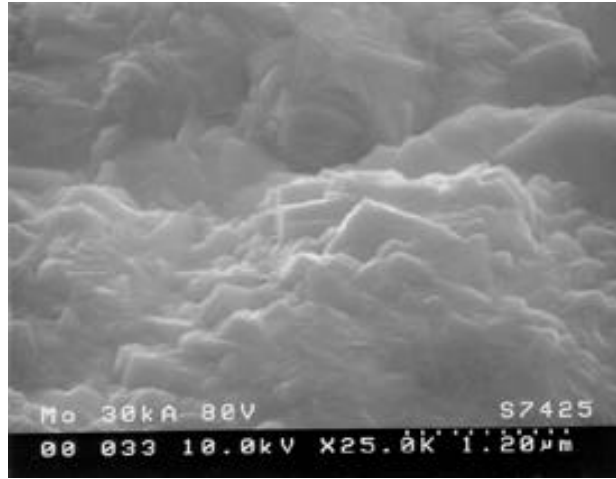


Figure 6.12: SEM micrograph of the surface of a 30-kÅ molybdenum film deposited with an anode bias voltage of -80 V. Magnification  $\times 25000$ .

A silicon substrate used as a witness plate was coated with molybdenum during each sputter-deposition. A mask was placed to cover a small fraction of their surface area so that the thickness of the deposited molybdenum film could be measured by means of a stylus profilometer, with the errors shown in Table 6.2.

In addition, a few molybdenum samples were deposited with thicknesses 2.5, 5, and 10 kÅ, a thickness range where Rutherford Backscattering Spectrometry (RBS) could be used to determine the sample density from the known thickness. A variation of this first method was to use the RBS data in conjunction with the RBS-simulation software Rump to obtain the density by curve-fitting, again from the known thickness.

The third method was to place the molybdenum-coated crystals with known thickness in the quartz crystal sensor and infer the density from the shift in crystal resonance frequency from the initial 6 MHz. This method was applied only to the 30-kÅ samples.

Finally, the mass difference of the crystals before and after deposition was also used to provide an estimate of the target densities. It should be noted that all four

Estimation method	Number of samples used	Known film properties used and associated error	Density [g/cm <sup>3</sup> ]
RBS	1	2.5 kÅ±4%	10.9±4%
	1	5.2 kÅ±5%	10.6±5%
	1	10.3 kÅ±2.5%	10.7±3%
RBS + Rump	1	2.5 kÅ±4%	10.8±4%
	1	5.2 kÅ±5%	10.2±5%
QCM	5 (80-V bias)	30 kÅ±3%	13.6±3%
	4 (150-V bias)	30 kÅ±3%	14.1±3%
Weight gain	6 (80-V bias)	30 kÅ±3%	10.7±13%
		4.95 mg±10%	
	4 (150-V bias)	30 kÅ±3%	13.5±11%
		6.22 mg±8%	

Table 6.2: Density estimates for the sputter-deposited molybdenum films.

methods relied on the knowledge of the thickness of the deposited films.

All four methods indicated a value slightly higher than the bulk density for molybdenum of 10.22 g/cm<sup>3</sup> [175], which is unrealistic. The density, however, was found to be at most within a few percent of the bulk density, except for the values calculated from the QCM frequency shift. This discrepancy could be explained by the fact that the films deposited in the zone T on a Thornton diagram (Fig. 6.10) harbor a slightly compressive stress, which does introduce a systematic error on an absolute thickness (or density) measurement with a QCM. Thickness change measurements, however, are not affected.

In conclusion, density is an important indicator of thin film morphology and is expected to affect surface sputtering. The samples were prepared under conditions that were chosen to give the molybdenum films a density very close to bulk density, which appeared to be confirmed experimentally. We note that the elemental information gained from the RBS spectra revealed a level of impurity limited to 0.1 to 0.2 percent (identified as tungsten), which was qualitatively confirmed with SEM

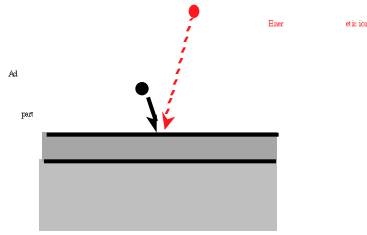


Figure 6.13: Regenerative vs. destructive processes for an adsorbate layer on a substrate.

elemental analysis.

### 6.2.3 Sample Surface Contamination

As noted earlier, surface contamination is a critical phenomenon for surface sputtering experiments. In order to guarantee accurate measurements, the sample surface should be free from adsorbed impurities or oxidation.

Yonts and Harrison [176] have discussed the competing processes involved in the building and destruction of the surface layer on a target bombarded by an ion beam in a vacuum system (Fig. 6.13). Their simplified analysis describes the sticking process by the equation

$$\frac{\partial n}{\partial t} = S_{a,s} \varphi_{g_a} - \varphi_d \quad (6.1)$$

where  $n$  is the surface layer density in atoms per unit area,  $t$  is time,  $\varphi_{g_a}$  is the number of gas atoms of species  $a$  striking a unit surface per second, and  $S_{a,s}$  is the corresponding sticking probability, such that  $S_{a,s} \varphi_{g_a}$  is the number of particles of adsorbate  $a$  sticking to a unit surface area of substrate  $s$  per second.  $\varphi_d$  is the number of atoms emitted per second from a unit surface area. The emission process considered here is ion-induced desorption, while thermal desorption is considered to be taken into account implicitly in the sticking probability. The evolution of the

surface layer with time is then, after integration, given by

$$n = n_0 \exp\left(-\frac{t}{\eta}\right) + S_{a,s} \eta \varphi_{g_a} \left[1 - \exp\left(-\frac{t}{\eta}\right)\right] \quad (6.2)$$

where the time constant  $\eta$  can be written as

$$\eta = \frac{e n_1}{J Y_{a,s}} \quad (6.3)$$

Here,  $n_0$  is the density of the initial surface layer, destroyed with time, and  $n_1$  is the surface density of the adsorbate for a complete monolayer.  $J$  is the ion beam current density,  $e$  the electronic charge and  $Y_{a,s}$  the sputtering yield of the emitted particles  $a$  when adsorbed on the substrate  $s$ . The equilibrium layer, or limit layer, can therefore be expressed as

$$n_\infty = S_{a,s} \eta \varphi_{g_a} \quad (6.4)$$

or

$$\frac{n_\infty}{n_1} = \left(\frac{S_{a,s}}{Y_{a,s}}\right) \left(\frac{e \varphi_{g_a}}{J}\right) \quad (6.5)$$

where we can define the ratio  $n_\infty/n_1$  as the limit fractional surface coverage  $\xi_\infty$ .

In the case of thermal background gas contamination,  $\varphi_{g_a}$  is given by the kinetic theory of gases and is proportional to  $P_a/(M_a T)^{1/2}$ , where  $P_a$  is the partial pressure and  $M_a$  the molecular mass of the gas species  $a$ , and  $T$  is the temperature. This result can be generalized for multiple species [82] by stating that

$$\xi_\infty = \sum_i \frac{S_{i,s} \varphi_{g_i}}{Y_{i,s} \varphi_b} \quad (6.6)$$

where  $S_{i,s}$  is the sticking probability of background gas species  $i$  on a clean target  $s$ ;

$Y_{i,s}$  is the sputtering yield of species  $i$  adsorbed on target  $s$ ;

$\varphi_{g_i}$  is the particle flux density of residual gas species  $i$ ; and

$\varphi_b$  is the beam particle flux density.

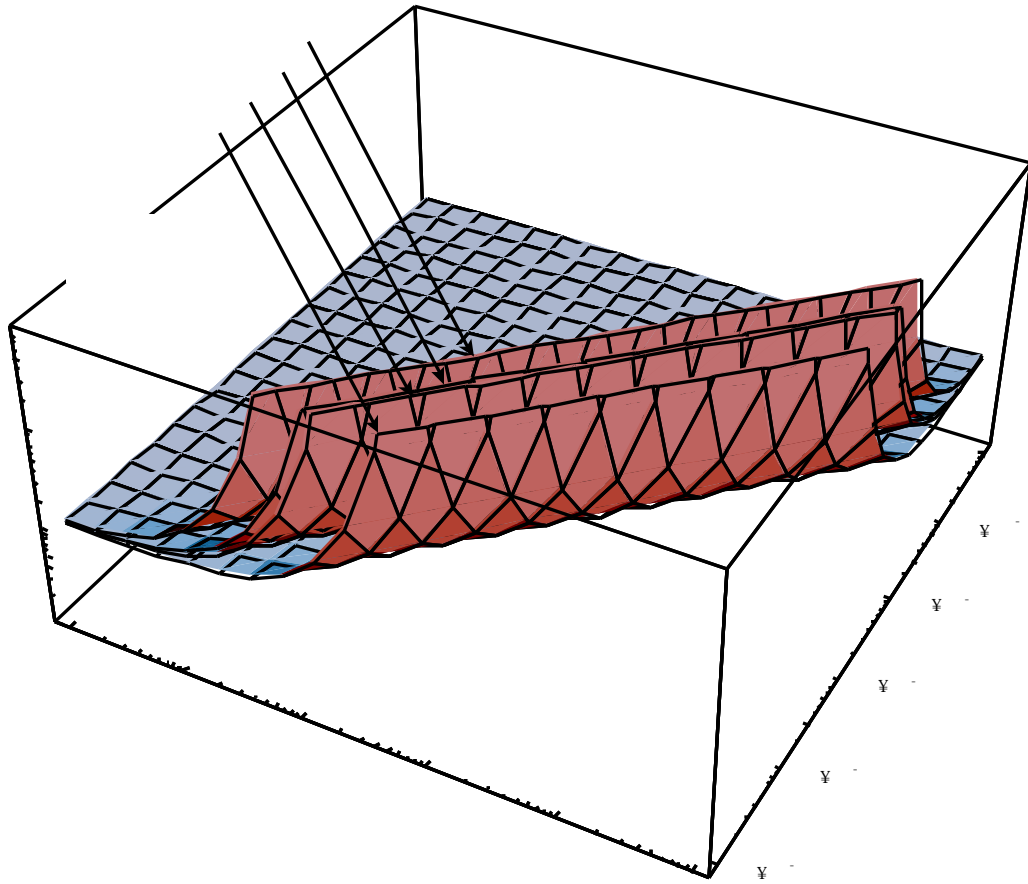


Figure 6.14: Beam-to-background gas particles flux ratio  $\varphi_b/\varphi_{g_i}$  at a surface at room temperature, for  $i=\text{Xe}$ ,  $\text{CO}$ ,  $\text{H}_2\text{O}$  and  $\text{H}_2$  as a function of pressure and ion beam current density.

Figure 6.14 illustrates the combined importance of the ion current density at the sample surface and the background gas pressure in surface contamination. The region of high beam current density and low residual gas pressure is the most favorable to maintain a clean sample surface, according to Eq. 6.6.

The balance between the regenerative effect of the system residual gas and the destructive effect of the beam appears directly in the ratio of  $\varphi_{g_i}$  to  $\varphi_b$ . The difficulty resides in the determination of the sticking probabilities  $S_{i,s}$  and the sputtering

yields  $Y_{i,s}$  of the particles making up the adsorbed or chemisorbed surface layer. In particular, in the limit of a coverage of about one monolayer, the sputtering yield of a species deposited on a target of a different material is in general different than the bulk sputtering yield for this species. For example, we will show in Chapter 7 that the sputtering yield of carbon on molybdenum with a coverage in the vicinity of one monolayer is significantly greater than the sputtering yield of bulk carbon.

The main gas species apart from xenon present in the chamber in the experiments described here were CO, Kr and CO<sub>2</sub> at a pressure near  $10^{-6}$  Pa ( $10^{-8}$  Torr), followed by H<sub>2</sub>, H<sub>2</sub>O, He and Ar at pressures in the high  $10^{-7}$ -Pa ( $10^{-9}$ -Torr) range. The effective average current density here was of the order of 1 mA/cm<sup>2</sup>, so that the ratio  $\varphi_b/\varphi_{g_i}$  was of the order of and slightly higher than unity. While the ratio of  $S_{i,s}$  to  $Y_{i,s}$  should be much smaller than unity for noble gases, it is expected that in particular CO, present in most ultra high vacuum systems, will have an important affinity for a clean molybdenum surface.

Experiments where Ion Scattering Spectroscopy (ISS) was performed on a clean molybdenum surface were conducted in another facility capable of base pressures in the mid- $10^{-8}$ -Pa ( $10^{-10}$ -Torr) range. The presence of oxygen at the surface was found to increase with a similar time constant (of order 30 minutes) at  $\sim 7 \times 10^{-8}$  Pa ( $5 \times 10^{-10}$  Torr) and  $3 \times 10^{-6}$  Pa ( $2 \times 10^{-8}$  Torr). It was found from mass spectrometry measurements that in both cases carbon monoxide was present with comparable partial pressures, *i.e.*, in greater relative quantities in the background gas for the lower pressure experiment.

This suggests that an initial, finite oxide layer might be extremely difficult to avoid, even when using more expensive pumping equipment. As shown in Eq. 6.5, however, the question of whether the surface is *dynamically* clean during the experi-

ment is determined more by the ratio of sticking-to-sputtering probability ( $S_{i,s}/Y_{i,s}$ ) and contaminant-to-ion flux density ( $\varphi_{g_i}/\varphi_b$ ) than by the initial layer. Chapter 7 will provide a case study of this phenomenon, with the example of carbon contamination.

### 6.3 Results and Discussion

We now present the results of the low energy sputtering yield measurements. A discussion of experimental error follows.

As mentioned in the description of the experimental procedure, the beam profile  $J(r)$  was obtained for each experiment and curve-fitted to a Gaussian curve, with general good agreement. This analytical form of  $J(r)$  was necessary to calculate the Current-Sensitivity Integral (CSI) discussed in Chapter 5. As an example, both data and Gaussian fits were shown in Fig. 6.6 for the beam current density profile across a 100-eV beam.

Similarly, a linear fit was performed on the thickness measurement  $\Delta\tau_{meas}$ , with the first 10 Å disregarded for sputter-cleaning, as explained earlier in the experimental procedures. Figure 6.15 shows the data and the fits for sputtering by 1-keV, 600-eV and 300-eV ion beams. We recall that, in the 300-eV case as in all cases below 400 eV, the sample was first sputter-cleaned at 1 keV, which results in the high initial etch rate over the first 10 Å. Using the CSI and the slope of the linear fit of  $\Delta\tau_{meas}$  versus time, the sputtering yield  $Y$  for the corresponding energy was then obtained using Eq. 5.16.

The recorded ion parameters, graphite mask current, sample current and sensor temperature were checked for stability. The measured sample current was the net current resulting from the collected beam current (between 200 and 50 nA), and

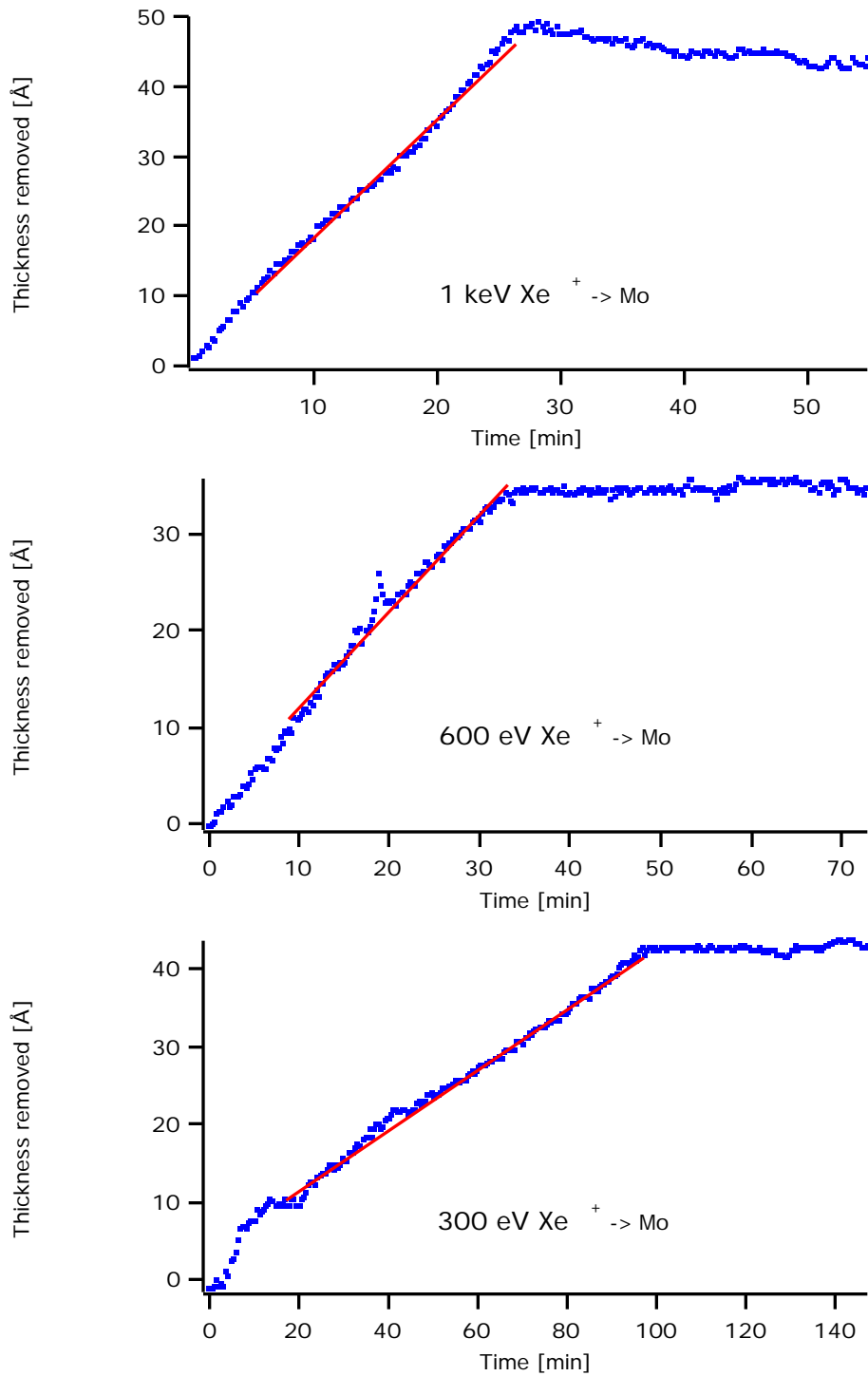


Figure 6.15: Time history of eroded thickness for 1-keV, 600-eV and 300-eV xenon ion bombardment on molybdenum. The dots represent the data points, and the solid line is the best linear fit over the corresponding time interval.

the secondary electron current. The expected secondary-electron emission current correction for xenon ions on molybdenum is 1% at 1 keV, and lower below 1 keV [177]. Because the Faraday cup was designed with a deep aspect ratio in order to limit the emission of secondary electrons out of the collector cup, no secondary electron current correction was applied to the Faraday cup current. Agreement between the integrated Faraday cup current over the mask aperture, and the collected sample current corrected for secondary electron emission, varied between  $\pm 10$ –20%.

Similarly, the current collected by the graphite mask was useful in checking the stability of the beam but did not agree with the corresponding integral of  $J(r)$ . This disagreement, however, was expected as the Gaussian fit was not in satisfactory agreement with the data at the corresponding radial positions (beyond  $\pm 4$  mm).

Due to the presence of the temperature control, there were no significant, large time-scale temperature change. Short time-scale thermal noise was kept within  $\pm 0.2^\circ\text{C}$  and was negligible.

A systematic, misalignment uncertainty of  $\pm 0.25$  mm was assumed and propagated in the calculation of the CSI. This misalignment uncertainty is based on the precision of the positioning system, and reflects the fact that the beam center position was found to occasionally vary by a comparable amount between experiments.

Finally, it was assumed that the film density was equal to the molybdenum bulk density with an uncertainty of  $+0/-5\%$ , based on the discussion in the previous section. This was propagated in the resulting sputtering yields through the  $N^{0.5}$  dependence reported by Shulga [127] in Eq. 4.22.

Table 6.3 presents a summary of the results where the calculated errors are indicated, based on the above discussion. The sample current is the integral of  $J(r)$  between  $\pm 4$  mm (the graphite mask aperture diameter) as measured by the Faraday

Energy eV	Sample current nA $\pm$ 10%	Mask current nA $\pm$ 10%	CSI nA/mm <sup>2</sup>	Sputtering yield atoms/ion
1000	202.4	8.0	19.06 $^{+0}_{-8}$ %	1.53 $^{+0.28}_{-0.19}$
900	140.1	7.9	12.10 $^{+0}_{-7}$ %	1.97 $^{+0.33}_{-0.25}$
800	268.3	4.9	30.80 $^{+0}_{-9}$ %	1.48 $^{+0.28}_{-0.19}$
700	142.0	16.9	12.14 $^{+0}_{-7}$ %	1.13 $^{+0.19}_{-0.14}$
600	186.8	14.9	19.20 $^{+0}_{-9}$ %	0.90 $^{+0.17}_{-0.11}$
500	119.0	32.4	10.24 $^{+0}_{-7}$ %	0.72 $^{+0.12}_{-0.09}$
400	119.9	31.9	10.60 $^{+0}_{-8}$ %	0.73 $^{+0.13}_{-0.09}$
300	122.9	20.1	13.26 $^{+0}_{-9}$ %	0.50 $^{+0.10}_{-0.06}$
250	90.0	39.4	7.62 $^{+0}_{-7}$ %	0.22 $^{+0.04}_{-0.03}$
200	83.7	39.2	7.09 $^{+0}_{-8}$ %	0.13 $^{+0.02}_{-0.02}$
100	50.1	41.8	3.41 $^{+0}_{-7}$ %	0.08 $^{+0.01}_{-0.01}$

Table 6.3: Summary of results for sputtering experiments with xenon ions on molybdenum.

cup. The assumed uncertainty of  $\pm 10\%$  is driven by the observed current fluctuations due to pressure changes in the ion source. The mask current is the current collected by the graphite shield, and is not used in the data processing. Finally, the error on the CSI shown only includes the effect of the misalignment uncertainty. A misalignment between the sample and the beam could only cause a reduced effective CSI. As seen in Table 6.3, the effect of focusing on the effective average current density (CSI) and corresponding (misalignment) error is emphasized in the experiment at 800 eV (high focusing) and the experiment at 900 eV (low focusing).

It can be seen from the comparisons between sample current and mask current that focusing of the beam was increasingly difficult at low energy. This is briefly discussed in Appendix A.

Energy (eV)	Ref. [136]	Ref. [111]	Ref. [137]	Ref. [138]	Present study
1000	1.6				$1.53^{+0.28}_{-0.19}$
900	1.42				$1.97^{+0.33}_{-0.25}$
800	1.24				$1.48^{+0.28}_{-0.19}$
750				$0.799\pm 0.183$	
700	1.06				$1.13^{+0.19}_{-0.14}$
600	0.88	1.06	0.78		$0.90^{+0.17}_{-0.11}$
500	0.69		0.70	$0.648\pm 0.149$	$0.72^{+0.12}_{-0.09}$
400	0.6	0.7	0.65		$0.73^{+0.13}_{-0.09}$
300	0.4	0.51	0.60		$0.50^{+0.10}_{-0.06}$
250				$0.241\pm 0.027$	$0.22^{+0.04}_{-0.03}$
200	0.2	0.28	0.30		$0.13^{+0.02}_{-0.02}$
150			0.09	$0.161\pm 0.02$	
100	0.023	0.06			$0.08^{+0.01}_{-0.01}$

Table 6.4: Sputtering yield of xenon on molybdenum, comparison with other data from published literature.

## 6.4 Conclusions

The QCM technique was found to offer a resolution that enables consistent detection of the removal of less than an atomic monolayer of molybdenum at the surface of a 3- $\mu\text{m}$  molybdenum sample. The samples were deposited on a piezoelectric quartz crystal electrode by magnetron sputtering with an anode bias of -80 V in order to obtain a density considered to be within 5% of the bulk density. Table 6.4 compares the results obtained in this study with previously published data in this energy range.

The results presented here are found to be in satisfactory agreement with previously published data, so that the author feels confident that the method can be extended to other metallic materials, including tantalum, tungsten and titanium, and ion kinetic energies closer to the energy threshold for sputtering by xenon-ion

bombardment. The remaining issues to be addressed in the future are primarily:

- improve the vacuum chamber base pressure and evaluate the sticking coefficients and ion-induced desorption cross-sections for contaminants, particularly if the measurements are to be extended to the threshold region, where the beam current density will be further reduced; and
- improve the differential pumping setup and pressure control in the source region of the ion gun to reduce the variability in beam current.

If such issues can be resolved in the future, this method should enable measurements of sputtering yields as low as  $10^{-4}$  atoms/ion, thus significantly extending the energy range over which experimental sputtering yields are available.

# Chapter 7

## The Effect of Carbon Deposition in Ground-Based Operations

As discussed in Chapter 2, long-duration ground testing of ion engines is an important—and costly—part of the effort to demonstrate and evaluate ion engine lifetimes. Some erosion mechanisms, however, can *a priori* be greatly affected by effects specific to the ground testing environment. Backflow contamination of the thruster surfaces by atoms sputtered from the beam target in ground facilities is one such effect, and the purpose of this chapter is to provide a quantitative assessment of its influence on engine lifetime.

### 7.1 Accelerator Grid Erosion by Charge-Exchange Ions During Ion Engine Ground Testing

Inelastic, two-body collisions between gaseous atoms can result in charge-transfer (also called electron-capture) processes. They can be either symmetric resonant (when

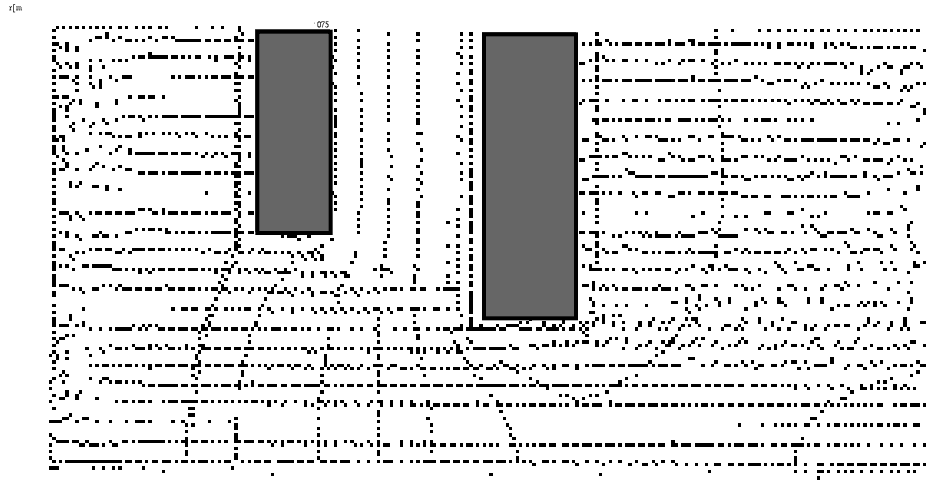


Figure 7.1: Electrostatic potential contours and ion trajectories in an individual ion optics aperture, courtesy J. Wang, JPL. This plot is similar to the ion current density vectors on Fig. 2.3, but the vector lengths have been normalized on this plot to clarify the trajectories.

the collision involves two atoms of the same species, *i.e.*, when the initial and final systems are identical) or asymmetric nonresonant (when the collision involves atoms of different species) [178, 179]. In the special case of a resonant symmetric charge-exchange collision between a fast (accelerated) ion and a slow (thermal) neutral, a slow-ion fast-neutral pair will be produced.

Figure 7.1 shows the electrostatic potential contours and ion trajectories through an individual hole in the ion optics, for the NSTAR ion engine at nominal operating conditions. The charge-exchange, thermal ions produced within the potential well in the vicinity of the accelerator grid (see also Fig. 2.3) are unable to escape this potential well, and are seen to be accelerated back toward that electrode. This can potentially lead to the failure modes 1–3 identified in Chapter 2 as associated with accelerator grid erosion.

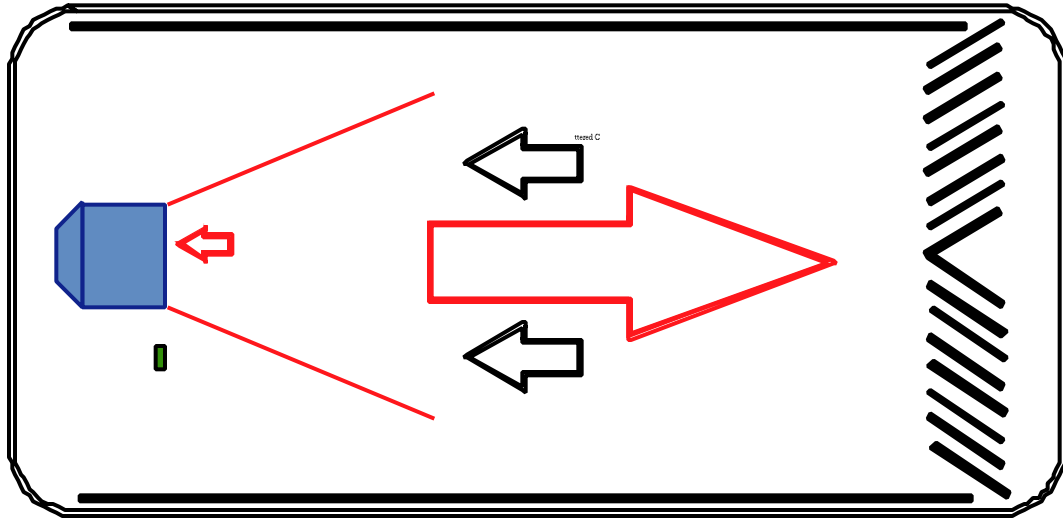


Figure 7.2: Schematic diagram of the NSTAR ground testing facility, and particle flows to and from the engine during thruster operation. The high-velocity ion beam is stopped by graphite panels to protect the stainless steel chamber walls, which causes carbon atoms to be backspattered on the engine. Simultaneously, the downstream side of the accelerator grid is subject to erosion by charge-exchange ions.

Because total cross-sections for electron capture are a function of projectile energy, the charge-exchange ion production rate is a function of ion velocity, as well as beam ion density and neutral atom density. The neutral gas density in the vicinity of the ion optics is dictated, in space-based operations, by the finite leak rate of neutral propellant atoms out of the discharge chamber through the grid structure. This is due to non-ideal propellant ionization efficiency. In ground tests, however, the background gas density in the vacuum chamber can be a contributor to the charge-exchange ion production rate. It can, in fact, affect the grid erosion in many ways because of the different neutral flow field [42] and ion production location.

Another effect specific to ground-based operations is the backflow contamination from sputtered beam target atoms, as illustrated in Fig. 7.2. The simultaneous erosion of the downstream side of the accelerator grid and deposition of carbon atoms

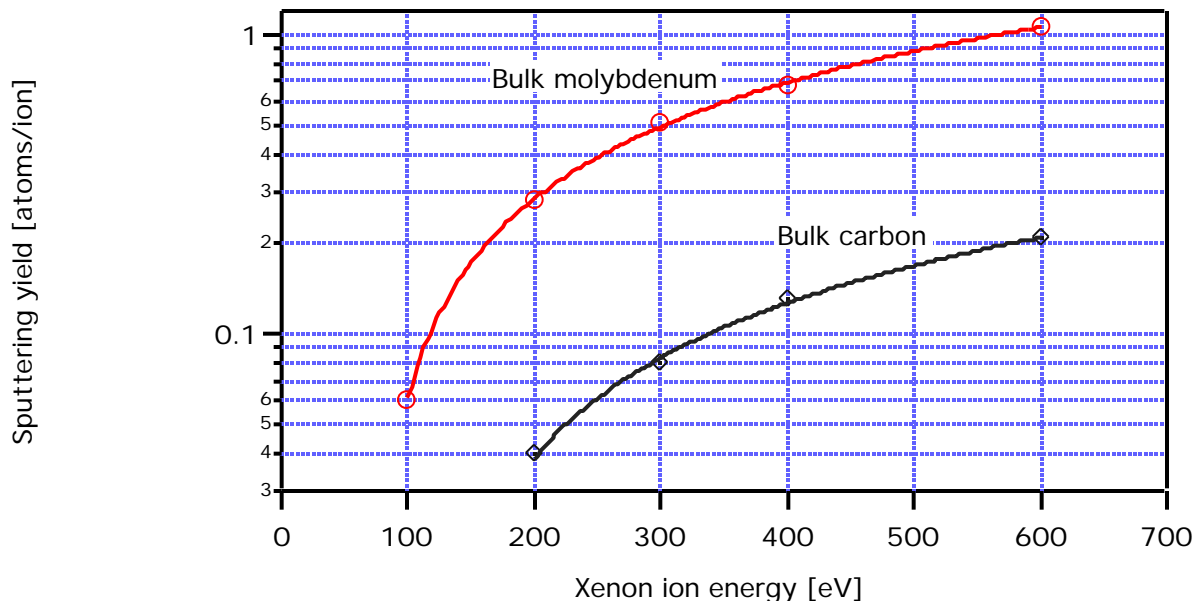


Figure 7.3: Sputtering yields for xenon on bulk molybdenum and carbon. Data from Rosenberg and Wehner [111].

sputtered from the beam target leads to the dynamic situation described in Chapter 6, Eq. 6.6, and is the subject of this chapter.

The sputtering yield of bulk<sup>1</sup> carbon is approximately an order of magnitude lower than the sputtering yield of bulk molybdenum, as seen in Fig. 7.3. This is the reason why graphite panels are used to protect the stainless steel walls of the vacuum chamber. The concern, however, is whether the deposited carbon on the downstream side of the molybdenum accelerator grid protects that electrode, thus rendering the conclusions of ground-based engine endurance testing questionable.

This concern is made clearer upon inspection of both the optical pictures (Fig. 7.4) and the SEM elemental images (Fig. 7.5) taken after completion of the 8200-hour Life

---

<sup>1</sup>Sputtering is fundamentally a surface process, but here we use the word “bulk” to distinguish a sample thick relative to the ion range in this material, from a film of thickness smaller than, or comparable to, the ion range.

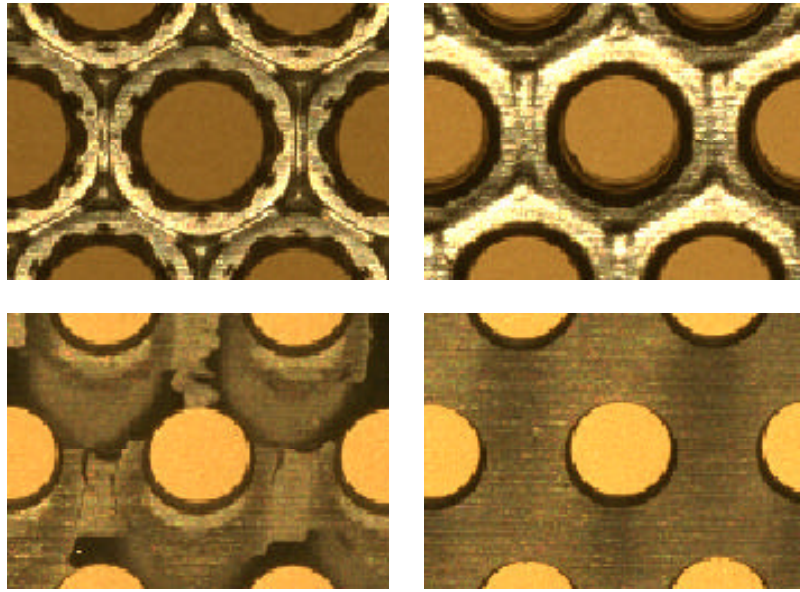


Figure 7.4: Optical photographs showing the deposition and erosion patterns on the downstream side of the accelerator grid [35].

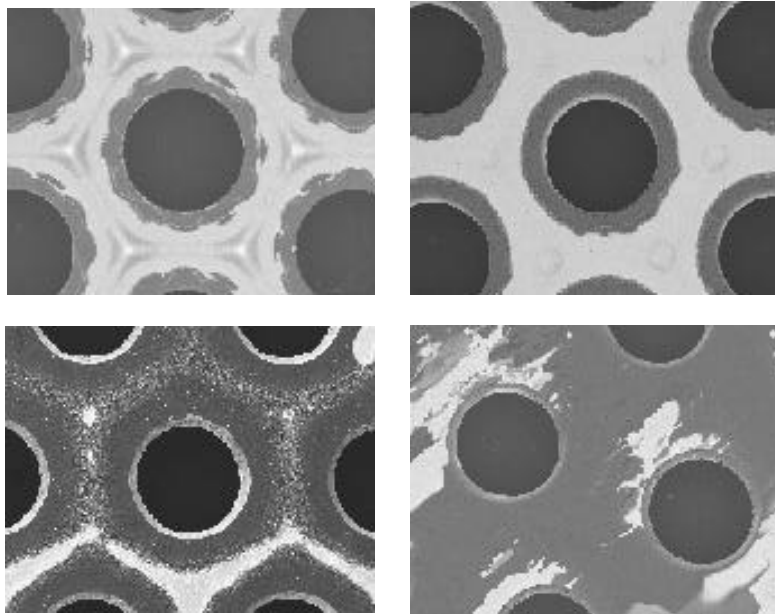


Figure 7.5: SEM images with elemental resolution showing the deposition and erosion pattern on the downstream side of the accelerator grid. White areas are predominantly molybdenum and dark regions are carbon deposits [35].

Demonstration Test (LDT) at JPL. The optical and SEM images shown here were taken at four different radial positions on the downstream side of the accelerator grid, as indicated ( $r = 0$  is the centerline). The post-test grid hole diameter varies from  $\approx 1.4$  mm along the centerline to  $\approx 1.1$  mm (practically the pre-test value) in the outer region of 30-cm diameter grid [55]. The optical pictures show a gradual attenuation of the pits and groove erosion pattern around the holes as the radial position increases, while the SEM images emphasize the gradual increase in carbon coverage (indicated by the dark areas). This behavior is caused by a gradual decrease in ion current density from approximately  $35 \mu\text{A}/\text{cm}^2$  near the centerline, to  $2 \mu\text{A}/\text{cm}^2$  at  $r = 14$  cm. The distribution of engine beam current density versus radial position is shown in Ref. [35].

Perhaps the most striking feature seen on the SEM images is the length scale over which the transition from net erosion to net deposition takes place on the accelerator grid (Fig. 7.5c). At this radial position ( $r = 11.8\text{cm}$ ), the beam current density  $J_b$  is approximately  $10 \mu\text{A}/\text{cm}^2$ . However, the question remains of whether the erosion rates, critical near the engine centerline, are reduced by the backspattered carbon. It was addressed by both an analytical approach and an experimental approach, as discussed below.

## 7.2 Surface Kinetics Model

In the case of simultaneous surface erosion and deposition by a dominant contaminant species, we established the result in Eq. 6.5 which we rewrite below, using the subscripts  $C$  for the carbon contaminant, and  $Mo$  for the substrate:

$$\xi_C = \left( \frac{S_{C,Mo}}{Y_{C,Mo}} \right) \left( \frac{e \varphi_C}{J} \right)$$

where  $\xi_C$  denotes the steady-state carbon fractional coverage,  $S_{C,Mo}$  is the sticking probability of carbon on molybdenum,  $Y_{C,Mo}$  is the sputtering yield of carbon adsorbed on molybdenum,  $\varphi_C$  is the incoming carbon atom flux density, and  $J/e$  is the beam ion flux density.

If we assume that the net molybdenum sputtering yield is decreased by an amount proportional to the carbon coverage, *i.e.*, if

$$Y_{Mo}^{net} = Y_{Mo} (1 - \xi_C) \quad (7.1)$$

where  $Y_{Mo}$  is the sputtering yield of bulk molybdenum, and if we assume further that the sticking probability  $S_{C,Mo}$  of carbon on a clean molybdenum surface is close to unity, then the reduction in molybdenum sputtering due to the carbon film at a given radial position  $r$  on the accelerator grid is given by the ratio

$$\frac{Y_{Mo}^{net}}{Y_{Mo}} = 1 - \left( \frac{e \varphi_C}{J(r) Y_{Mo}} \right) \left( \frac{Y_{Mo}}{Y_{C,Mo}} \right) \quad (7.2)$$

In this expression,  $J(r)$  is known [35], as well as  $Y_{Mo}$  (above 100 eV). The quantity  $\varphi_C$  is given by the QCM deposition monitor shown in Fig. 7.2 and was found to be relatively constant during testing, at a value  $\varphi_C \approx 2.19 \times 10^{12}$  atoms/cm<sup>2</sup>·s [35, 55]. The reduction in sputtering yield, therefore, requires knowledge of the ratio  $Y_{Mo}/Y_{C,Mo}$ , *i.e.*, the ratio of bulk molybdenum sputtering yield to that of a thin carbon film on molybdenum.

### 7.3 Desorption Cross-Section Model

Technically, it is considered that sputtering is a phenomenon that is observable on target materials of homogeneous composition. This criterion is what separates sputtering from collision-induced desorption [82]. Because we are concerned here with the

ion-induced removal of carbon surface atoms with coverage in the monolayer range on bulk molybdenum, and in keeping with this convention, we will often refer to desorption cross-sections as opposed to sputtering yields in the remainder of this chapter. It should be understood, however, that the two physical quantities are closely related, as shown below:

$$\begin{aligned}
 Y &= n_1 \sigma_d \\
 &= n \sigma_{d_1}
 \end{aligned}
 \tag{7.3}$$

where  $n$  is the surface atomic number density, in  $\text{cm}^{-2}$ , and  $\sigma_d$  is the ion-induced desorption cross-section, in  $\text{cm}^2$ . The subscript 1 refers to a coverage of unity, *i.e.*,  $n = n_1$  for a complete monolayer. Thus, we have expressed the fact that the probability of desorbing an atom is proportional to the surface coverage  $\xi = n/n_1$  for a given desorption mechanism.

This section presents a brief description of a model implemented by Polk *et al.* [35] for a theoretical treatment of the desorption cross-sections. In a similar fashion to our treatment of sputtering of homogeneous targets in Chapter 3 (Fig. 3.2), we start by distinguishing three distinct mechanisms of desorption by knock-on collisions [82]: direct knock-on by incoming ions; knock-on by reflected ions; and knock-on by sputtered substrate atoms, as shown in Fig. 7.6.

The collision processes involved in the three mechanisms can be modeled as two-body scattering events [180, 181] using the power potential approximation proposed by Lindhard [88] and described in Chapter 3. The Winters-Sigmund theory assumes that the total desorption cross-section  $\sigma_d$  is given by the sum of the cross-sections for the three interactions shown in Fig. 7.6, and expressed as follows [180, 181].

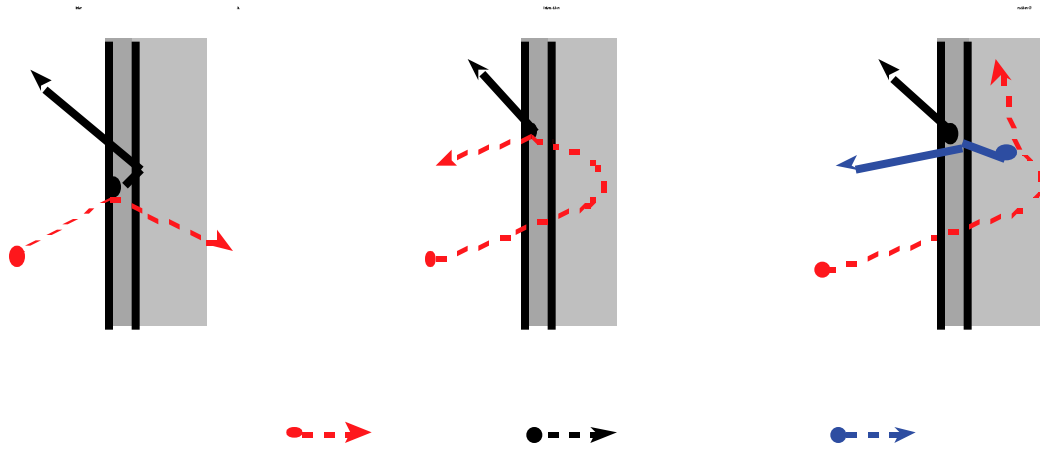


Figure 7.6: Mechanisms of ion-induced desorption, *e.g.*, carbon adsorbate on a molybdenum substrate.

The cross-section for interaction A is given by

$$\begin{aligned}\sigma_A &= \frac{1}{\cos \vartheta} \int_{E'}^{\gamma E} d\sigma(E, E') \\ &= \frac{1}{\cos \vartheta} \frac{C_m}{m} (E U_b)^{-m} (1 - x^{-m})\end{aligned}\quad (7.4)$$

with the notations used in Chapter 3, where  $\gamma$  is given by Eq. 3.3,  $d\sigma$  by Eq. 3.10, and  $C_m$  by Eq. 3.11. In the expression for  $\sigma_A$ , the quantities  $d\sigma$ ,  $\gamma$ ,  $m$  and  $C_m$  are all calculated for the ion (xenon) as the projectile, and for the adsorbate (carbon) as the target element. Consequently, the surface binding energy is that of carbon on molybdenum. The parameter  $x$  is equal to  $\gamma E/U_b$ , and the energy  $E'$  is the average minimum energy that the carbon atom must be given to escape under this mechanism.

In the case of interaction B, the cross-section is calculated from

$$\sigma_B = \sigma_A R_{12} \left( 4 - \frac{4 \ln x}{3(x^{1/3} - 1)} \right) \cos \vartheta \quad (7.5)$$

where  $R_{12}$  is the reflection coefficient for the ion at the substrate surface and is a strong function of the mass ratio  $M_1/M_2$ .

Finally, the contribution from interaction C is given by

$$\sigma_C = 4\gamma C_m \frac{U_{b_{Mo}}}{U_{b_C}} Y_{Mo} \frac{1 - [(1 + \ln y/y)]}{(1 - \gamma/y)^2} \quad (7.6)$$

where  $U_{b_{Mo}}$  and  $U_{b_C}$  are the surface binding energy of molybdenum, and carbon on molybdenum, respectively. In this expression, the energy transfer coefficient  $\gamma$  is calculated for the outbound molybdenum atom as the projectile, and carbon as the target. The parameter  $m$  is set equal to zero, consistent with very low energy interactions. The parameter  $y$  is the product of the two energy transfer coefficients for xenon on molybdenum, and molybdenum on carbon, times the ratio  $E/U_{b_C}$ .

The expressions described above were used to calculate the ion-induced desorption cross-sections of argon and xenon for a thin carbon film on molybdenum. The results for the total desorption cross-sections are discussed later, along with the experimental results.

## 7.4 Experimental Measurements of Carbon Desorption Cross-Sections

In this section, we describe the apparatus and experimental method implemented to measure ion-induced desorption cross-sections for xenon ions on a thin carbon film deposited on molybdenum. The experiments described in this section were performed at the Department of Chemistry, University of Southern California.

### 7.4.1 Surface Diagnostics and Ion Scattering Spectroscopy

The measurement of the ion-induced desorption cross-sections of carbon on molybdenum was performed in a static experiment, *i.e.*, with no flux of incoming carbon

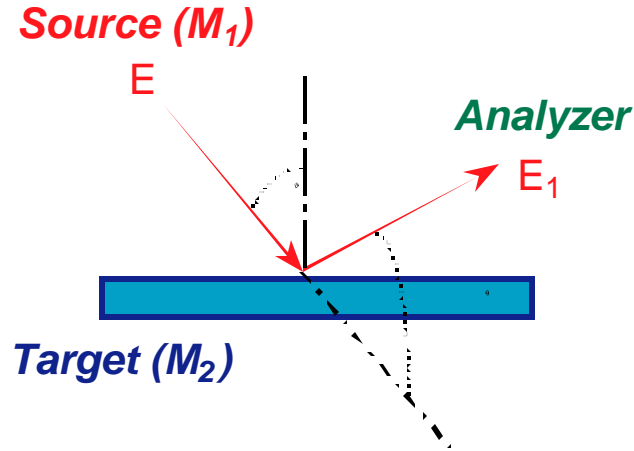


Figure 7.7: Principle of Ion Scattering Spectroscopy (ISS).  $E$  is the energy of the incident ion, and  $E_1$  is the energy of the backscattered ion. The ratio  $E_1/E$  is a measure of the mass ratio  $M_1/M_2$ .

atoms during the ion bombardment. *In-situ*, controlled deposition of carbon in the monolayer-range was achieved on an atomically clean Mo(100) single crystal surface before bombarding the sample with an energetic ion beam. Appropriate surface diagnostics were then used to determine carbon surface coverage as a function of bombarding ion fluence.

Among the variety of popular quantitative surface analysis techniques, Ion Scattering Spectroscopy (ISS) has the unique particularity of being extremely sensitive to the first atomic layer [182, 183] and was therefore chosen to monitor the carbon coverage on the molybdenum substrate. As shown in Fig. 7.7, the incoming ions produced and accelerated by the ion source are scattered by the surface atoms and collected in an electrostatic energy analyzer.

The energy ratio  $E_1/E$  is given by [184]

$$\frac{E_1}{E} = \left( \frac{\cos \theta + \sqrt{(M_2/M_1)^2 - \sin^2 \theta}}{1 + M_2/M_1} \right)^2 \quad (7.7)$$

As shown in Fig. 7.8, the scattering angle  $\theta$  is fixed and determined by the relative

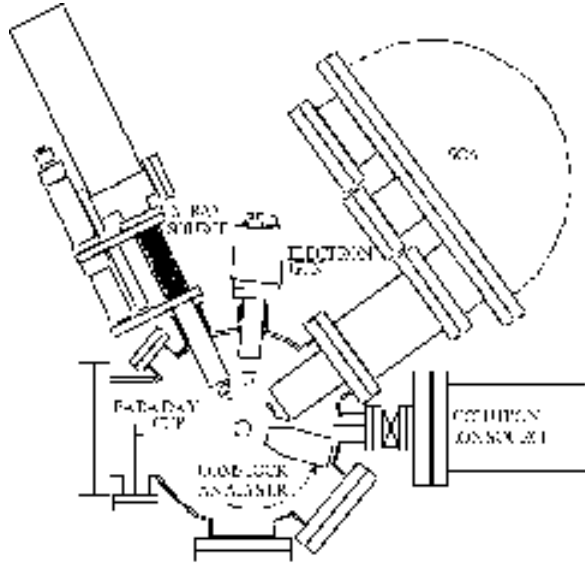


Figure 7.8: Diagnostics setup in the ultra high vacuum facility used to measure the ion-induced desorption cross-sections.

alignment between the ion source and the Spherical Capacitor Analyzer (SCA). The ratio  $E_1/E$  is then only a function of the mass ratio between the incoming ions and the scattering centers at the surface. The peaks in collected current over the energy range scanned by the analyzer correspond to the different atomic masses of atoms present in the top monolayer.

We are primarily interested in the desorption induced by normally-incident ions, so the incidence angle  $\vartheta$  had to be zero degrees. This condition of normal incidence could not allow operation of ISS in forward-scattering mode, and the heavier atomic mass of xenon compared to both carbon and molybdenum also made back-scattering ISS impossible. It was therefore necessary to use a mixture of a lighter gas (argon) and xenon to allow simultaneous desorption by xenon ions and back-scattering ISS using the argon beam.

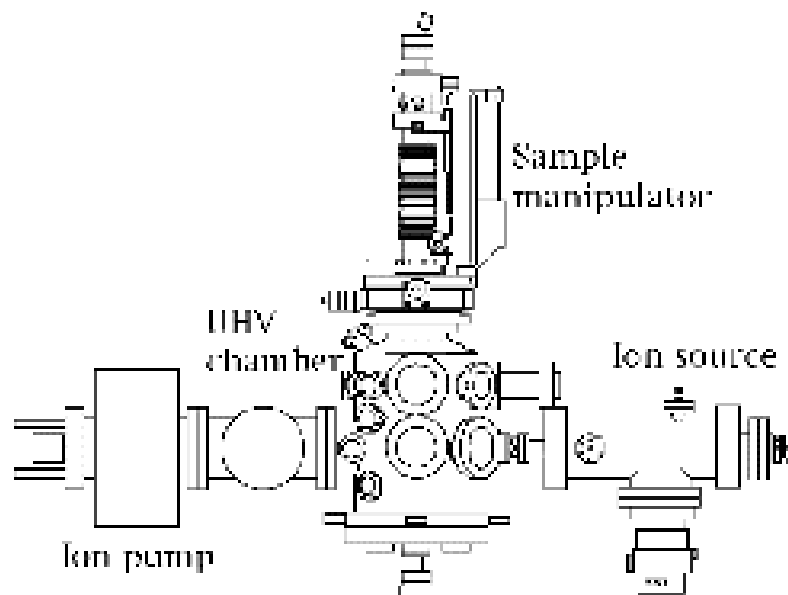


Figure 7.9: Ultra high vacuum facility used to measure the ion-induced desorption cross-section.

#### 7.4.2 Apparatus and Sample Preparation

The experiments were carried out in a ultra high vacuum system at the Department of Chemistry, University of Southern California. The base pressure was  $10^{-8}$  Pa ( $10^{-10}$  Torr) and the system, represented in Figs. 7.8 and 7.9, contained a differentially pumped Colutron 10-kV ion gun, and a Perkin-Elmer Model 10-360 Spherical Capacitor Analyzer (SCA) at a fixed 144-degree scattering angle, usable for ISS and X-ray Photoelectron Spectroscopy (XPS). Other capabilities included in the chamber are Auger Electron Spectroscopy (AES) and Low Energy Electron Diffraction (LEED).

Because the Colutron ion gun could not produce a stable ion beam at energies less than about 400 eV, it was not possible to obtain data at the energies expected for the charge exchange ions incident on the downstream surface of the accelerator

grid. Measurements were made for energies ranging from 400 to 1000 eV, and the behavior at lower energies was obtained qualitatively using the theoretical model.

The Mo(100) sample (Atomergic Chemetals Corp.) was a 10-mm diameter  $\times$  1.5-mm thick single crystal cut within  $\pm 0.5$  deg. The crystal was held on the sample holder between two 0.4-mm tungsten wires used to resistively heat the sample. Temperatures were measured by a thermocouple junction spot-welded to the edge of the crystal.

At the indicated base pressure, the monolayer formation time for oxygen appeared to be on the order of an hour, while it was expected to be  $\approx 30$  hours for carbon-containing species [185]. Overnight, a surface layer containing carbon and oxygen would build up to yield an Auger Peak to Peak Height (APPH) ratio of typically 40% for C/Mo and 50% for O/Mo at the beginning of the next day.

In order to perform the initial cleaning of the surface, the sample was first submitted to an oxygen treatment at an oxygen partial pressure of  $1.3 \times 10^{-5}$  Pa ( $1 \times 10^{-7}$  Torr) at 800 K, for 2 minutes. The oxygen treatment removed the carbon surface layer by forming CO, which then evaporated. A new AES analysis typically yielded an APPH ratio close to 0% for C/Mo and 100% for O/Mo after this step. The next step was to flash-heat the sample at 1700 K to drive off the surface oxygen. The APPH ratio at this point was usually about 20% for C/Mo and 0% for O/Mo. The presence of new traces of carbon at the surface was due to carbon diffusion from the bulk during the brief annealing. If more carbon were present, the cycle was repeated in order to lower the bulk concentration of carbon.

A controlled carbon monolayer was then grown on the sample surface by dosing 20 Langmuir ( $10^{-7}$  Torr  $\times$  200 seconds) of ethylene ( $C_2H_4$ ) at the sample surface at 850 K. This was performed to thermally crack the hydrocarbon and desorb hydrogen from

the surface, leaving behind carbon adatoms [186,187]. This method has been reported to deposit a saturated p(1×1) carbon monolayer on the molybdenum surface for a C/Mo APPH ratio of  $0.36\pm 0.01$  [187]. The annealing temperature was a trade-off between a temperature high enough to carburize the surface, while avoiding carbon diffusion into the bulk. The sharp p(1×1) LEED pattern obtained was in accordance with the literature, but the C/Mo APPH ratio was close to 32%, except on two occasions when it was observed to be as high as 43% and 50%.

### 7.4.3 Experimental Procedure

When a uniform ion beam with current density  $J$  impinges on a sample surface, the decrease  $dn_a/dt$  of the surface atomic number density of the adsorbate with time is given by [188, 189]

$$-\frac{dn_a}{dt} = \frac{J}{e} \sigma_d n_a(t) \quad (7.8)$$

where  $\sigma_d$  is the desorption cross-section. Under the assumption that the intensity of the ion scattering signal is proportional to the surface density of the scattering centers, we have

$$I_a(t) = C_a n_a(t) \quad (7.9)$$

where  $C_a$  mostly depends on the scattering cross-section and the neutralization probability for the incident ion. The decrease in ISS signal for the adsorbate with increasing ion fluence is therefore described by

$$I_a(t) = C \exp\left(-\frac{J}{e} \sigma_d t\right) \quad (7.10)$$

where  $C$  is a constant. Since argon ions are not backscattered by carbon adatoms, however, the rise of the substrate signal can be monitored instead and we have equiv-

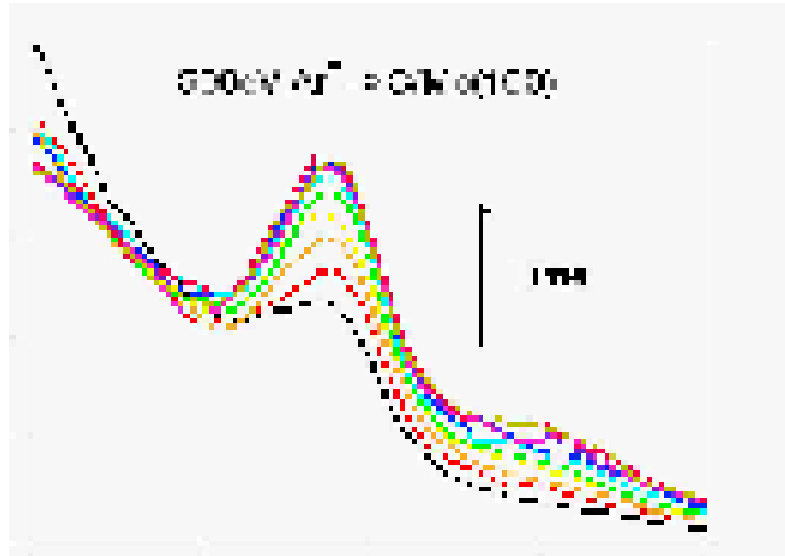


Figure 7.10: Molybdenum ISS peak vs. time for 500-eV argon ion-induced desorption of carbon on a molybdenum single crystal. The time scale between curves is 2 min.

alently [188]:

$$I_s(t) = I_s(\infty) + C \exp\left(-\frac{J}{e} \sigma_d t\right) \quad (7.11)$$

where  $I_s(t)$  is the signal intensity for the substrate atoms.

By monitoring the rise in the ISS substrate signal with time, or rather ion fluence, it is then a matter of fitting this exponential form to the data and repeating the experiment for different values of incident ion energy to obtain the energy dependence of the desorption cross-sections. An example of the rise of the molybdenum (substrate) ISS signal with time is given for the case of carbon desorption by 500-eV argon ions in Fig. 7.10.

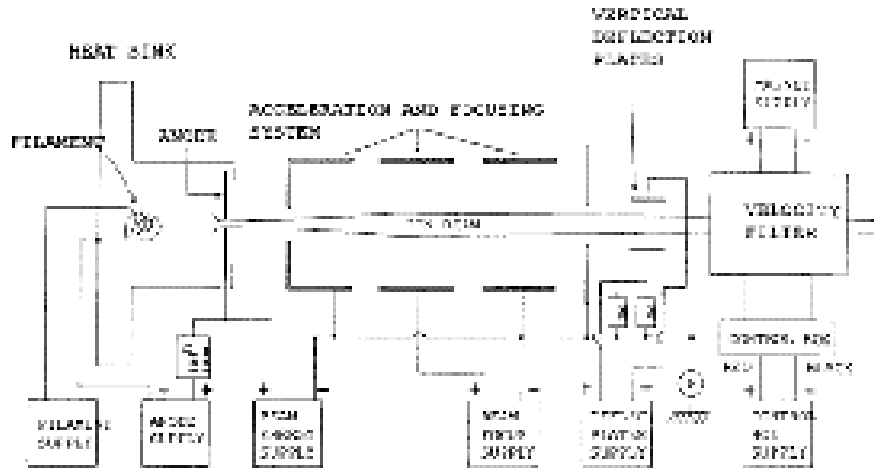


Figure 7.11: Ion source used in the ion-induced desorption experiments.

#### 7.4.4 Results

Three data points each were obtained for the desorption of carbon on molybdenum by argon and neon. In both cases, the gas was introduced pure in the ion source. In addition, nine points were obtained for desorption by xenon, at five different energies. In the case of xenon-ion induced desorption, however, and as discussed earlier, a 2/1 mixture of argon and xenon was used. An  $E \times B$  velocity filter shown in Fig. 7.11 downstream of the ion optics was used to select the xenon ion beam to desorb the carbon layer, or the argon ion beam to perform the ISS diagnostics at regular time intervals.

The downstream aperture of the ion gun was  $2 \text{ mm}^2$  in size, and the beam parameters including focusing were adjusted so as to optimize the beam current on a fixed Faraday cup placed downstream of the sample. An important discrepancy, usually a factor of 3 to 5, was found between the beam density as measured by the Faraday cup, and the beam density as inferred by the sample current. This was believed to be caused by a slight misalignment of the Faraday cup and the beam, possibly due to

imprecise positioning of the Faraday cup or beam deflection by the ion optics. The beam current density was therefore inferred from the sample current, with the ion gun assumed to generate a well collimated, uniform beam with a spot size of  $2 \text{ mm}^2$  (1.6-mm diameter). This assumption is supported by the fact that an ion beam of this diameter with a current density of  $2 \text{ nA/mm}^2$ , typical in the experiments described here, assumed fully non-neutralized and with an energy of 400 eV (worst case) would have a divergence angle due to its own space charge smaller than 0.01 degree (Appendix A).

Another correction was brought to the data acquired for molybdenum to account for the desorption induced by the argon beam during the ISS diagnostics. The argon cross-sections were used along with an initial guess of the xenon cross-sections to calculate an equivalent xenon ion fluence accumulated on the analysis area by the argon ion beam during the approximately 1-minute long ISS scan. After several iterations a ratio of 7 between the xenon cross-sections and the argon cross-sections was found to be satisfactorily self-consistent. Because the argon current was generally lower than the xenon current, and because the argon cross-sections are lower than those for xenon, this correction proved to be rather minor and of the order of a few percent, except on one occasion when the argon current was noticeably larger than the xenon current (correction of 20% for the higher value of the xenon ion desorption cross-section at 500 eV).

The ISS signal used was the integrated area under the molybdenum peak, expressed in relative, arbitrary units and scaled with the sample current to correct for small variations of the incident ion beam current density over time. Example plots of the ISS signal versus ion fluence along with the corresponding exponential fit are shown in Fig. 7.12. The experimental cross-sections obtained here are summarized in

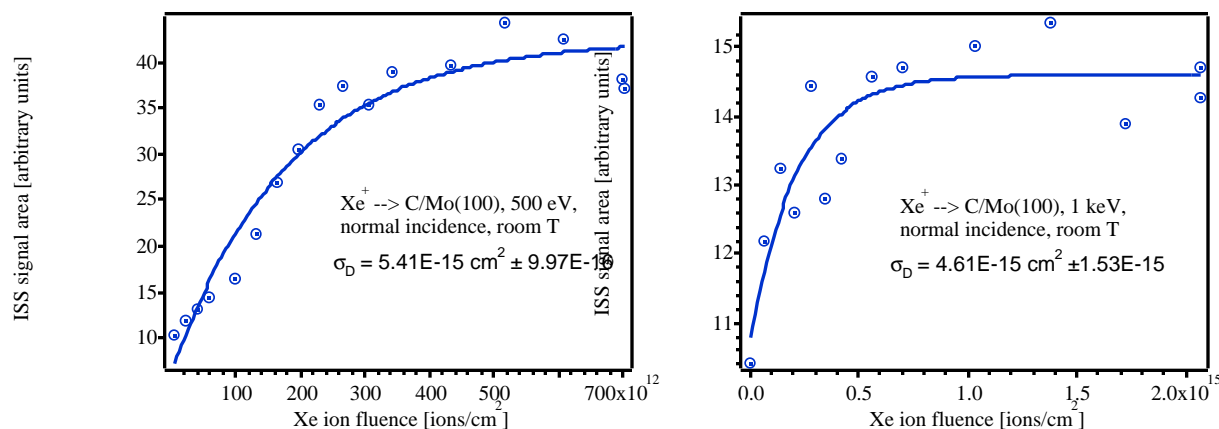


Figure 7.12: ISS signal area for molybdenum vs. xenon ion fluence. Bombardment at 500 eV (left) and 1 keV (right).

Table 7.1.

The rather large spread in the data has been noted by other authors, and may be attributed to particle prebombardment and changes in surface roughness [185, 189, 190]. In addition, small variations in the level of carburization of the surface could cause an overlayer of carbon adatoms with smaller binding energy to form, possibly changing the measured desorption cross-section.

It is particularly interesting to notice that in the two cases where consecutive experiments were performed on different regions of the sample without a new surface preparation, the measured desorption cross-sections were remarkably consistent, *e.g.*, xenon cross-sections of  $1.25 \times 10^{-14}$  at 1 keV and  $1.36 \times 10^{-14}$  at 750 eV for a given surface preparation, and xenon cross-sections of  $4.61 \times 10^{-15}$  at 1 keV and  $5.41 \times 10^{-15}$  at 500 eV for another. Overall, the data seemed to agree in range with the published literature [191] for argon and neon, while it was noticeably higher for xenon. Few cross-sections for xenon, however, are available for comparison.

Energy (eV)	Ions		
	Xenon	Argon	Neon
400	$3.34 \times 10^{-15} \pm 31\%$		
	$1.22 \times 10^{-15} \pm 192\%$		
500	$1.01 \times 10^{-15} \pm 20\%$	$5.08 \times 10^{-16} \pm 17\%$	$1.65 \times 10^{-16} \pm 10\%$
	$5.41 \times 10^{-15} \pm 18\%$		
600	$1.79 \times 10^{-16} \pm 39\%$		
750	$1.36 \times 10^{-14} \pm 35\%$		
	$4.9 \times 10^{-15} \pm 37\%$		
1000	$1.25 \times 10^{-14} \pm 117\%$	$5.05 \times 10^{-16} \pm 36\%$	$2.65 \times 10^{-16} \pm 11\%$
	$4.61 \times 10^{-15} \pm 33\%$	$1.27 \times 10^{-16} \pm 11\%$	$2.73 \times 10^{-16} \pm 12\%$

Table 7.1: Summary of experimental ion-induced desorption cross-section measurements. Cross-sections are in  $\text{cm}^2$ .

## 7.5 Discussion

The calculated desorption cross-sections for xenon and argon are plotted in Fig. 7.13 assuming two different values for the carbon binding energy  $U_{b_C}$ . A value of 6 eV for  $U_{b_C}$  and 10 eV for  $E'$  yields results which agree very well with the argon data, but underpredict the xenon cross-sections. A value of 2 eV for  $U_{b_C}$  and 3 eV for  $E'$  matches the lower values of the xenon measurements at low energies, but still significantly underpredicts the results at higher energies. A binding energy of 2 eV or less is unrealistic for a chemisorbed adatom. If the true value were this low, thermal desorption would be significant and it would be difficult to accumulate carbon on the hot grid. It is more likely that some model assumptions fail for this case.

Comparison of the Winters-Sigmund model with measured cross-sections for a large number of ion-target combinations reveals that it often underpredicts the measured values for heavy ions [192]. The cross-sections for the direct knockoff and reflected ion contributions decrease slightly with increasing energy, while the sputtered atom contribution rises with increasing energy. The trend in the xenon data

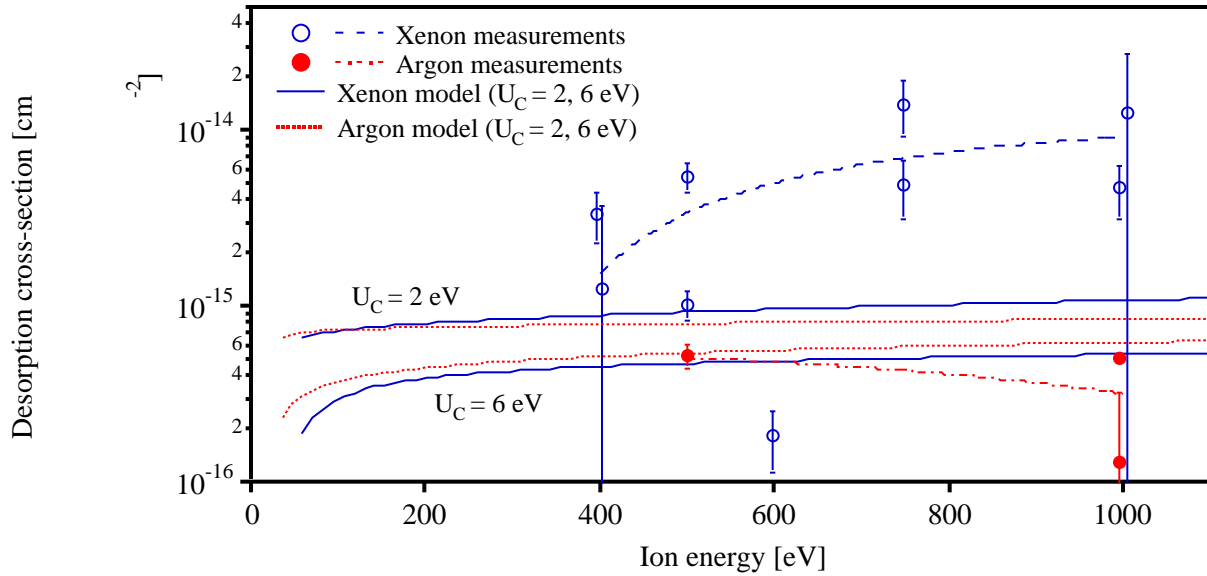


Figure 7.13: Measured and calculated cross-sections for ion-induced desorption of carbon from molybdenum by xenon and argon ions [35].

suggests that the desorption of carbon by sputtered atoms plays an important role, as has been observed in other heavy ion experiments [192]. The use of binary collision approximations and most existing collision potentials for sputtering calculations at low energies and high ion mass is questionable [95], so there may be considerable error in this component of the calculated cross-sections. In addition, the calculated reflection coefficients for xenon incident on molybdenum are very low (on the order of  $10^{-3}$ ), so  $\sigma_B$  is negligible. Errors in the reflection coefficient could also contribute to the underprediction.

## 7.6 Conclusions

The surface kinetics model discussed earlier (Eq. 7.2) can be used, along with the relationship in Eq. 7.3, to evaluate the attenuation in the sputtering yield of molyb-

denum due to carbon deposition in the sub-monolayer range. The lowest measured values for  $\sigma_d$  with xenon are of the order of  $1 \times 10^{-15} \text{ cm}^2$ . The surface density  $n_1$  for a complete monolayer—a p(1×1) layer—is given by the density of adsorption sites at the surface of the molybdenum single crystal, *i.e.*,  $N^{2/3}$  where  $N$  is the atomic number density of molybdenum, in atoms/cm<sup>3</sup>. Using a value for  $n_1$  of  $1.1 \times 10^{15} \text{ cm}^{-2}$  [35], and a sputtering yield of 0.295 for xenon on molybdenum at 200 eV, the ratio  $Y_{Mo}/Y_{C,Mo}$  has the value 0.27.

The theoretical results show qualitatively that the cross-sections do not vary much with energy down to about 50 eV. The theoretical cross-sections for reasonable values of the carbon binding energy are somewhat lower—on the order of  $4 \times 10^{-16} \text{ cm}^2$ , which corresponds to a yield of 0.44 atoms/ion and a ratio  $Y_{Mo}/Y_{C,Mo}$  of 0.67. These values and the measured carbon deposition rate were used to calculate the reduction in molybdenum sputtering yield, which is plotted as a function of ion impingement current density in Fig. 7.14.

The average impingement current density in the center of the grid and at a radius of 11.8 cm—the boundary between net deposition and net sputtering—is shown as vertical lines on the plot. These data show that the effect of carbon deposition on ion engine grid wear rates is less than 5% in the center of the grids, where the ion impingement current density is high. The measured values of the carbon sputtering yield and the estimated ion impingement current density at a radius of 11.8 cm on the grid suggest that the reduction in the molybdenum sputter yield is only about 5–15% in that location also, while the deposition pattern indicates that the molybdenum sputtering yield is reduced to zero at this point. As shown in Fig. 7.14, a sputtering yield ratio of  $Y_{Mo}/Y_{C,Mo} = 8$  is required to prevent molybdenum sputtering at a current density of  $10 \text{ } \mu\text{A}/\text{cm}^2$ . This corresponds to an ion-induced desorption cross-

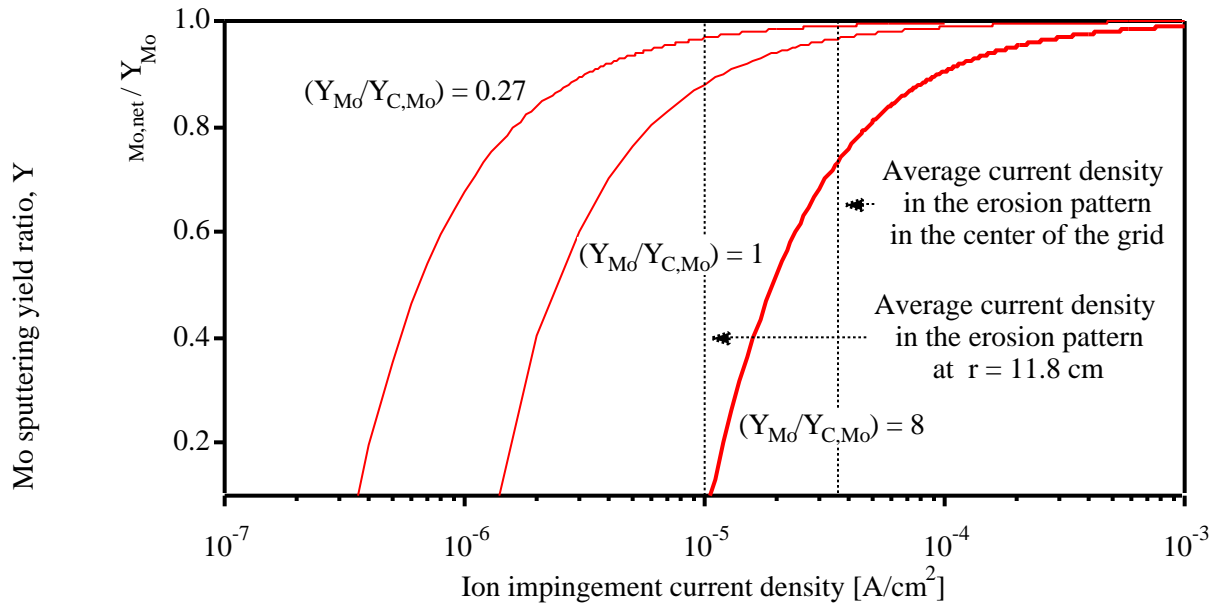


Figure 7.14: Attenuation of molybdenum sputtering yield due to carbon deposition vs. ion impingement current density [35].

section of  $3.4 \times 10^{-17} \text{ cm}^2$ , which is 2 orders of magnitude lower than the measured cross-sections. A more likely explanation is that the ion current density or energy is overestimated at this location. Computational modeling of the ion flow field and energy distributions in the vicinity of the grids is an ongoing effort in the NSTAR program, and should contribute to lower the uncertainties on the effect of carbon deposition.

However, even with these uncertainties, it appears that the impingement current density and the carbon sputter yields are sufficiently high to prevent the accumulation of carbon in the erosion pattern in the center of the grids. This is an important result because the wear in the center of the grid determines the grid lifetime. The erosion rates measured in the long duration tests can therefore be used with confidence in predicting engine wear in space.

# Chapter 8

## Conclusions

### 8.1 Summary of Major Results

Quantitative analysis of physical sputtering at energies in the eV region poses unique challenges. Considering the interest generated by this field and the effort devoted by the scientific community, it may seem that surprisingly little progress has been made since the early sixties.

On the analytical and computational side, the difficulties reside both in the choice of an appropriate description of the colliding atoms, and in realistic modeling of the interaction mechanisms. To begin with, collisional energy transfers have multiple sources and mechanisms, elastic or inelastic. They involve the electronic distribution of the atoms, and have a complex nature where direct electron-electron collisions, and excitation or ionization of the colliding atoms may come into play. In addition, modeling of atomic binding forces at a real surface is also a source of extreme difficulty. Obviously, sputtering is a discipline that mixes solid state, atomic, molecular, chemical, and surface physics, as well as materials science.

Upon reviewing current analytical methods with over seventeen distinct approaches and variations, we have concluded that only one, the Wilhelm theory, appears to have a sound physical justification below 100 eV. Unfortunately, it is still of relatively limited use because of the uncertainties associated with the parameters that describe it, so that the uncertainty has only been shifted from the model used to describe the sputtering mechanisms, to the determination of the parameters of a more reliable model. We have proposed, in Chapter 4, a practical approach to its implementation based on a simple calculation of total scattering cross-section under the approximation  $m = 0$  in the Lindhard differential cross-section. Unfortunately, an estimate for the sputtering threshold energy, a somewhat controversial and subjective quantity, is also needed. Again, we have proposed a model for quantitative estimates of sputtering thresholds. This model, however, has both the merit of incorporating inelastic energy losses and returning values (Table 4.1) that appear in reasonable agreement with what little experimental data is available for comparison (Table 3.2), and the worrisome limitation that it assumes binary collisions, a notion that the Wilhelm theory is precisely avoiding.

Because we used a value of 28 eV for the threshold energy, which was calculated using a 1/4 LS potential model for the inelastic loss, and which is close to the lower value of 27 eV in the range of proposed threshold energies for xenon on molybdenum, and because the form of the Thomas-Fermi potential used resulted in higher sputtering yields than the hard-core approximation to the Born-Mayer potential, the proposed implementation of the Wilhelm theory is on the conservative side. The fact that the form proposed in Chapter 4 fits the data by Rosenberg and Wehner [111] at 100 eV is actually a surprising result, since in the examples used by Wilhelm [75] for sputtering by mercury ions, the predictions from his theory seemed to agree with

experimental data within 30–40 eV from threshold at most. This might be due to the contribution of the quantum-statistical coefficient  $h_{2/1}$  in the Wilhelm formula (Eq. 4.23), assumed equal to unity, to the overall uncertainty. Yet, because the hard-core radius in the Born-Mayer potential for xenon ions in molybdenum varies from 1.32 Å at 100 eV to 1.59 Å at 28 eV and since the mean interatomic distance in molybdenum is approximately 2.5 Å, the binary collision approximation is expected to start breaking down in the vicinity of 100 eV. Clearly, however, the need is still there to bridge the gap in the experimental data below 100 eV.

Computational Monte-Carlo simulations were used, in Chapter 4, in an attempt to extend sputtering yield values in the energy region below 100 eV. The TRIM code, based on the binary collision approximation, uses a random impact parameter to solve the collision orbit using the ZBL potential, an interatomic potential shown to be adapted to low energy collisions, *i.e.*, “down to  $\sim 300$  eV” [115]. Between calculated collisions, the code applies complex, averaged electronic and nuclear energy losses over the path length of the projectile. Again, the relatively good agreement between the Wilhelm (3-body) theory and the TRIM (binary collision) model is a surprising result, since we noted that multibody collisions should start being important below 100 eV. TRIM computations were also used to demonstrate that, although the relative sensitivity of sputtering to surface binding energy is dramatically increased at energies near threshold, and although the surface binding energy is a (weak) function of temperature, the low-energy sputtering yields are not expected to be increased by more than 1–2% at temperatures relevant to ion engine operations.

On the experimental side, a relatively inexpensive QCM technique described in Chapter 5 was implemented in a novel way that could allow measurements of sputtering yields as low as  $10^{-5}$  atoms/ion with the limited beam current densities of the

order of  $1 \mu\text{A}/\text{cm}^2$  available from the ion gun. Unfortunately, although the method was demonstrated over the energy range 1 keV–100 eV, it has failed yet to deliver reliable measurements below 100 eV, which was the initial goal. It is the author’s belief that no fundamental limit has been reached, however, and that additional efforts should finally yield results below 100 eV in the very near future, should this work be pursued. A number of difficulties could be resolved with the use of the new equipment soon to be available for this facility—a more stable ion beam current density due to appropriate differential pumping of the ion gun and improved control of the xenon pressure in the source (one of the leading factors in the uncertainty and variability of the data), and improved base pressure with the addition of an ultra high vacuum capable pumping setup.

The analytical, computational and experimental sputtering results described in this dissertation for xenon on molybdenum are summarized in Figs. 8.1 and 8.2. Figure 8.1 is similar to Fig. 4.3, but it includes the additional experimental results obtained in Chapter 6. Figure 8.2 details the analytical and computational results obtained in Chapter 4, for energies below 100 eV. The error bars for the Wilhelm theory include the uncertainties listed in Table 4.2, as well as an uncertainty corresponding to a factor of  $\pm 2$  on the coefficient  $h_{2/1}$ .

To complete the review of the results presented in this dissertation, we showed in Chapter 7 that although the agreement between the experimental ion-induced desorption cross-sections obtained with Ion Scattering Spectroscopy (ISS) and the model implemented by Polk *et al.* [35] is not very good, both the experimental data and the model suggested that the effect of carbon deposition on accelerator grid wear rates in ion engine ground testing was minimal. This is an extremely important result, for it allows the erosion data gathered during expensive and long-duration ( $\sim 10000$

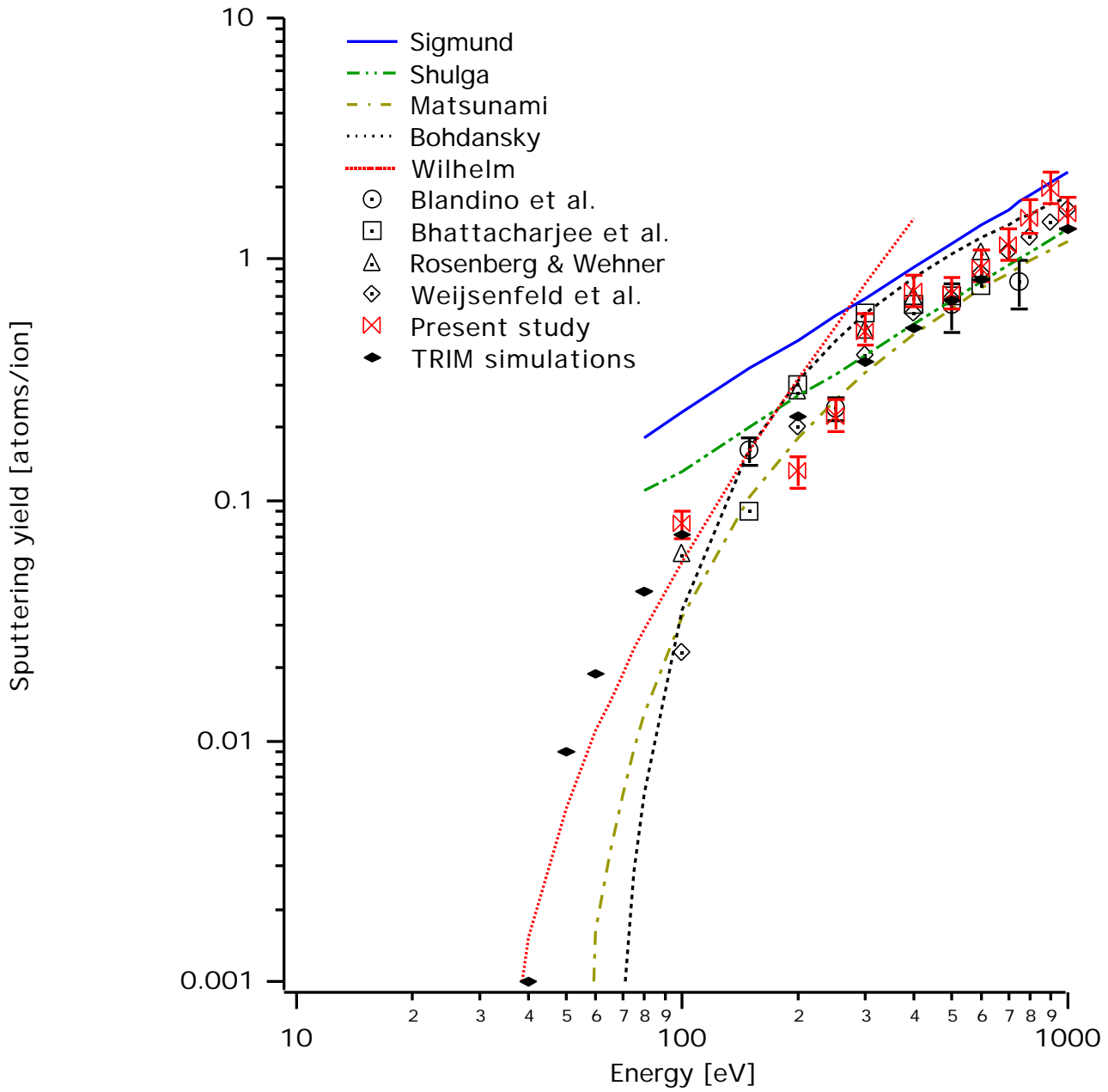


Figure 8.1: Analytical formulae, computer simulations, previous experimental data, and results of the present study for the energy dependence of the sputtering yield of molybdenum by xenon ions. The previous experimental data are from Weijsenfeld *et al.* [136], Rohsenberg and Wehner [111], Bhattacharjee *et al.* [137], and Blandino *et al.* [138].

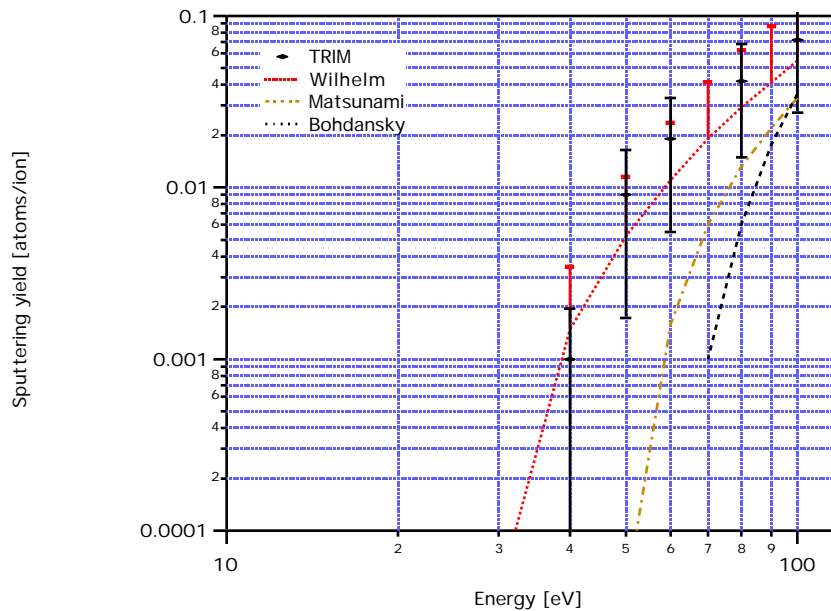


Figure 8.2: Analytical formulae and computer simulations for the energy dependence of the sputtering yield of molybdenum by xenon ions below 100 eV. The negative error bars on the Wilhelm formula are not shown for clarity.

hours) testing campaigns to be applied to the prediction of engine lifetime and failure risks in space.

## 8.2 Future Work

A significant goal of this project—providing experimental yield data below 100 eV and thereby contributing to significantly reduce the uncertainty on the yield parameter in the probabilistic failure models—has not been reached. It is the author’s belief, however, that these important results can be obtained with the facility and apparatus built along the course of this project, with the addition of newly available equipment. A number of issues remain, however, and should be addressed in the future.

Erratic response of the QCM to ion bombardment was occasionally observed. A

possible explanation could be that this was caused by local heating by the ion beam, resulting in a transient radial temperature gradient that triggered the high surface-stress sensitivity of the quartz crystal resonant frequency. To address this, a higher sample temperature might help to avoid frequency instabilities due to surface stresses induced by thermal transients generated by a sudden application of ion bombardment. Another solution could be to use the relatively recent SC-cut (stress compensated) crystals for which the resonant frequencies have been found to be less sensitive to thermal shock and mechanical stress [162]. Hayderer *et al.* [160] recently published sputtering yield measurements for He<sup>+</sup>-, N<sup>+</sup>- and Cu<sup>+</sup>-ions on LiF at energies down to 100 eV, using an SC-cut QCM. This method, however, is made more complex by the fact that in contrast to AT-cut crystals, the doubly-rotated SC-cut crystals have two shear modes of oscillation. Because the important benefit provided by the use of the differential mass sensitivity described in Chapter 5 might be lost when using SC-cut crystals, it is not clear whether such crystals would provide a decisive benefit. Because the occasional erratic response was not systematic and did not appear to be correlated to beam voltage or density, a more likely cause of this behavior was perhaps a deteriorated adhesion of the film on the crystal electrode after repeated vacuum chamber bakeouts. This could be caused by the coefficient of thermal expansion mismatch between the quartz and the sample material.

More importantly, the issue of surface contamination at low bombarding ion densities is still critical. As seen in Chapter 7, self-cleaning of the target surface during low-density irradiation cannot be achieved, and “a contamination-free surface has to be maintained by means of ultra high vacuum conditions” [193]. There seems to be some disagreement over the oxide layer formation time scales on clean molybdenum under high vacuum conditions [34,35,194,195]. Because low-energy sputtering experi-

ments will typically take tens of hours, however, it does not appear that an oxide-free surface can be maintained in such an experiment, regardless of the initial surface cleanliness, as evidenced by Eq. 6.4. A solution would be, therefore, to perform a study similar to the one described in Chapter 7, where the desorption cross-section of *chemisorbed* contaminants such as oxygen under xenon bombardment would be evaluated to assess the effect of a finite oxygen coverage of the sample.

On a different note, and as for the probabilistic failure analyses, the variability on the engine dependent parameters and on analytic failure models input parameters could possibly be reduced by applying the Taguchi method of robust engineering to the choice of values for the independent parameters necessary to achieve a desired engine throttle level. The Taguchi approach to the design of experiments has already been used in the NSTAR program to calculate engine parameter sensitivities [37], and it could be taken one step further.

### 8.3 Outlook

To paraphrase a famous quote in the history of space exploration, ion engine technology has taken a giant leap forward with the decisive flight validation of the NSTAR thruster aboard the interplanetary spacecraft *Deep Space 1*. Because the NSTAR technology was voluntarily conservative while yet offering spectacular benefits on comet rendezvous or sample return, Mars, and a variety of other outer planet missions, because improvements in total engine impulse capability provide a considerable leverage on mission performance, and finally because there exist candidate technologies with the promise of allowing significant engine lifetime improvements, the prospects for dramatically more ambitious space exploration missions now appear extremely

favorable.

# Appendix A

## Divergence of a Non-Neutralized Beam

The divergence angle for a non-neutralized beam of particles carrying a charge  $q$  and streaming at velocity  $\mathbf{v}$  is the result of the action of the outward electric force  $q\mathbf{E}$ , where  $\mathbf{E}$  is the local electrostatic field induced by the space-charge, and the inward force  $q\mathbf{v} \times \mathbf{B}$  produced by the azimuthal magnetic field  $\mathbf{B}$ . The net (radial) force is then given by (see for example Ref. [196])

$$qE - qvB = \left( \frac{qI_b}{2\pi\epsilon_0 Rv} \right) (1 - \epsilon_0\mu_0v^2) \quad (\text{A.1})$$

where  $I_b$  the total beam current,  $\epsilon_0$  and  $\mu_0$  are respectively the permittivity and permeability of vacuum, and  $R$  is the beam radius. Although the beam divergence is not linear with source-to-target distance  $d$ , the angle subtended by the beam spot viewed from the source can be given by

$$\delta = \arcsin \left[ \frac{1}{2d} (qE - qvB) \left( \frac{d}{v} \right)^2 \right] \quad (\text{A.2})$$

Thus, for a fully non-neutralized beam of 100-eV, singly-charged xenon ions with current density  $15 \text{ nA/mm}^2$  and initial radius 2 mm, the spot on a target located 1 cm away from the source will subtend an angle of  $\approx 2^\circ$  from the source.

# Bibliography

- [1] J.S. Snyder. Air and Space 2000, the Year in Review: Electric Propulsion. *Aerospace America*, 12:48–49, 2000.
- [2] W.J. Larson and J.R. Wertz. *Space Mission Analysis and Design*. Microcosm, Inc., Torrance, California, 1993.
- [3] R.W. Humble, G.N. Henry, and W.J. Larson. *Space Propulsion Analysis and Design*. McGraw-Hill, Inc., 1995.
- [4] J.M. Sponable and J.P. Penn. Electric Propulsion for Orbit Transfer—A NAVSTAR Case Study. In 19<sup>th</sup> *International Electric Propulsion Conference*, Colorado Springs, CO, 1987. AIAA 87-0985.
- [5] J.R. Beattie and J.N. Matossian. Xenon Ion Sources for Space Applications. *Review of Scientific Instruments*, 61(1):348–353, 1990.
- [6] J.S. Meserole. Launch Costs to GEO Using Solar-Powered Orbit Transfer Vehicles. In 29<sup>th</sup> *Joint Propulsion Conference*, Monterey, CA, 1993. AIAA 93-2219.
- [7] S.R. Oleson, R. Myers, C. Kluever, J.P. Riehl, and F.M. Curran. Advanced Propulsion for Geostationary Orbit Insertion and North-South Station Keeping. In 31<sup>st</sup> *Joint Propulsion Conference*, San Diego, CA, 1995. AIAA 95-2513.
- [8] H. Bassner and K.H. Groh. A 50-mN RIT Thruster Assembly for Application to Heavy GEO-Satellites. In 31<sup>st</sup> *Joint Propulsion Conference*, San Diego, CA, 1995. AIAA 95-3068.
- [9] J.E. Pollard. Simplified Approach for Assessment of Low-Thrust Elliptical Orbit Transfers. In 25<sup>th</sup> *International Electric Propulsion Conference*, Cleveland, OH, 1997. IEPC 97-160.
- [10] J.E. Pollard. Low-Thrust Maneuvers for LEO and MEO Missions. In 35<sup>th</sup> *Joint Propulsion Conference*, Los Angeles, CA, 1999. AIAA 99-2870.
- [11] M.J.L. Turner. *Rocket and Spacecraft Propulsion: Principles, Practice and New Developments*. Praxis Publishing Ltd, Chichester, UK, 2000.

- [12] J.E. Polk, R.Y. Kakuda, J.R. Anderson, J.R. Brophy, V.K. Rawlin, M.J. Patterson, J. Sovey, and J. Hamley. Validation of the NSTAR Ion Propulsion System on the Deep Space One Mission: Overview and Initial Results. In *35<sup>th</sup> Joint Propulsion Conference*, Los Angeles, CA, 1999. AIAA 99-2274.
- [13] H.F. Michielsen. A Rendezvous with Halley's Comet in 1985–1986. *J. Spacecraft*, 5(3):328–334, 1967.
- [14] K.L. Atkins, C.G. Sauer, and G.A. Flandro. Solar Electric Propulsion Combined with Earth Gravity Assist— A New Potential for Planetary Exploration. In *AIAA/AAS Astrodynamics Conference*, San Diego, CA, 1976. AIAA 76-807.
- [15] R.A. Broucke. The Celestial Mechanics of Gravity Assist. In *AIAA/AAS Astrodynamics Conference*, Minneapolis, MN, 1988. AIAA 88-4220.
- [16] J.M. Longuski and S.N. Williams. Automated Design of Multiple Encounter Gravity-Assist Trajectories. In *AIAA/AAS Astrodynamics Conference*, Portland, OR, 1990. AIAA 90-2982.
- [17] J.M. Longuski and S.N. Williams. Automated Design of Gravity-Assist Trajectories to Mars and the Outer Planets. *Celestial Mechanics and Dynamical Astronomy*, 52(3):207–220, 1991.
- [18] M.A. Minovitch. Fast Missions to Pluto Using Jupiter Gravity-Assist and Small Launch Vehicles. *J. of Spacecraft and Rockets*, 31(6):1029–1037, 1994.
- [19] W.J. Schatz, R.D. Cannova, R.T. Cowley, and D.D. Evans. Development and Flight Experience of the Voyager Propulsion System. In *15<sup>th</sup> Joint Propulsion Conference*, Las Vegas, NV, 1979. AIAA 79-1334.
- [20] A. Alagheband, T. Corazzini, O. Duchemin, D. Henny, R. Mason, and M. Noca. Neptune Explorer: An All Solar Powered Neptune Orbiter Mission. In *32<sup>nd</sup> Joint Propulsion Conference*, Lake Buena Vista, FL, 1996. AIAA 96-2980.
- [21] R.A. Park et al. Trajectory Analysis Aspects of Low-Thrust and Ballistic Rendezvous Missions to Halley's Comet. In *AIAA/AAS Astrodynamics Conference*, Princeton, NJ, 1969. AIAA 69-933.
- [22] D.H. Kruse and M.K. Fox. Trajectory Analysis Aspects of Low-Thrust and Ballistic Rendezvous Missions to Halley's Comet. In *AIAA/AAS Astrodynamics Conference*, Princeton, NJ, 1969. AIAA 69-933.
- [23] C. Sauer. Application of Solar Electric Propulsion to Future Planetary Missions. In *19<sup>th</sup> International Electric Propulsion Conference*, Colorado Springs, CO, 1987. AIAA 87-1053.

- [24] R. Kakuda, J. Sercel, and W. Lee. Small Body Rendezvous Mission using Solar Electric Ion Propulsion: Low Cost Mission Approach and Technology Requirements. *Acta Astronautica*, 35:657–666, 1995.
- [25] C.A. Kluever. Optimal Low-Thrust Interplanetary Trajectories by Direct Method Techniques. In *AAS/AIAA Space Flight Mechanics Meeting*, Austin, TX, 1996. AAS 96-194.
- [26] M. Nakano and Y. Arakawa. Interplanetary Trajectory Optimization Code for Electric Propulsion System Study. In *32<sup>nd</sup> Joint Propulsion Conference*, Lake Buena Vista, FL, 1996. AIAA 96-2981.
- [27] M. Noca and J.R. Brophy. Over Powering Solar System Exploration. In *33<sup>rd</sup> Joint Propulsion Conference*, Seattle, WA, 1997. AIAA 97-2914.
- [28] J.R. Brophy. Advanced Ion Propulsion Technology for Solar System Exploration. In *33<sup>rd</sup> Joint Propulsion Conference*, Seattle, WA, 1997. AIAA 97-2782.
- [29] J.R. Brophy, C.E. Garner, J.E. Polk, and J.M. Weiss. The Ion Propulsion System on NASA’s Space Technology 4/Champollion Comet Rendezvous Mission. In *35<sup>th</sup> Joint Propulsion Conference*, Los Angeles, CA, 1999. AIAA 99-2856.
- [30] J.R. Brophy. Ion Propulsion System Design for the Comet Nucleus Sample Return Mission. In *35<sup>th</sup> Joint Propulsion Conference*, Huntsville, AL, 2000. AIAA 2000-3414.
- [31] J.R. Brophy. Ion Propulsion for Mars Sample Return Missions. In *35<sup>th</sup> Joint Propulsion Conference*, Huntsville, AL, 2000. AIAA 2000-3412.
- [32] J.E. Polk, N.R. Moore, and J.R. Brophy. The Role of Analysis and Testing in the Service Life Assessment of Ion Engines. In *24<sup>th</sup> International Electric Propulsion Conference*, Moscow, Russia, 1995. AIAA 95-228.
- [33] O.B. Duchemin, J.R. Brophy, C.E. Garner, P.K. Ray, V. Shutthanandan, and M.A. Manteniaks. A Review of Low Energy Sputtering Theory and Experiments. In *25<sup>th</sup> International Electric Propulsion Conference*, Cleveland, OH, 1997. IEPC 97-068.
- [34] O.B. Duchemin and J.E. Polk. Low Energy Sputtering Experiments For Ion Engine Lifetime Assessment: Preliminary Results. In *35<sup>th</sup> Joint Propulsion Conference*, Los Angeles, CA, 1999. AIAA 99-2858.
- [35] J.E. Polk, O.B. Duchemin, C.-S. Ho, and B.E. Koel. The Effect of Carbon Deposition on Accelerator Grid Wear Rates in Ion Engine Ground Testing. In *36<sup>th</sup> Joint Propulsion Conference*, Huntsville, AL, 2000. AIAA 2000-3662.

- [36] H.R. Kaufman and P.D. Reader. Experimental Performance of Ion Rockets Employing Electron-Bombardment Ion Sources. In *Electrostatic Propulsion Conference*, Monterey, CA, 1960. ARS 1374-60.
- [37] J.R. Brophy, J.E. Polk, and V.K. Rawlin. Ion Engine Service Life Validation by Analysis and Testing. In *32<sup>nd</sup> Joint Propulsion Conference*, Lake Buena Vista, FL, 1996. AIAA 96-2715.
- [38] X. Peng, W.M. Ruyten, and D. Keefer. Monte Carlo Simulations of Ion-Neutral Charge Exchange Collisions and Grid Erosion in an Ion Thruster. In *29<sup>th</sup> Aerospace Sciences Meeting*, Reno, NV, 1991. AIAA 91-0607.
- [39] X. Peng, W.M. Ruyten, and D. Keefer. Three-Dimensional Particle Simulation of Grid Erosion in Ion Thrusters. In *22<sup>nd</sup> International Electric Propulsion Conference*, Viareggio, Italy, 1991. IEPC 91-119.
- [40] X. Peng, W.M. Ruyten, and D. Keefer. Further Study of the Effect of the Downstream Plasma Condition on the Accelerator Grid Erosion in an Ion Thruster. In *28<sup>th</sup> Joint Propulsion Conference*, Nashville, TN, 1992. AIAA 92-3829.
- [41] J.R. Brophy, J.E. Polk, and L.C. Pless. Test-to-Failure of a Two-Grid, 30-cm-dia. Ion Accelerator System. In *23<sup>rd</sup> International Electric Propulsion Conference*, Seattle, WA, 1993. IEPC 93-172.
- [42] X. Peng, W.M. Ruyten, and D. Keefer. Charge-Exchange Grid Erosion Study for Ground-Based and Space-Based Operations of Ion Thrusters. In *23<sup>rd</sup> International Electric Propulsion Conference*, Seattle, WA, 1993. IEPC 93-173.
- [43] V.K. Rawlin. Erosion Characteristics of Two-Grid Ion Accelerating Systems. In *23<sup>rd</sup> International Electric Propulsion Conference*, Seattle, WA, 1993. IEPC 93-175.
- [44] R.A. Bond and P.M. Latham. Ion Thruster Extraction Grid Design and Erosion Modelling using Computer Simulation. In *31<sup>st</sup> Joint Propulsion Conference*, San Diego, CA, 1995. AIAA 95-2923.
- [45] I.V. Gavryushin and V.G. Grigoryan. The Flow Modelling of Charge Exchange Ions in the Ion Thruster. In *25<sup>th</sup> International Electric Propulsion Conference*, Cleveland, OH, 1997. IEPC 97-140.
- [46] M. Tartz, E. Hartmann, R. Deltschew, and H. Neumann. Experimental Validation of a Grid Erosion Simulation. In *35<sup>th</sup> Joint Propulsion Conference*, Los Angeles, CA, 1999. AIAA 99-2860.
- [47] V.K. Rawlin. Internal Erosion Rates of a 10-kW Xenon Ion Thruster. In *24<sup>th</sup> Joint Propulsion Conference*, Boston, MA, 1988. AIAA 88-2912.

- [48] J.R. Anderson, K.D Goodfellow, J.E. Polk, R.F. Shotwell, V.K. Rawlin, J.S. Sovey, and M.J. Patterson. Results of an On-going Long Duration Ground Test of the DS1 Flight Spare Ion Engine. In *35<sup>th</sup> Joint Propulsion Conference*, Los Angeles, CA, 1999. AIAA 99-2857.
- [49] J.R. Anderson, K.D Goodfellow, J.E. Polk, V.K. Rawlin, and J.S. Sovey. Performance Characteristics of the NSTAR Ion Thruster During an On-Going Long Duration Ground Test. In *20<sup>th</sup> IEEE Aerospace Conference*, Big Sky, MT, 2000.
- [50] J.E. Polk, J.R. Brophy, and J. Wang. Spatial and Temporal Distribution of Ion Engine Accelerator Grid Erosion. In *31<sup>st</sup> Joint Propulsion Conference*, San Diego, CA, 1995. AIAA 95-2924.
- [51] K.D. Goodfellow, G.B. Ganapathi, and J.F. Stocky. An Experimental and Theoretical Analysis of the Grid Clearing Capability of the NSTAR Ion Propulsion System. In *35<sup>th</sup> Joint Propulsion Conference*, Los Angeles, CA, 1999. AIAA 99-2859.
- [52] M.J. Patterson, V.K. Rawlin, J.S. Sovey, M.J. Kussmaul, and J. Parkes. 2.3 kW Ion Thruster Wear Test. In *31<sup>st</sup> Joint Propulsion Conference*, San Diego, CA, 1995. AIAA 95-2516.
- [53] V. Rawlin. NSTAR Memorandum. Technical report, NASA Glenn Research Center, 1996.
- [54] J.E. Polk *et al.* A 1000-Hour Wear Test of the NASA 30-cm Xenon Ion Engine. In *32<sup>nd</sup> Joint Propulsion Conference*, Lake Buena Vista, FL, 1996. AIAA 962717.
- [55] J.E. Polk, J.R. Anderson, J.R. Brophy, V.K. Rawlin, M.J. Patterson, J. Sovey, and J. Hamley. An Overview of the Results from an 8200 Hour Wear Test of the NSTAR Ion Thruster. In *35<sup>th</sup> Joint Propulsion Conference*, Los Angeles, CA, 1999. AIAA 99-2446.
- [56] J.R. Brophy. Ion thruster performance model. Technical report, Colorado State University, Fort Collins, CO, 1984. NASA CR-174810.
- [57] J.E. Polk, J.R. Anderson, J.R. Brophy, V.K. Rawlin, J. Patterson, and J.S. Sovey. The Effect of Engine Wear on Performance in the NSTAR 8000 Hour Ion Engine Endurance Test. In *33<sup>rd</sup> Joint Propulsion Conference*, Seattle, WA, 1997. AIAA 97-3387.
- [58] T.R. Sarver-Verhey. 28,000 Hour Xenon Hollow Cathode Life Test Results. In *25<sup>th</sup> International Electric Propulsion Conference*, Cleveland, OH, 1997. IEPC 97-168.

- [59] T.R. Sarver-Verhey. Destructive Evaluation of a Xenon Hollow Cathode After a 28,000 Hour Life Test. In *34<sup>th</sup> Joint Propulsion Conference*, Cleveland, OH, 1998. AIAA 98-3482.
- [60] I. Kameyama and P.J. Wilbur. Zenith-Angle Distributions of Erosion Rates near High-Current Hollow Cathodes. In *32<sup>nd</sup> Joint Propulsion Conference*, Lake Buena Vista, FL, 1996. AIAA 96-3208.
- [61] P.M. Latham, A.J. Pearce, and R.A. Bond. Erosion Processes in the UK-25 Ion Thruster. In *22<sup>nd</sup> International Electric Propulsion Conference*, Viareggio, Italy, 1991. IEPC 91-096.
- [62] V.J. Friedly and P.J. Wilbur. High Current Hollow Cathode Phenomena. *Journal of Propulsion and Power*, 8(3):635–643, May–June 1992.
- [63] I. Kameyama and P.J. Wilbur. Measurements of Ions from High-Current Hollow Cathodes Using Electrostatic Energy Analyzer. *Journal of Propulsion and Power*, 16(3):529–535, May–June 2000.
- [64] M.W. Crofton. The Feasibility of Hollow Cathode Ion Thrusters: A Preliminary Characterization. In *36<sup>th</sup> Joint Propulsion Conference*, Huntsville, AL, 2000. AIAA 2000-3273.
- [65] J.E. Polk, J.R. Anderson, J.R. Brophy, J. Wang, O. Duchemin, C.-S. Ho, and B.E. Koel. Plasma-Surface Interactions and Life-Limiting Phenomena in Ion Engines. In *42<sup>nd</sup> Meeting of the American Physical Society Division of Plasma Physics*, Quebec City, Canada, 2000.
- [66] N. Moore, D. Ebbeler, and M. Creager. Failure Risk Assessment by Analysis and Testing. In *28<sup>th</sup> Joint Propulsion Conference*, Nashville, TN, 1992. AIAA 92-3415.
- [67] W. Nelson. Weibull Analysis of Reliability Data with Few or No Failures. *Journal of Quality Technology*, 17(3):140–146, 1985.
- [68] A. Bendell, J. Disney, and W.A. Pridmore, editors. *Taguchi Methods: Applications in World Industry*. Springer-Verlag, 1989.
- [69] J.E. Polk, N.R. Moore, L.E. Newlin, J.R. Brophy, and D.H. Ebbeler. Probabilistic Analysis of Ion Engine Accelerator Grid Life. In *23<sup>rd</sup> International Electric Propulsion Conference*, Seattle, WA, 1993. IEPC 93-176.
- [70] J.R. Anderson, J.E. Polk, and J.R. Brophy. Service Life Assessment for Ion Engines. In *25<sup>th</sup> International Electric Propulsion Conference*, Cleveland, OH, 1997. IEPC 97-049.

- [71] J. Wang, J.R. Anderson, and J.E. Polk. Three-Dimensional Particle Simulations of Ion Optics Plasma Flow. In *34<sup>th</sup> Joint Propulsion Conference*, Cleveland, OH, 1998. AIAA 98-3799.
- [72] L.I. Maissel and R. Glang, editors. *Handbook of Thin Film Technology*, chapter 3. McGraw-Hill, New York, 1970.
- [73] W. Eckstein. *Computer Simulation of Ion-Solid Interactions*. Springer-Verlag, New York, 1991.
- [74] N.H. Tolk, Z. Hargitai, Y. Yao, B. Pratt-Ferguson, M.M. Albert, R.G. Albridge, A.V. Barnes, J.M. Gilligan, V.D. Gordon, G. Lupke, A. Puckett, J. Tully, G. Betz, and W. Husinsky. Molecular Effects in Measured Sputtering Yields on Gold at Near Threshold Energies. *Izvestiya Akademii Nauk Seriya Fizicheskaya*, 62(4):676–679, 1998.
- [75] H.E. Wilhelm. Quantum-Statistical Analysis of Low-Energy Sputtering. *Australian Journal of Physics*, 38(2):125–133, 1985.
- [76] J.P. Biersack. Computer Simulations of Sputtering. *Nuclear Instruments and Methods in Physics Research Section B - Beam Interactions with Materials and Atoms*, 27:21–36, 1987.
- [77] C.D. O’Brian, A. Lindner, and W.J. Moore. Sputtering of Silver by Hydrogen Ions. *Journal of Chemical Physics*, 29(3), 1958.
- [78] C.E. KenKnight and G.K. Wehner. Sputtering of Metals by Hydrogen Ions. *Journal of Applied Physics*, 35:322, 1964.
- [79] J.L. Crasten, R. Hancox, A.E. Robson, S. Kaufmann, H.T. Miles, A. Ware, and J.A. Wessen. The Roles of Materials in Controlled Thermonuclear Research. *Proceedings of 2<sup>nd</sup> Int. Conf. on the Peaceful Uses of Atomic Energy*, 32:414, 1958.
- [80] R. Bastasz. An Application of SIMS to Fusion Energy Research: Determination of Ion Impact Desorption Cross Sections. *IEEE Transactions on Nuclear Science*, NS-30(2):1183–1186, 1983.
- [81] J.F. Ziegler, J.P. Biersack, and U. Littmark. *The Stopping and Range of Ions in Solids*. Pergamond Press, New York, 1985.
- [82] R. Behrisch, editor. *Sputtering by Particle Bombardment I: Physical Sputtering of Single-Element Solids*. Springer-Verlag, New York, 1981.
- [83] R. Behrisch, G. Maderlechner, and B.M.U. Scherzer. The Sputtering Mechanism for Low-Energy Light Ions. *Journal of Applied Physics*, 18:391, 1964.

- [84] G.K. Wehner and D. Rosenberg. Angular Distribution of Sputtered Material. *Journal of Applied Physics*, 31:177, 1960.
- [85] R.R. Olson, M.E. King, and G.K. Wehner. Mass Effects on Angular Distribution of Sputtered Atoms. *Journal of Applied Physics*, 50(5):3677, 1979.
- [86] W. Eckstein, C. García-Rosales, J. Roth, and J. László. Threshold Energy for Sputtering and its Dependence on Angle of Incidence. *Nuclear Instruments and Methods in Physics Research B*, 83(1-2):95–109, 1993.
- [87] P.K. Ray and V. Shuttanandan. Low Energy Sputtering Research. Technical report, NASA, 1999. CR 1999-209161.
- [88] J. Lindhard, V. Nielsen, and M. Scharff. Approximation Method in Classical Scattering by Screened Coulomb Fields (Notes on Atomic Collisions, I). *Det Kgl. Danske Videnskabernes Selskab-Mat. Fys. Meddr.*, 36(10), 1968.
- [89] A. Sommerfeld. Asymptotic Integration of the Differential Equation Relating to the Thomas-Fermi Atom. *Zeitung F. Physik*, 78:283, 1932.
- [90] G. Molière. Theory of Scattering of Fast Charged Particles. I. Single Scattering in a Screened Coulomb Field. *Z. Naturforschung*, A2:133, 1947.
- [91] W. Lenz. Über die Anwendbarkeit der Statistischen Methode auf Ionengitter. *Zeitung F. Physik*, 77:713, 1932.
- [92] H. Jensen. Die Ladungsverteilung in Ionen und die Gitterkonstante des Rubidiumbromids nach der Statistischen Methode. *Zeitung F. Physik*, 77:722, 1932.
- [93] N. Bohr. The Penetration of Atomic Particles Through Matter. *Det Kgl. Danske Videnskabernes Selskab-Mat. Fys. Meddr.*, 18(8), 1948.
- [94] D.E. Harrison Jr. and G.D. Magnuson. Sputtering Thresholds. *Physical Review*, 122(5):1421–1430, 1961.
- [95] P. Sigmund. Theory of Sputtering. I. Sputtering Yields of Amorphous and Polycrystalline Targets. *Physical Review*, 184(2):383–415, 1969.
- [96] J. Bohdansky, J. Roth, and H.L. Bay. An Analytical Formula and Important Parameters for Low-Energy Ion Sputtering. *Journal of Applied Physics*, 51(5):2861–2865, 1980.
- [97] Y. Yamamura, N. Matsunami, and N. Itoh. A New Empirical Formula for the Sputtering Yield. *Radiation Effects Letters*, 68:83–87, 1982.

- [98] Y. Yamamura, Y. Itikawa, and N. Itoh. Angular dependence of sputtering yields of monoatomic solids. Technical report, Institute of Plasma Physics, Nagoya University, Nagoya, Japan, 1983. IPPJ-AM-26.
- [99] R. Behrish and W. Eckstein. Sputtering Yield Increase with Target Temperature for Ag. *Nuclear Instruments and Methods in Physics Research Section B - Beam Interactions with Materials and Atoms*, 82(2):255–258, 1993.
- [100] Y. Yamamura and H. Tawara. Energy Dependence of Ion-Induced Sputtering Yields from Monatomic Solids at Normal Incidence. *Atomic Data and Nuclear Tables*, 62(2):149–253, 1996. Erratum in *Atomic Data and Nuclear Tables*, 63(2):353, 1996.
- [101] R.C. Bradley. Sputtering of Alkali Atoms by Inert Gas Ions of Low Energy. *Physical Review*, 93(4):1421–1430, 1954.
- [102] G.K. Wehner. Low-Energy Sputtering Yields in Hg. *Physical Review*, 112(4):1120–1124, 1958.
- [103] N.D. Morgulis and V.D. Tishchenko. The Investigation of Cathode Sputtering in the Near Threshold Region. I. *Soviet Physics JETP*, 3(1):52–56, 1956.
- [104] R.V. Stuart and G.K. Wehner. Sputtering Yields at Very Low Bombarding Ion Energies. *Journal of Applied Physics*, 33(7):2345–2352, 1962.
- [105] R. Weissmann and P. Sigmund. Sputtering and Backscattering of keV Light Ions Bombarding Random Targets. *Radiation Effects*, 19:7–14, 1973.
- [106] S.G. Askerov and L.A. Sena. Cathode Sputtering of Metals by Slow Mercury Ions. *Soviet Physics - Solid State*, 11(6):1288–1293, 1969.
- [107] E. Hotston. Threshold Energies for Sputtering. *Nuclear Fusion*, 15:544–547, 1975.
- [108] H.L. Bay, J. Roth, and J. Bohdansky. Light-Ion Sputtering Yields for Molybdenum and Gold at Low Energies. *Journal of Applied Physics*, 48(11):4722–4728, 1977.
- [109] Y. Yamamura. An Empirical-Formula for Angular-Dependence of Sputtering Yields. *Radiation Effects and Defects in Solids*, 80(1-2):57–72, 1984.
- [110] M.A. Manteniaks. Sputtering Threshold Energies of Heavy Ions. In *25<sup>th</sup> International Electric Propulsion Conference*, Cleveland, OH, 1997. IEPC 97-187.
- [111] D. Rosenberg and G.K. Wehner. Sputtering Yields for Low-Energy He<sup>+</sup>-, Kr<sup>+</sup>-, and Xe<sup>+</sup>-Ion Bombardment. *Journal of Applied Physics*, 33(5):1842–1845, 1962.

- [112] Y. Yamamura and J. Bohdansky. Few Collisions Approach for Threshold Sputtering. *Vacuum*, 35(12):561–571, 1985.
- [113] J. Lindhard and M. Scharff. Energy Dissipation by Ions in the keV Region. *Physical Review*, 124:128, 1961.
- [114] J. Bohdansky. A Universal Relation for the Sputtering Yield of Monoatomic Solids at Normal Ion Incidence. *Nuclear Instruments and Methods in Physics Research*, B2:587–591, 1984.
- [115] P. Sigmund. Mechanisms and Theory of Physical Sputtering by Particle Impact. *Nuclear Instruments and Methods in Physics Research*, B27:1–20, 1987.
- [116] M.W. Thompson. II. The Energy Spectrum of Ejected Atoms During the High-Energy Sputtering of Gold. *Philos. Mag.*, 18:377–414, 1968.
- [117] R.P. Webb and I.H. Wilson. Problems Using the Sigmund Formula for the Calculation of Sputtering Yields. *Vacuum*, 39(11-12):1163–1165, 1989.
- [118] S.A. Schwarz and C.R. Helms. A Statistical Model of Sputtering. *Journal of Applied Physics*, 50(5):3677, 5492–5499 1979.
- [119] E. Hintz, D. Rusbuldt, B. Schweer, J. Bohdansky, J. Roth, and A.P. Martinelli. The Determination of the Flux Density of Sputtered Atoms by Means of Pulsed Dye Laser Excited Fluorescence. *Journal of Nuclear Materials*, 93-94:44, 1980.
- [120] W. Eckstein, C. García-Rosales, J. Roth, and W. Ottenberger. Technical report, Max-Planck Institut für Plasmaphysik, Garching, Germany, 1993. IPP 9/82.
- [121] L. Matsunami, Y. Yamamura, Y. Itikawa, N. Itoh, Y. Kazumata, S. Miyagawa, K. Morita, and R. Shimizu. A Semiempirical Formula for the Energy Dependence of the Sputtering Yield. *Radiation Effects Letters*, 57:15–21, 1980.
- [122] Y. Yamamura, N. Matsunami, and N. Itoh. Theoretical Studies on an Empirical Formula for Sputtering Yield at Normal Incidence. *Radiation Effects Letters*, 71:65–86, 1983.
- [123] N. Matsunami, Y. Yamamura, Y. Itikawa, N. Itoh, Y. Kazumata, S. Miyagawa, K. Morita, R. Shimizu, and H. Tawara. Energy-Dependence of the Ion-Induced Sputtering Yields of Monoatomic Solids. *Atomic Data and Nuclear Table*, 31(1):1–80, 1984.
- [124] H.J. Strydom and W.H. Gries. A Comparison of 3 Versions of Sigmund Model of Sputtering Using Experimental Results. *Radiation Effects Letters*, 86(4):145–151, 1984.

- [125] W.H. Gries and H.J. Strydom. A Practical Table of Sputtering Yields for the Non- Expert User. *Fresenius Zeitschrift für Analytische Chemie*, 319(6-7):727–728, 1984.
- [126] C. Steinbrüchel. A Simple Formula for Low-Energy Sputtering Yields. *Applied Physics A - Materials Science and Processing*, 36(1):37–42, 1985.
- [127] V.I. Shulga. The Density Effects in Sputtering of Amorphous Materials. *Nuclear Instruments and Methods in Physics Research Section B - Beam Interactions with Materials and Atoms*, 170(3-4):347–361, 2000.
- [128] Y. Kitazoe and Y. Yamamura. Hydrodynamical Approach to Non-Linear Effects in Sputtering Yields. *Radiation Effects Letters*, 50:39–44, 1980.
- [129] Y. Kitazoe, N. Hiraoka, and Y. Yamamura. Hydrodynamical Analysis of Non-Linear Sputtering Yields. *Surface Science*, 111(3):381–394, 1981.
- [130] M.M. Jakas. A Note on Thermal Spikes and Sputtering Yields. *Radiation Effects and Defects in Solids*, 152(2):157–163, 2000.
- [131] N. Laegreid and G.K. Wehner. Sputtering Yields of Metals for Ar<sup>+</sup> and Ne<sup>+</sup> Ions with Energies from 50 to 600 eV. *Journal of Applied Physics*, 32(3):365, 1961.
- [132] R. Behrisch. Festkörperzerstäubung durch Ionenbeschuß. *Ergeb. Exacten. Naturwiss.*, 35:295–443, 1964.
- [133] G. Leibfried. *Bestrahlungseffekte in Festkörpern*. G.B. Teubner, Stuttgart, 1965.
- [134] H.H. Andersen and P. Sigmund. *Nuclear Instruments and Methods*, 38:238–240, 1965.
- [135] O.B. Firsov. *Soviet Physics JETP*, 6:534, 1958.
- [136] C.H. Weijzenfeld, A. Hoogendoorn, and M. Koedam. Sputtering of Polycrystalline Metals by Inert Gas Ions of Low-Energy (100–1000 eV). *Physica*, 27:763, 1961.
- [137] S. Bhattacharjee, J. Zhang, V. Shutthanandan, P.K. Ray, N.R. Shivaparan, and R.J. Smith. Application of Secondary Neutral Mass Spectrometry in Low-Energy Sputtering Yield Measurements. *Nuclear Instruments and Methods in Physics Research Section B - Beam Interactions with Materials and Atoms*, 129(1):123–129, 1997.
- [138] J.J. Blandino, D.G. Goodwin, and C.E. Garner. Low Energy Sputter Yields for Diamond, Carbon- Carbon Composite, and Molybdenum Subject to Xenon Ion Bombardment. *Diamond and Related Materials*, 9(12):1992–2001, 2000.

- [139] <http://www.research.ibm.com/ionbeams/>.
- [140] R. Hultgren, P.D. Desai, D.T. Hawkins, M. Gleiser, K.K. Kelley, and D.D. Wagman. *Selected Values of the Thermodynamic Properties of the Elements*. American Society for Metals, 1973.
- [141] J. Fine. Absolute sputtering yield measurement methods: A review. In *10<sup>th</sup> Summer School and Symposium on the Physics of Ionized Gases*, Beograd, Yugoslavia, 1980.
- [142] G.K. Wehner. Sputtering Yields for Normally Incident Hg<sup>+</sup>-Ion Bombardment at Low Ion Energy. *Physical Review*, 108(1):35–45, 1957.
- [143] R. Behrisch, J. Bohdanský, G.H. Oetjen, J. Roth, G. Schilling, and H. Verbeek. Measurements of the Erosion of Stainless Steel, Carbon, and SiC by Hydrogen Bombardment in the Energy Range of 0.5–7.5 keV. *Journal of Nuclear Materials*, 60:321–329, 1976.
- [144] E. Hechtel, H.L. Bay, and J. Bohdanský. Low Energy Self-sputtering Yields of Nickel. *Applied Physics*, 16:147–150, 1978.
- [145] Y. Garnier, V. Viel, J.F. Roussel, and J. Bernard. Low-Energy Xenon Ion Sputtering of Ceramics Investigated for Stationary Plasma Thrusters. *Journal of Vacuum Science and Technology A - Vacuum Surfaces and Films*, 17(6):3246–3254, 1999.
- [146] Y. Okajima. Estimation of Sputtering Rate by Bombardment with Argon Gas Ions. *Journal of Applied Physics*, 51(1):715–717, 1980.
- [147] A.K. Handoo and P.K. Ray. Modeling of life limiting phenomena in the discharge chamber of an electron bombardment ion thruster. Technical report, Tuskegee University, Tuskegee, AL, 1991. Grant NAG 8-020.
- [148] A.K. Handoo and P.K. Ray. Sputtering Yield of Chromium by Argon and Xenon Ions with Energies from 50 TO 500-eV. *Applied Physics A - Solids and Surfaces*, 54:92–94, 1992.
- [149] A.K. Handoo and P.K. Ray. Sputtering of Cobalt and Chromium by Argon and Xenon Ions near the Threshold Energy Region. *Canadian Journal of Physics*, 71:155–158, 1993.
- [150] J. Polk. *Mechanisms of Cathode Erosion in Plasma Thrusters*. PhD thesis, Princeton University, N.J., 1996.
- [151] R.V. Stuart and G.K. Wehner. Sputtering Thresholds and Displacement Energies. *Physical Review Letters*, 4(8):409–410, 1960.

- [152] B.A. Rock, M.A. Manteniaks, and M.L. Parsons. Rapid Evaluation of Ion Thruster Lifetime Using Optical Emission Spectroscopy. In *18<sup>th</sup> International Electric Propulsion Conference*, Alexandria, VA, 1985. AIAA 85-2011.
- [153] J.N. Smith Jr., C.H. Meyer Jr., and J.K. Layton. Auger Electron Spectroscopy in Sputtering Measurements: Application to Low-Energy Ar<sup>+</sup> sputtering of Ag and Nb. *Journal of Applied Physics*, 46(10):4291–4293, 1975.
- [154] V. Shutthanandan, P.K. Ray, N.R. Shivaparan, R.J. Smith, S. Thevuthasan, and M.A. Manteniaks. On the Measurement of Low-Energy Sputtering Yield Using Rutherford Backscattering Spectrometry. In *25<sup>th</sup> International Electric Propulsion Conference*, Cleveland, OH, 1997. IEPC 97-069.
- [155] D. McKeown. New Method for Measuring Sputtering Near Threshold. *The Review of Scientific Instruments*, 32(2):133–136, 1960.
- [156] W.H. Hayward and A.R. Wolter. Sputtering Yield Measurements with Low-Energy Metal Ion Beams. *Journal of Applied Physics*, 40(7):2911–2916, 1969.
- [157] H.H. Andersen and H. Bay. The Z<sub>1</sub> Dependence of Heavy-Ion Sputtering Yield in Copper. *Radiation Effects*, 13:67–74, 1972.
- [158] B. Navinšek, P. Panjan, and A. Žabkar. A Comparison of Sputtered Ni/Cr Interface Depth Resolution as Obtained by the Quartz Crystal Microbalance Mass-Loss Method and Auger Spectroscopy. *Journal of Vacuum Science Technology A*, 3(3):671–673, 1985.
- [159] Y. Yao, Z. Hargitai, M. Albert, R.G. Albridge, A.V. Barnes, J.M. Gilligan, B. Pratt Ferguson, G. Lüpke, V.D. Gordon, J.C. Tolk, N.H. Tully, G. Betz, and W. Husinsky. New Molecular Collisional Interaction Effect in Low-Energy Sputtering. *Physical Review Letter*, 81(3):550–553, 1998.
- [160] G. Hayderer, M. Schmid, P. Varga, H.P. Winter, and F. Aumayr. A Highly Sensitive Quartz-Crystal Microbalance for Sputtering Investigations in Slow Ion-Surface Collisions. *Review of Scientific Instruments*, 70(9):3696–3700, 1999.
- [161] C.A. Gogol. Advances in the quartz crystal deposition controller: A history of the technology and recent technical improvements. Technical report, Leybold Inficon, 1990.
- [162] C. Lu and A.W. Czanderna, editors. *Applications of Piezoelectric Quartz Crystal Microbalances*. Elsevier, New York, 1984.
- [163] G. Sauerbrey. Use of Oscillator Quartz Crystals for Weighing Thin Layers and Microweighing. *Zeitschrift für Physik*, 155:206–222, 1959.

- [164] Institute for Electrical and Electronics Engineers, New York. *IEEE Standard on Piezoelectricity*, 1978. Vol. 176.
- [165] P.J. Cumpson and M.P. Seah. The Quartz Crystal Microbalance; Radial/Polar Dependence of Mass Sensitivity Both on and off the Electrodes. *Measurement Science and Technology*, 1:544–555, 1990.
- [166] *XTM/2 Deposition Monitor Manual*. Leybold Inficon Inc., East Syracuse, N.Y., 1996. P/N 074-186.
- [167] E. Hafner. I. Crystal Resonators. *IEEE Transactions on Sonics and Ultrasonics*, su-21(4):220–237, 1974.
- [168] E. Törnqvist. *The kinetics of Adsorption and Reaction of Molecules on Evaporated Metal Films*. PhD thesis, Chalmers University, Göteborg, Sweden, 1980.
- [169] H.F. Tiersten and R.C. Smythe. An Analysis of Contoured Crystal Resonators Operating in Overtones of Coupled Thickness Shear and Thickness Twist. *Journal of the Acoustic Society of America*, 65(6):1455–1460, 1979.
- [170] J.H. Moore, C.C. Davis, and M.A. Coplan. *Building Scientific Apparatus: a Practical Guide to Design and Construction*. Perseus Books Publishing, LLC, 2<sup>nd</sup> edition, 1991.
- [171] J.A. Thornton. Influence of Apparatus Geometry and Deposition Conditions on the Structure and Topography of Thick Sputtered Coatings. *Journal of Vacuum Science Technology*, 11(4):666–670, 1960.
- [172] J.L. Vossen and W. Kern, editors. *Thin Film Processes*. Academic Press, Inc., New York, 1978.
- [173] A. Belkind. Thin Film Phenomena: an Introductory Course. In *International Conference on Metallurgical Coatings and Thin Films*, San Diego, CA, 1998.
- [174] K.L. Chopra. *Thin Film Phenomena*. McGraw-hill, New York, 1969.
- [175] J.R. Davis, editor. *Metals Handbook*. ASM International Handbook Committee, 2<sup>nd</sup> desk edition, 1998.
- [176] O.C. Yonts and D.E. Harrison Jr. Surface Cleaning by Cathode Sputtering. *Journal of Applied Physics*, 31(9):1583–1584, 1960.
- [177] S.C. Brown. *Basic Data of Plasma Physics*. MIT press, 2<sup>nd</sup> edition, 1966.
- [178] F. Rapp and W.E. Francis. Charge Exchange between Gaseous Ions and Atoms. *Journal of Chemical Physics*, 37(11):2631–2645, 1962.

- [179] B.H. Bransden and M.R.C. McDowell, editors. *Charge Exchange and the Theory of Ion-Atom Collisions*. Clarendon Press, Oxford, U.K., 1992.
- [180] H.F. Winters and P. Sigmund. Sputtering of Chemisorbed Gas (Nitrogen on Tungsten) by Low-Energy Ions. *Journal of Applied Physics*, 45(11):4760–4766, 1974.
- [181] H.F. Winters and E. Taglauer. Sputtering of Chemisorbed Nitrogen from Single-Crystal Planes of Tungsten and Molybdenum. *Phys. Rev. B*, 35(5):2174–2187, 1987.
- [182] W.L. Baun. Quantitative Surface Analysis of Materials. In *ASTM Symposium on Surface Analysis*, Cleveland, OH, 1977. ASTM Technical Publication 643.
- [183] E. Taglauer. Probing Surfaces with Low-Energy Ions. *Nuclear Instruments and Methods in Physics Research B*, 98:392–399, 1995.
- [184] D.P. Woodruff and T.A. Delchar, editors. *Modern Techniques of Surface Science*. Cambridge University Press, Cambridge, 1994.
- [185] J.L. Peña, J.W. Dieball, and D. Lichtman. Argon Ion Impact Desorption Cross Sections of Chlorine and Carbon from Molybdenum. *Journal of Nuclear Materials*, 102:267–281, 1981.
- [186] E.I. Ko and R.J. Madix. Effects of Adsorbed Carbon and Oxygen on the Chemisorption of H<sub>2</sub> and CO on Mo(100). *Surface Science*, 109:221–238, 1981.
- [187] T. Schöberl. On the non-Langmuir-McLean Segregation of Carbon to Mo(100): Bulk Depletion and Multilayer Enrichment. *Surface Science*, 326:267–274, 1995.
- [188] E. Taglauer, G. Marin, and W. Heiland. A Contribution to the Investigation of Ion Impact Desorption by Ion Scattering. *Applied Physics*, 13:47–49, 1977.
- [189] E. Taglauer and W. Heiland. Ion-Induced Desorption of Adsorption Layers on Annealed and Prebombarded Surfaces. *Journal of Nuclear Materials*, 93 and 94:823–829, 1980.
- [190] E. Taglauer, W. Heiland, and J. Onsgaard. Ion Beam Induced Desorption of Surface Layers. *Nuclear Instrument Methods*, 168:571–577, 1980.
- [191] A. Sagara and K. Kamada. Compilation and Evaluation of Ion Impact Desorption Cross-Section. *Journal of Nuclear Materials*, 111 and 112:812–815, 1982.
- [192] T. Oshiyama, S. Nagai, and K. Ozawa. Role of Reflection and Sputtering in Ion Impact Desorption of Gases From Solid Surfaces. *Journal of Nuclear Materials*, 168:162–170, 1989.

- [193] H.D. Mieskes, W. Assmann, M. Brodale, M. Dobler, H. Gluckler, P. Hartung, and P. Stenzel. Measuring Sputtering Yields of High Energy Heavy Ions on Metals. *Nuclear Instruments and Methods in Physics Research Section B - Beam Interactions with Materials and Atoms*, 146(1-4):162–171, 1998.
- [194] T.B. Fryberger and P.C. Stair. The Metal-Oxide Transition on Mo(100) Monitored by Photoemission of Physisorbed Xenon. *Chemical Physics Letters*, 93(3):151–156, 1982.
- [195] L.D. López-Carreño, G. Benítez, L. Viscido, J.M. Heras, F. Yubero, J.P. Espinós, and A.R. González-Elipe. Oxidation of Molybdenum Surfaces by Reactive Oxygen Plasma and  $O_2^+$  Bombardment: an Auger and XPS Study. *Surface and Interface Analysis*, 26:235–241, 1998.
- [196] P. Lorrain and D.R. Corson. *Electromagnetism, Principles and Applications*. W. H. Freeman and Company, New York, 2<sup>nd</sup> edition, 1997.